

Preparation and characterization of alpha'-SiAlON ceramics

Citation for published version (APA):

Cao, G. Z. (1991). *Preparation and characterization of alpha'-SiAlON ceramics*. [Phd Thesis 1 (Research TU/e / Graduation TU/e), Chemical Engineering and Chemistry]. Technische Universiteit Eindhoven.
<https://doi.org/10.6100/IR350592>

DOI:

[10.6100/IR350592](https://doi.org/10.6100/IR350592)

Document status and date:

Published: 01/01/1991

Document Version:

Publisher's PDF, also known as Version of Record (includes final page, issue and volume numbers)

Please check the document version of this publication:

- A submitted manuscript is the version of the article upon submission and before peer-review. There can be important differences between the submitted version and the official published version of record. People interested in the research are advised to contact the author for the final version of the publication, or visit the DOI to the publisher's website.
- The final author version and the galley proof are versions of the publication after peer review.
- The final published version features the final layout of the paper including the volume, issue and page numbers.

[Link to publication](#)

General rights

Copyright and moral rights for the publications made accessible in the public portal are retained by the authors and/or other copyright owners and it is a condition of accessing publications that users recognise and abide by the legal requirements associated with these rights.

- Users may download and print one copy of any publication from the public portal for the purpose of private study or research.
- You may not further distribute the material or use it for any profit-making activity or commercial gain
- You may freely distribute the URL identifying the publication in the public portal.

If the publication is distributed under the terms of Article 25fa of the Dutch Copyright Act, indicated by the "Taverne" license above, please follow below link for the End User Agreement:

www.tue.nl/taverne

Take down policy

If you believe that this document breaches copyright please contact us at:

openaccess@tue.nl

providing details and we will investigate your claim.

Handwritten signature

**PREPARATION AND CHARACTERIZATION
OF α' -SIALON CERAMICS**

GUO-ZHONG CAO

**PREPARATION AND CHARACTERIZATION
OF α' -SIALON CERAMICS**

PREPARATION AND CHARACTERIZATION OF α^2 -SIALON CERAMICS

PROEFSCHRIFT

ter verkrijging van de graad van doctor aan
de Technische Universiteit Eindhoven, op gezag
van de Rector Magnificus, prof. dr. J.H. van Lint,
voor een commissie aangewezen door het College
van Dekanen in het openbaar te verdedigen
op dinsdag 16 april 1991 te 16.00 uur.

door

GUO-ZHONG CAO

geboren te JIANGSU, CHINA



Dit proefschrift is goedgekeurd door
de promotoren:

prof. dr. R. Metselaar
en
prof. dr. G. Ziegler

CONTENTS

Chapter One, Introduction	
1-1. Overview	1
1-2. Silicon Nitride Ceramics	1
1-3. Outline of This Thesis	3
1-4. References	4
Chapter Two, Fundamentals of α' -Sialons	
2-1. Introduction	7
2-2. Structure of α and β - Si_3N_4	7
2-3. Crystal Chemistry of α' -Sialons	9
2-4. Representation of Sialon Systems	13
2-5. Phase Relationships Concerning α' -Sialons	15
2-6. Summary	21
2-7. References	21
Chapter Three, Experimental Procedures	
3-1. Raw Materials	26
3-2. Mixture Compositions	30
3-3. Powder Processing	32
3-4. Sintering Processing	33
3-5. Characterization	34
3-6. References	35
Chapter Four, Formation and Densification of α' -Sialon Ceramics	
4-1. Introduction	37
4-2. Formation of Sialons	38
4-3. Densification of α' -Sialon Ceramics	48
4-4. Microstructural Development	58
4-5. Discussion and Summary	64
4-6. References	67

Chapter Five, Gas Pressure Sintering of α' -Sialon Ceramics	
5-1. Gas Pressure Sintering	70
5-2. Gas Pressure Sintering with Two Steps	73
5-3. Statistical Evaluation	78
5-4. Other Factors Concerning GPS Sintering	88
5-5. Discussion and Summary	95
5-6. References	96
Chapter Six, Microstructure and Properties of α' -Sialon Ceramics	
6-1. Introduction	99
6-2. Microstructure	99
6-3. Mechanical Properties	114
6-4. Oxidation Resistance	121
6-5. Summary	133
6-6. References	135
Chapter Seven, Summary and Conclusions	138
Summary	143
Samenvatting	145
Acknowledgements	
Curriculum Vitae	

CHAPTER ONE. INTRODUCTION

1-1. OVERVIEW

Materials are always the indispensable basis for any activity conducted by mankind. They are widely known to have characterized mankind's historic development — from the Stone Age, to the Bronze Age, to the Iron Age. And now there is a worldwide ceramic fever due to the emergence of advanced ceramics in the last decades.

The word "ceramic", which originated a long time ago from the Greek word "keramos", nowadays has been widely broadened being defined as an inorganic, nonmetallic material processed or solidated at high temperatures.

Ceramic materials can be classified as traditional and advanced ceramics. Traditional ceramics are primarily clay-based materials such as brick, tile, sanitaryware, dinnerware, clay pipe and electrical porcelain. Based on their primary applications, advanced ceramics, also named as high-tech ceramics or fine ceramics, can be subdivided into functional and structural ceramics. An example of functional ceramics is high temperature superconductor. Examples of structural ceramics are silicon nitride, silicon carbide, toughened zirconia and fiber/whisker-reinforced ceramics.

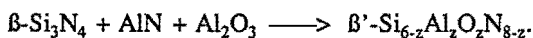
1-2. SILICON NITRIDE CERAMICS

Silicon nitride and oxynitride ceramics have attracted interest for high temperature engineering applications for nearly forty years [1-4], because of their excellent properties: (1) high strength; (2) wear resistance; (3) high decomposition temperature; (4) oxidation resistance; (5) thermal shock resistance; (6) low coefficient of friction and (7) resistance to corrosive environments.

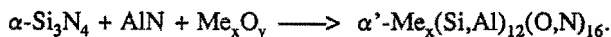
The formation of silicon nitride (Si_3N_4) was reported approximately a century ago [5-7]. However, fully dense silicon nitride ceramics were only obtained by hot-pressing in 1961 [8]. Huge efforts on the investigation of silicon nitride ceramics have been made in the last three decades, resulting in a tremendous progress [9-10].

The properties mentioned above of silicon nitride ceramics are achieved only in fully dense materials. But as a highly covalent compound, silicon nitride exhibits a very low diffusivity [11-15] and therefore cannot be densified by using conventional sintering methods. This difficulty has been partly overcome by gas pressure sintering and hot isostatic pressing either with sintering additives or by using impure silicon nitride powders. The sintering additives are usually metal oxides, such as MgO, Al₂O₃, Y₂O₃ and Ln₂O₃ [16-23], but some metals, carbides and nitrides have been tried as well [24-27]. At high temperatures these additives will react with both the oxygen-rich layer, which is always present at the surface of each silicon nitride particle [28-29], and a small fraction of silicon nitride to form an oxynitride liquid phase. This allows densification by the mechanism of liquid phase sintering. However, the liquid cools to give glassy phases at the grain boundaries, of which only a part can be crystallized by carefully controlling the cooling process and/or by using post-sintering heat-treatment [30-32]. Thus these intergranular phases degrade the chemical and mechanical properties of the densified products at high temperatures.

In the beginning of the 1970's, Oyama et al. [33-35] and Jack et al. [36-37] reported that Al³⁺ can enter the silicon nitride crystal lattice without changing the structure by replacing Si⁴⁺ if at the same time N³⁻ is replaced by O²⁻ as well. Such solid solutions have been named "Sialon" — the acronym for these materials based on the abbreviation of these four elements [37]. The solid solutions above are called β'-sialons since they are derived from the structure of β-silicon nitride.



As early as β'-sialons were reported, the formation of α-silicon nitride solid solutions with expanded α-structure by reaction of lithium silicon nitride with alumina [36] or of lithium aluminate with silicon nitride [38] was observed as well. So-called α'-sialons were found later not only in the Li-Si-Al-O-N system but also in Mg, Ca, Y-Si-Al-O-N systems [36,38-41]. The possible chemical reaction leading to these solid solutions is



Sialon ceramics not only maintain the excellent properties of silicon nitride or oxynitride but also promise better high temperature properties due to the incorporation of some constituents of the grain boundary phase into their crystal

lattices.

β' -sialon ceramics have been widely investigated [42-45], and some commercial products are available now, mainly as wear parts, extrusion dies, weld location pins and turbocharger rotors. However, research of α' -sialon ceramics is still in the early stage. Recently they have attracted more and more attention world-wide [42,46-50], because they promise excellent mechanical properties and good thermal shock resistance. α' -sialons have the α -silicon nitride type structure with two interstitial sites per unit cell, cations like Li, Ca, Y or rare-earth ions can be accommodated into the crystal lattice. Thus in principle the constituents of the liquid phase can be absorbed into the final ceramics. These materials therefore offer the possibility to develop nitrogen ceramics with clean grain boundaries.

However, in practice, the high nitrogen content (see chapter two) results in a small amount of high viscosity oxynitride liquid. Furthermore, the liquid constituents are gradually absorbed into the crystal lattice of the final products during firing. Therefore the complete formation and full densification of α' -sialons are very difficult to achieve. At this moment the complicated interrelationships between the formation sequence, fabrication conditions, properties, and microstructures are still insufficiently understood. Further systematical studies on α' -sialons therefore are necessary [51]. Furthermore, some advanced sintering techniques, such as gas pressure sintering and hot isostatic pressing, are considered to be methods to overcome the difficulty of the completion of the formation of α' -sialons [52].

1-3. OUTLINE OF THIS THESIS

The primary objectives of the present investigation are twofold. Firstly, to get a better understanding of the interrelationships among the chemical compositions, powder characteristics, sintering parameters, microstructure and properties of yttrium- α' -sialon ceramics. Secondly, to achieve fully dense α' -sialon ceramics by using optimized gas pressure sintering parameters. Composite $\alpha'+\beta'$ -sialon ceramics are also included in this thesis.

Chapter two reviews the fundamentals of α' -sialons, including the structure of silicon nitride, crystal chemistry and phase equilibria concerning α' -sialons. Besides, the representation of sialon systems is described as well.

Experimental procedures are outlined in chapter three, consisting of the composition and properties of the raw materials used, the preparation of specimens, the sintering set up, and the evaluation methods of the microstructure and properties of the sintered products. The variation of the oxygen impurity content in the silicon nitride starting powders during the powder processing is emphasized.

In chapter four, the reaction sequences of the formation of α' -sialon and the densification behaviour are followed by means of X-ray diffraction (XRD) and in-situ dilatometry, respectively. Also the microstructure evolution is studied. Further, the effects of the characteristics of the starting silicon nitride powders and the addition of some oxides to the mixtures are investigated as well.

In chapter five, gas pressure sintering is employed as a method to achieve the completion of the formation and densification of α' -sialon ceramics, and the process has been optimised by use of a statistical evaluation method. The influences of high pressure nitrogen gas, crucibles and bed powders used on the composition and microstructure of the final products are discussed.

The microstructure analysis, by using the XRD, the neutron powder diffraction, optical microscope (OM), scanning electron microscope (SEM) and transmission electron microscope (TEM), are presented in chapter six. The evaluation of both mechanical properties, such as Vickers hardness, fracture toughness, biaxial bending strength and wear resistance, and oxidation resistance of α' -sialon ceramics at various oxidation conditions are followed.

Final summary and conclusions are presented in chapter seven.

1-4. REFERENCES

1. Collins, J.F. and Gerby, R.W., *J. Met.*, 1955,7,612.
2. Sage, A.M. and Histed, J.H., *Powder Metall.*, 1961,4,196.
3. Parr, N.L., *Research (London)*, 1960,13,261.
4. Popper, P. and Ruddlesden, S.N., *Trans. Brit. Ceram. Soc.*, 1961,60,603.
5. Schützenberger, P., *Compt. rend.* 1879,2,644.
6. Schützenberger, P. and Colson, A., *Compt. Rend.* 1881,92b,1508.
7. Weiss, L. and Engelhardt, T., *Z. Anorg. Chem.*, 1910,65,38.
8. Deeley, C.G., Herbert, J.M. and Moore, N.C., *Powder Metall.*, 1961,4,145.

9. See, for instance, High-tech Ceramics, ed. Vincenzini, P., 1987, Elsevier Science Publishers B.V., Amsterdam.
10. See, for instance, Progress in Nitrogen Ceramics, ed. Riley, F.L., 1983, NATO ASI Series E65, Martinus Nijhoff, The Hague.
11. Kijima, K. and Shirasaki, S., J. Chem. Phys., 1976,65,2668.
12. Kunz, K.P., Sarin, V.K., Davis, R.F. and Bryan, S.R., Mater. Sci. and Eng., 1988,A105/106,47.
13. Batha, H.D. and Whitney, E.D., J. Am. Ceram. Soc., 1973,56,365.
14. Cooper, A.R. and Major, L.D., NTIS, Rep. AD-A-069004, 1979.
15. Wuensch, B.J. and Vasilos, T., NTIS, Final rep. Ad-A-021175, 1975.
16. Gazza, G.E., J. Am. Ceram. Soc., 1973,56,662.
17. Loehmen, R.E. and Rowcliffe, D.J., J. Am. Ceram. Soc., 1980,63,144.
18. Mazdiyasi, K.S. and Cooke, C.M., J. Am. Ceram. Soc., 1974,57,536.
19. Huseby, I.C. and Petzow, G., Powder Metall. Int., 1974,6,16.
20. Negita, K., J. Mater. Sci. Lett., 1985,4,755.
21. Ueno, K. and Toibana, T., Yogyo-kyokai-Shi, 1983,91,409.
22. Xu, Y.R., Huang, L.P., Fu, X.R. and Yan, D.S., Scientia Sinica, 1985,A28,556.
23. Hirosaki, N., Okada, A. and Matoba, K., J. Am. Ceram. Soc., 1988,71,C-144.
24. Greskovich, C. and O'Clair, C.R., U.S. Patent No.93687, 1977.
25. Lange, F.F., J. Am. Ceram. Soc., 1973,56,445.
26. Prochazka, S. and Greskovich, C.D., Rept. AMMRC-TR78-32, 1978, SRD-77-178.
27. Greskovich, C.D., Prochazka, S. and Rosolowski, D.H., Rept. APML-TR-76-179, 1976, SRD-76-151.
28. Singhal, S.C., Ceram. Int., 1976,2,123.
29. Raider, S.I., Flitsch, R., Aboof, J.A. and Plisken, W.A., J. Electrochem. Soc., 1976,123,560.
30. Raj, R. and Lange, F.F., Acta Metall., 1981,29,1993.
31. Raj, R., J. Am. Ceram. Soc., 1981,64,245.
32. Clarke, D.R., Progress in Nitrogen Ceramics, ed. Riley, F.L., 1983, p341, NATO ASI Series E65, Martinus Nijhoff, The Hague.

33. Oyama, Y. and Kamigaito, O., Jappan J. Appl. Phys., 1971,10,1637.
34. Oyama, Y., Jappan J. Appl. Phys., 1972,11,760.
35. Oyama, Y., Yogyo-Kyokai-Shi, 1974,82,351.
36. Jack, K.H. and Wilson, W.I., Nature Phys. Sci., 1972,238,28.
37. Jack, K.H., Trans. J. Brit. Ceram. Soc., 1973,72,376.
38. Jama, S.A.B.,Thompson, D.P. and Jack, K.H., Special Ceramics 6, ed. Popper, P., 1975, p299. B.C.R.A.,Stoke-on-Trent.
39. Jack, K.H., J. Mater. Sci., 1976,11,1135.
40. Masaki, H., Oyama, Y. and Kamigaito, O., Jappan. J. Appl. Phys., 1975,14,301.
41. Mitomo, M., Yogyo-Kyokai-Shi, 1977,85,50.
42. Jack, K.H., Non-oxide Technical and Engineering Ceramics, ed. Hampshire, S., 1986, p1, Elsevier Applied Sciences.
43. Lewis, M.H. and Lumby, R.J., Powder Metall., 1983,26,73.
44. Lumby, R.J., Butler, B. and Lewis, M.H., Progress in Nitrogen Ceramics, ed. Riley, F.L., 1983, p683, NATO ASI Series E65, Martinus Nijhoff, The Hague.
45. Lewis, M.H., Bhatti, A.R., Lumby, R.J. and North, B., J. Mater. Sci., 1980,15,103.
46. Jack, K.H., Progress in Nitrogen Ceramics, ed. Riley, F.L., 1983, p45, NATO ASI Series E65, Martinus Nijhoff, The Hague.
47. Jack, K.H., Alloying, eds. Walter, J.L., Jackson, M.R. and Sims, C.T., 1988, p447, ASM International Metals Park, Ohio 44073.
48. Ekström, T., Ingelström, N., Brage, R., Hatcher, M. and Johansson, T., J. Am. Ceram. Soc., 1988,71,1164.
49. Boskovic, S. and Nickel, K.G., Euro-Ceramics, eds. de With, G., Terpstra, R.A. and Metselaar, R., 1989, p441, Elsevier Applied Science.
50. Slasor, S., Liddell, K. and Thompson, D.P., Special Ceramics 8, eds. Howlett, S.P. and Taylor, D., 1986, p51, The Institute of Ceramics, Stoke-on-Trent.
51. Cao, G.Z. and Metselaar, R., to be published in Chemistry of Materials.
52. Cao, G.Z., Metselaar, R. and Ziegler, G., Euro-ceramics, eds. de With, G., Terpstra, R.A. and Metselaar, R., 1989, p346, Elsevier Applied Science.

CHAPTER TWO. FUNDAMENTALS OF α' -SIALONS

2-1. INTRODUCTION

The fundamentals of α' -sialons has been extensively studied and are well documented in literature [1-4]. The following summarizes the basic knowledge concerning α' -sialons, including the structure of silicon nitride, the crystal chemistry of sialons and the phase relationships in the various systems studied. However, the work on the preparation, microstructure, and properties of α' -sialon ceramics is very limited, and consequently excluded in this chapter.

2-2. STRUCTURE OF α and β - Si_3N_4

Silicon nitride occurs in two modifications, known as α and β . The structures of both α - and β - Si_3N_4 have been reported in a number of papers [5-15]. The building units are SiN_4 tetrahedra forming a corner shared three dimensional structure. The tetrahedra are linked with one edge parallel and one edge perpendicular to the (0001) plane of the hexagonal structures. Although the tetrahedra are slightly distorted, the Si_3N groups perpendicular to the basal plane lie approximately in a plane. The β -structure as shown in Fig. 2-1 is obtained from an ABAB.... stacking of these planes. The resulting space group is P63/m, with $a = 0.759\text{-}0.761$ nm and $c = 0.271\text{-}0.292$ nm. In this structure there are continuous channels parallel to the c-direction.

The α -structure is obtained from an ABCD stacking of the planes (Fig. 2-1). The resulting structure has space group P31c, with $a = 0.775\text{-}0.777$ nm and $c = 0.516\text{-}0.569$ nm. Due to the c-glide plane connecting the AB layers with the CD layers the channels are closed. As a result there are, in each unit cell $\text{Si}_{12}\text{N}_{16}$, two large interstitial sites at $2/3, 1/3, 3/8$ and $1/3, 2/3, 7/8$. To form the α -structure the tetrahedra have to be distorted and tilted, producing some strain in the network.

The characteristics of α and β -silicon nitride have been discussed widely, yet some uncertainties have remained in literature:

α -silicon nitride was considered to be a silicon oxynitride with the formula $\text{Si}_{11.5}\text{N}_{15.5}\text{O}_{0.5}$ and with some special lattice sites for the oxygen atoms [9,10,16].

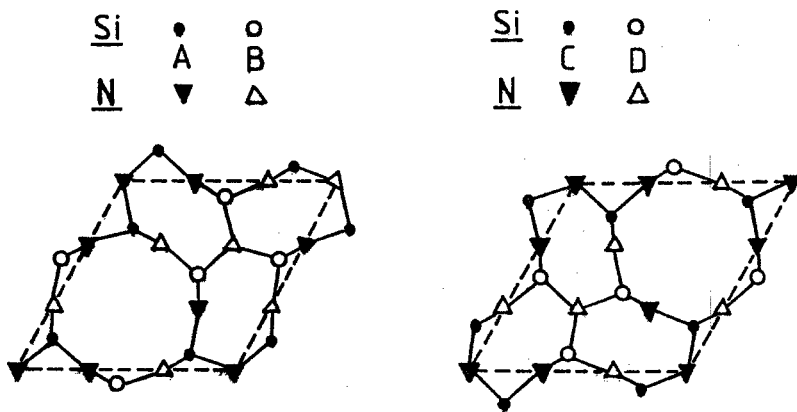


Fig. 2-1: AB and CD Si-N layers in silicon nitride. The stacking sequence in the α -modification is ABCD... and in the β -modification ABAB...[3].

However, later chemical analyses [17-18] and refined structural analyses [19-21] suggested that α -silicon nitride is a pure silicon nitride. Although this view has been generally accepted some recent reports [22-23] revealed that oxygen impurities in silicon nitride powders, which consist mainly of α -silicon nitride, exist not only in the surface layer but also in the bulk of the particles. So whether α -silicon nitride is an oxynitride or a pure nitride is still uncertain. There is no doubt that β -silicon nitride is a pure nitride [18-19].

There is also some uncertainty about the stability of the two phases. According to [24-25] α -silicon nitride is a low temperature modification while β -silicon nitride is a high temperature one. Thermodynamic data [26-35] obtained so far are not sufficiently accurate to make a decision. Since the $\beta \rightarrow \alpha$ phase transformation is never observed, it is assumed that β -silicon nitride is more stable at all temperatures, while α -silicon nitride is only formed under special conditions for kinetic reasons during the nitridation of silicon. This would also be in accordance with what one would expect on basis of the higher strain in the α -

structure.

The α to β -phase transformation is a reconstructive transformation, which requires a considerable activation energy for the breaking of Si-N bonds [25,36-39]. A solution precipitation mechanism is suggested: Dissolution of α in a liquid phase and precipitation of β from the liquid at elevated temperatures [40-44]. This $\alpha \rightarrow \beta$ phase transformation starts very slowly at about 1400°C and completes close to 1800°C only in the presence of a liquid phase. Earlier theories of transformation in the solid state as well as a desoxidation reaction are no longer considered [45-46], and also a possible transformation via the gas phase is not observed.

2-3. CRYSTAL CHEMISTRY OF α' -SIALON

Solid solutions with the β -type structure are formed only with aluminium and beryllium by a limited substitution of Si^{4+} by Al^{3+} or Be^{2+} and of N^{3-} by O^{2-} [1-4, 47-51]. The cation to anion ratio remains constant at 3 to 4 and no constitutional vacancies are formed. The aluminium substitution leads to $\text{Si}_{6-z}\text{Al}_z\text{O}_z\text{N}_{8-z}$ with $0 \leq z \leq 4.2$. In the case of beryllium the formula is $\text{Si}_{6-z}\text{Be}_z\text{O}_{2-z}\text{N}_{8-2z}$ with $0 \leq z \leq 2$. The β' -sialons can thus be described as solid solutions between Si_3N_4 and $\text{Al}_3\text{O}_3\text{N}$, the β' -sibeons between Si_3N_4 and Be_2SiO_4 .

In contrast to the purely substitutional solubility in the β' -phase, in the α -silicon nitride structure there are two interstitial sites per unit cell which can be occupied by cations (see Fig. 2-2). So the formation of solid solutions in the α -silicon nitride type structure occurs only in quinary Me-Si-Al-O-N systems where Me = Li, Mg, Ca, Y and rare-earth metals except La and Ce [1-4,52-57]. Fig. 2-3 shows a schematic phase diagram of the Me-Si-Al-O-N system with the plane containing the α' -sialon stability region [3].

The α' -sialon crystal structure is derived from α - $\text{Si}_{12}\text{N}_{16}$ by partial replacement of Si^{4+} by Al^{3+} and stabilized by trapping "modifying" cations such as Li, Ca, Y in the interstices of the [Si,Al]-[O,N] network. In Y- α' -sialon, the coordination of the Y^{3+} cation is shown in Fig. 2-4. This figure indicates that the Y^{3+} atom is surrounded by seven (N,O)-atom sites with three different Y-(N,O) distances. A polar three-fold rotation axis exists in the [0001] direction, which is also the direction of the shortest Y-(N,O) distance [58-59].

If α' -sialon is synthesized entirely from nitrides the products should contain

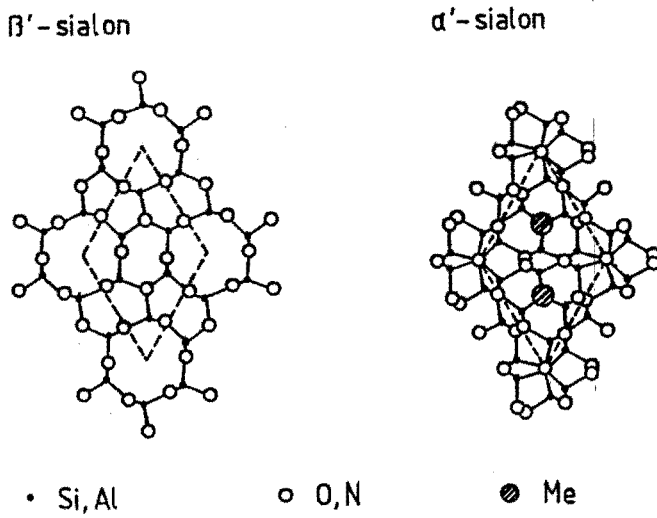


Fig. 2-2: Projections of the α' - and β' -sialon crystal structure perpendicular to the c-axis [56].

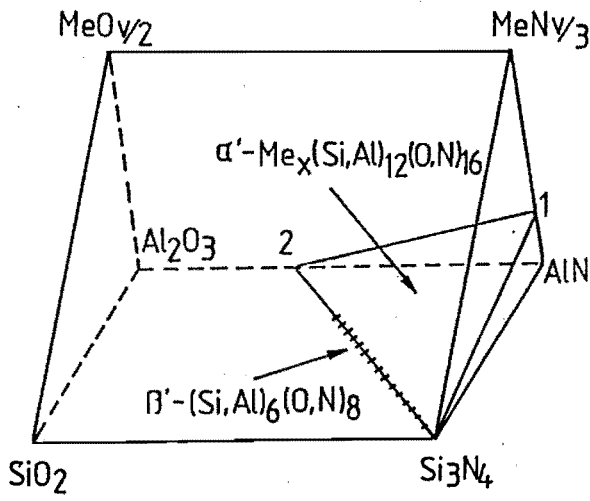


Fig. 2-3: A schematic phase diagram of the α' - and β' -sialon stability regions, Me is a metal ion with valency v.
 1. $\text{Me}_{3/v}\text{Al}_3\text{N}_4$ 2: $\text{Al}_3\text{O}_3\text{N}$

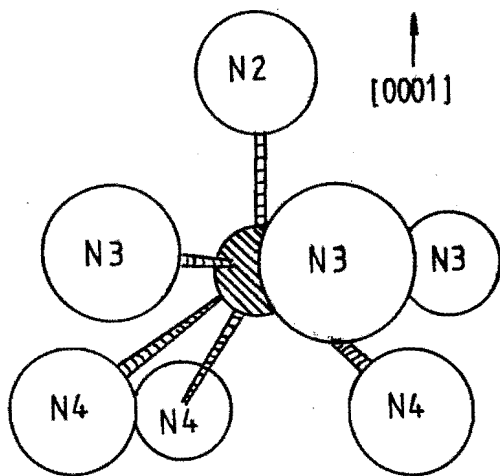
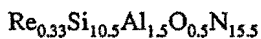
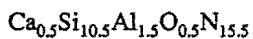


Fig. 2-4: The coordination of the Y^{3+} cation in α' -sialon [58,59].

no oxygen and thus valency compensation is due solely to the introduction of the modifier cations. Because there are only two sites per unit cell for these, the upper limiting compositions for α' -sialons with a v-valent metal ion are expected to be $Me_2Si_{12-2v}Al_{2v}N_{16}$, e.g. $Li_2Si_{10}Al_2N_{16}$, $Ca_2Si_8Al_4N_{16}$ and $Y_2Si_6Al_6N_{16}$. These limits have not been reached, which may be due to the presence of oxygen in the silicon nitride particles. The highest solubility has been reported to be 1.83 Ca^{2+} per cell in Ca- α' -sialon with a composition of $Ca_{1.83}Si_{8.34}Al_{3.66}N_{16}$ [3] and 1.5 Li^+ in Li- α' -sialon on the line Si_3N_4 - Li_2O :3AlN [60], respectively. The upper limits of the solubility in α' -sialons generally decrease as the size of the modifying cations becomes larger, see Fig. 2-5 [61-62].

Earlier work on α' -sialons suggested a miscibility gap between α -silicon nitride and the α' -phase, the α' -sialon compositions closest to Si_3N_4 being:



here Re can be all rare-earth elements except La and Ce. To stabilize the structure, the equivalent of not less than half a cationic valency ($Ca_{0.25}$ or $Re_{0.16}$) was considered necessary in each of the two interstices [3, 5, 61-62]. However,

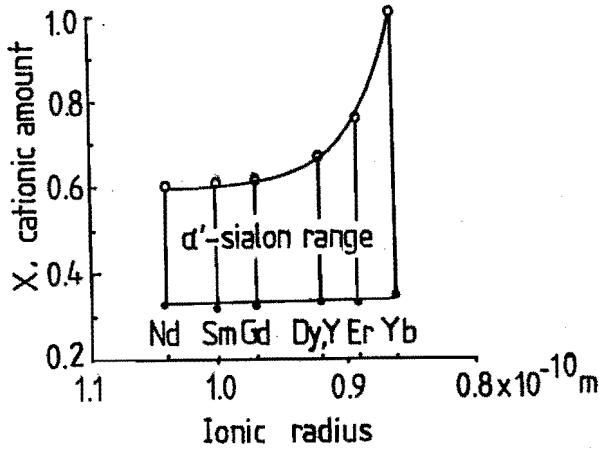
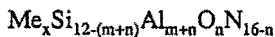


Fig. 2-5: Solubility of some modifying cations in α' -sialon: $Me_x(Si,Al)_{12}(O,N)_{16}$ [61,62].

later experimental results reveal some exceptions. In the Li- α' -sialon system the α' -phase composition closest to α -silicon nitride is $Li_{0.25}(Si,Al)_{12}(O,N)_{16}$, which indicates that only 0.125 cationic valency for each of the two interstices is sufficient to stabilize the α' -structure [60]. Similar results have been observed in the Si_3N_4 -AlN-CaO system [63].

Unlike in β' -sialon, $Si_{6-z}Al_zO_2N_{8-z}$, where the replacement without structure change is Si-N by Al-O, the replacement in α' -sialon is largely Si-N by Al-N. With bond lengths Si-N: 0.174 nm, Al-O: 0.175 nm and Al-N: 0.187 nm, the relative increases in unit cell dimensions for $\alpha \rightarrow \alpha'$ are much larger than for $\beta \rightarrow \beta'$. For a general composition:



$m(Al-N)$ replaces $m(Si-N)$ and $n(Al-O)$ replaces $n(Si-N)$. The change of the cell dimensions fit reasonably with the relationships [3, 5]:

$$\Delta a \text{ (pm)} = 4.5m + 0.9n$$

$$\Delta c \text{ (pm)} = 4.0m + 0.8n.$$

This suggests that the dimensional increase upon replacement of (Si-N) by (Al-N)

is about five times that for replacement by (Al-O). The size and solubility of the modifying cations does not influence the dimension expansion of α' -sialon. Possibly the interstitial holes are large enough to accommodate those cations.

2-4. REPRESENTATION OF SIALON SYSTEMS

Most sialons are quaternary or quinary systems due to the addition of oxides for both liquid phase sintering and structure modification. The study of phase relationships is very important to understand the reactions. Before we consider these, we will first discuss the representation of sialon systems, which was introduced first by Gauckler et al. [49,64] for the representation of the Si_3N_4 -AlN-SiO₂-Al₂O₃ system and Huseby et al. [47] for the Si_3N_4 -SiO₂-Be₃N₂-BeO system. A detailed discussion is given by Jack [1].

The Si-Al-O-N system is an essential one for sialon systems. As a four component system it might be represented by a regular tetrahedron, each corner representing one atom of the elements. Although the bonding in the sialons is predominantly covalent, there is a great advantage in assuming normal charges for the elements and using charge equivalents. Using the tetrahedral representation as shown in Fig. 2-6, there are 12 charge equivalents along each side of the tetrahedron. The requirement of charge neutrality is obeyed only at the midpoints of each side of the tetrahedron. These four points, with composition Si₃O₆, Al₄O₆, Al₄N₄ and Si₃N₄, therefore lie at the corners of a square. All compositions of four valent silicon, three valent aluminium and nitrogen, and two valent oxygen lie on this plane. Fig. 2-7 shows the phase diagram of the Si_3N_4 -SiO₂-AlN-Al₂O₃ system at 1700°C [65]. The β' -sialon compositions, which extend from the Si₃N₄ corner, are indicated in this diagram.

Let us next look at the α' -sialon diagrams i.e. in the Me-Si-Al-O-N quinary systems. A simple representation is again obtained by using atom equivalents. This leads to the so-called Jänecke triangular prism [66-68], in which all edges, expressed in equivalent units, are equal. Fig. 2-8 shows the prism of the Si_3N_4 -SiO₂-AlN-Al₂O₃-YN-Y₂O₃ system. It is based on the usual square diagram of the Si_3N_4 -SiO₂-AlN-Al₂O₃ system extending to the third dimension by the addition of yttrium. This forms two more squares of the AlN-Al₂O₃-YN-Y₂O₃ and Si_3N_4 -SiO₂-YN-Y₂O₃ systems. The triangular face at the left-hand side is the

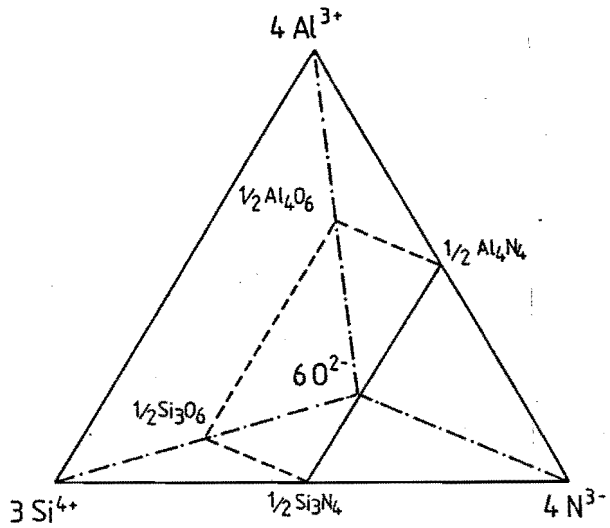


Fig. 2-6: A regular tetrahedron representation of the Si-Al-O-N system; each corner represents 12 equivalent charges. The Si_3N_4 -AlN-SiO₂-Al₂O₃ subsystem forms a two-dimensional square plane in this representation (see Fig. 2-7).

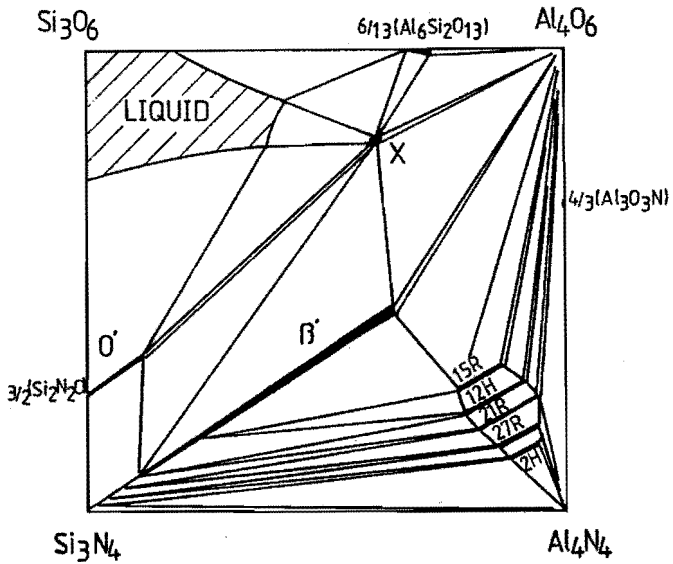


Fig. 2-7: Phase diagram of the Si_3N_4 -SiO₂-AlN-Al₂O₃ system at 1700° [65].

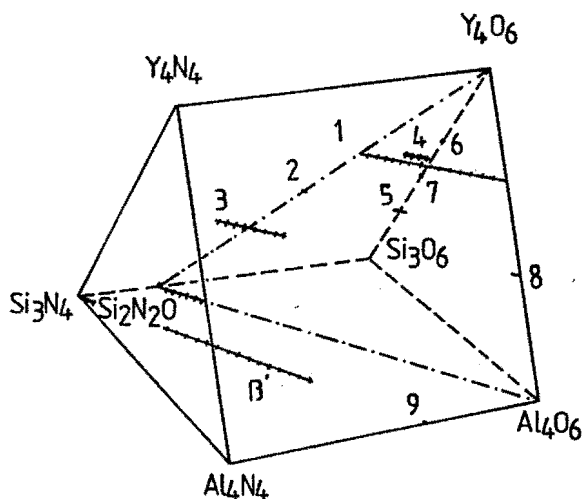


Fig. 2-8: The Jänecke prism for the Y-Si-Al-O-N system [4].

- | | |
|-----------------------------|-----------------------------|
| 1: $2Y_2O_3 \cdot Si_2N_2O$ | 6: Y_2SiO_5 |
| 2: $Y_2O_3 \cdot Si_2N_2O$ | 7: $Y_2Si_2O_7$ |
| 3: $Y_2O_3 \cdot Si_3N_4$ | 8: $3Y_2O_3 \cdot 5Al_2O_3$ |
| 4: $Y_{10}(SiO_4)_6N_2$ | 9: Al_3O_3N |
| 5: Y_2SiAlO_5N | |

nitride system and at the right-hand side the oxide system.

Although the representation mentioned above has led to much better understanding and easier interpretation of experimental observations, phase relationships in Me-Si-Al-O-N quinary systems are very complicated and so most reports deal only with some triangular planes by cutting of the Jänecke prism, e.g. Si_2N_2O - Al_2O_3 - Y_2O_3 , Si_3N_4 - SiO_2 - Y_2O_3 planes [69-71].

2-5. PHASE RELATIONSHIPS CONCERNING α' -SIALON

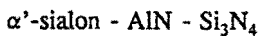
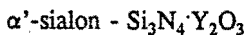
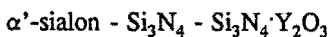
When using phase diagrams for nitride and oxynitride systems some points should be kept in mind. In the first place one should be aware that most phase diagrams of nitride and oxynitride systems do not represent thermodynamical equilibrium phase relationships. Due to the low self-diffusivity in silicon nitride, a small fraction of glassy grain-boundary phase is always present but is not considered in the phase diagrams. Furthermore, only major solid phases are

considered, while the presence and influence of vapour phases and a small amount of impurities are normally ignored. Also an accurate determination of the composition is difficult due to the presence of the light elements oxygen and nitrogen.

In spite of these limitations the knowledge of these diagrams is an essential basis for the fabrication of nitride and oxynitride ceramics. This is the more so since the presence of secondary phases influences the microstructure, and the resulting properties of the final products.

However, the number of phase equilibrium studies on α' -sialon systems is very limited. Some important diagrams will be discussed here. Several studies discuss the formation of α' -sialons along the $\text{Si}_3\text{N}_4\text{-M}_x\text{O}_y\text{:mAlN}$ join. However, as early as the appearance of the phase diagram of the $\text{Si}_3\text{N}_4\text{-AlN-Y}_2\text{O}_3$ system [72], the existence of a two-dimensional region of α' -sialon stability was proposed (see Fig. 2-3) and a tentative Ca- α' -sialon phase diagram was reported by Jack in the Ca-Si-Al-O-N system [3].

We will first discuss the phase relationships in the Y-Si-Al-O-N system which is one of the most detailed α' -sialon system known so far [56,59,72-75]. The general formula for the Y- α' -sialons is $\text{Y}_x\text{Si}_{12-(m+n)}\text{Al}_{m+n}\text{O}_n\text{N}_{16-n}$, where $x = m/3$, and m and n are independent parameters. The phase diagram of the $\text{Si}_3\text{N}_4\text{-AlN-Y}_2\text{O}_3$ system is the first complete α' -sialon diagram studied (see Fig. 2-9) [72], in which α -silicon nitride forms a limited solid solution with a mixture of $\text{Y}_2\text{O}_3\text{:9AlN}$. The solubility limits along this line are represented by $0.33 \leq x \leq 0.67$. Silicon nitride also reacts with Y_2O_3 to form $\text{Si}_3\text{N}_4\text{Y}_2\text{O}_3$ and $\text{Si}_2\text{N}_2\text{O}_2\text{Y}_2\text{O}_3$, the latter of which does not lie on the plane of $\text{Si}_3\text{N}_4\text{-AlN-Y}_2\text{O}_3$. Five compatibility triangles containing α' -sialon were observed:



More detailed phase relationships in the system were studied on the $\text{Si}_{12}\text{N}_{16}\text{-Y}_4\text{Al}_{12}\text{N}_{16}\text{-Si}_4\text{Al}_8\text{O}_8\text{N}_8$ concentration plane at 1700°C , and the diagrams are shown in Figs. 2-10 and 2-11 [56,59,73-75]. According to the diagrams the

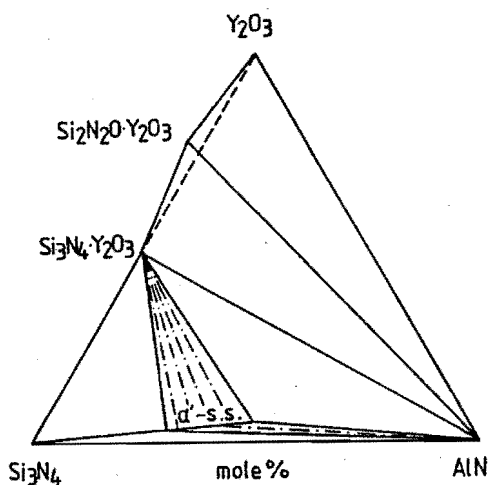


Fig. 2-9: Subsolidus diagram of the $\text{Si}_3\text{N}_4\text{-AlN-Y}_2\text{O}_3$ system [72].

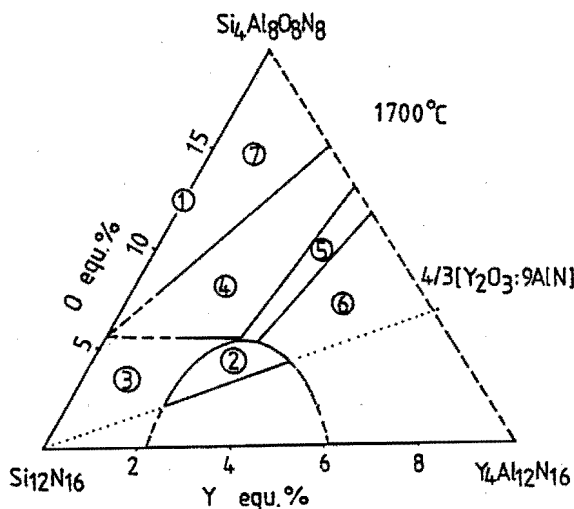


Fig. 2-10: Phase relations in the concentration plane $\text{Si}_{12}\text{N}_{16}\text{-Y}_4\text{Al}_8\text{N}_{12}\text{-Si}_4\text{Al}_8\text{O}_8\text{N}_8$ at 1700°C [56,59].

1: β' -sialon	5: α' -sialon + 12H
2: α' -sialon	6: α' -sialon + 21R
3: α' + β' -sialon	7: β' -sialon + 12H
4: α' + β' -sialon + 12H	

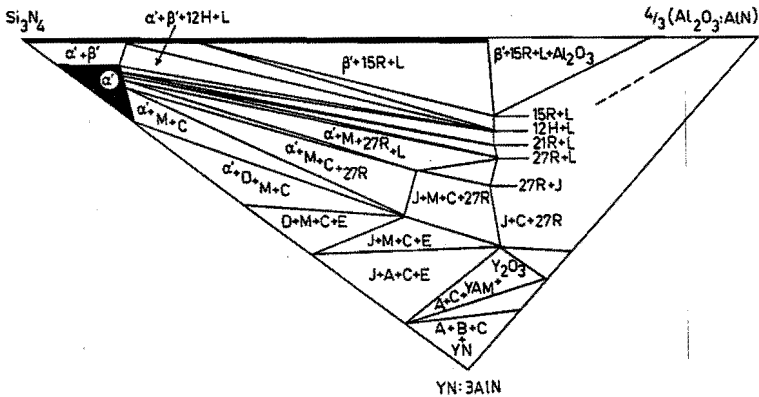


Fig. 2-11: Phase relations in the Y- α' -sialon plane at 1750°C [74,75].
 A: $Y_6Si_3N_{10}$ J: $Y_4Si_2O_7N_2$ - $Y_4Al_2O_9$ ss
 C: AlN L: Liquid
 D: YSi_3N_5 M: $Y_2Si_3O_3N_4$
 E: $Y_2Si_3N_6$

boundaries of the single phase α' -sialon region are: $0.33 \leq x \leq 1$ (Y) and $0.5 \leq n \leq 1.5$ (O). A discussion is given in [75].

The Si_3N_4 -AlN- Re_2O_3 systems exhibit phase diagrams similar to those shown in Fig. 2-9, when Re = Gd, Dy, Er and Yb [61-62]. The phase diagrams of the Si_3N_4 -AlN- Nd_2O_3 and Sm_2O_3 systems are slightly different, since AlN reacts with Nd_2O_3 and Sm_2O_3 to form Nd_2AlO_3N and Sm_2AlO_3N , respectively (see Fig. 2-12). The solubility limits of α' -sialon in these systems have been plotted in Fig. 2-5. The lower limits are the same as for yttrium while the upper limits increase when the size of the modifier cations decreases.

Two dimensional phase relationships on the $Si_{12}N_{16}$ - $(Nd/Sm)_4Al_{12}N_{16}$ - $Si_4Al_8O_8N_8$ concentration plane were also studied [76]. Approximately the same phase relationships were reported as in Fig. 2-11.

The phase diagram of the Si_3N_4 -AlN-CaO system, shown in Fig. 2-13 [63], is very similar to that of the Si_3N_4 -AlN- Y_2O_3 system. Silicon nitride reacts with the mixture of CaO:3AlN to form solid solutions with compositions in the range

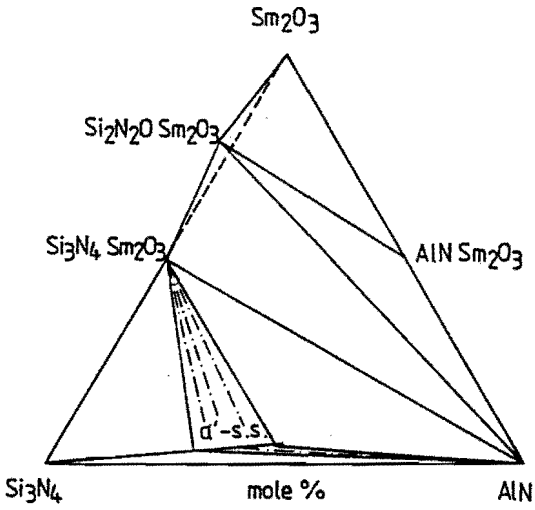


Fig. 2-12: Subsolidus diagram of the Si_3N_4 -AlN- Sm_2O_3 system [61,62].

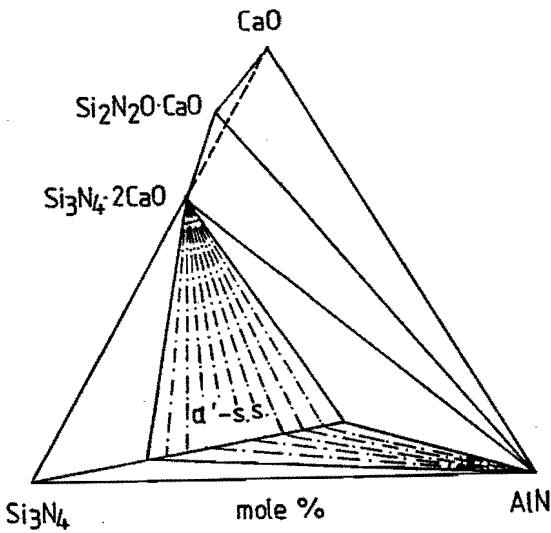


Fig. 2-13: Subsolidus diagram of the Si_3N_4 -AlN-CaO system [63].

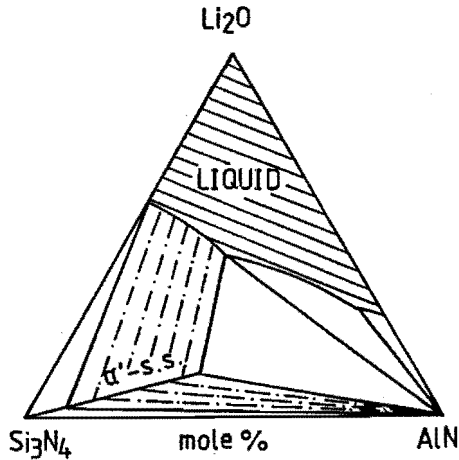


Fig. 2-14: Isothermal section at 1750°C of the Si_3N_4 -AlN- Li_2O system [60].

0.3 to 1.4 Ca per unit cell of α' -sialon. Silicon nitride also reacts with CaO resulting in the formation of $2\text{CaO}\cdot\text{Si}_3\text{N}_4$ and $3\text{CaO}\cdot\text{Si}_2\text{N}_2\text{O}$. Besides, at 1450°C a metastable phase of $2\text{CaO}\cdot\text{Si}_3\text{N}_4\cdot\text{AlN}$ was found as well.

The phase relationships of the Si_3N_4 -AlN- Li_2O system have also been reported recently [60]. So far single phase Li- α' -sialon has been found only on the line Si_3N_4 - Li_2O :3AlN (Fig. 2-14). Li- α' -sialon exhibits a large solubility range viz. from 0.25 Li to 1.50 Li per unit cell. The discrepancy here with previous work in literature has been discussed before. The composition $10\text{Li}_2\text{O}:\text{Si}_3\text{N}_4\cdot\text{AlN}$ has a liquidus temperature of only about 900°C. Some more detailed work is still required in this system.

The phase diagram of the Si_3N_4 -AlN-MgO system is another one studied recently [77]. However, in this system single phase Mg- α' -sialon has not been obtained on the line Si_3N_4 -MgO:3AlN. The phase compositions along this line with increasing amount of MgO:3AlN are mixtures of the phases $\beta' + \alpha'$, $\alpha' + 12\text{H}$ (AlN polytypoid) and $\alpha' + 12\text{H} + \text{AlN}$, respectively. It is suggested that the small Mg- α' -sialon region is located only at the nitrogen rich side [77], thus preparation of single phase Mg- α' -sialon might be possible by using Mg_3N_2 .

The compatibility between α' - and β' -sialon, indicates the possibilities for developing composite $\alpha'+\beta'$ -sialon ceramics with tailored properties by varying the α'/β' -ratio.

2-6. SUMMARY

In contrast to the well documented structure and crystal chemistry for α' -sialons, up to now only a very limited understanding of the preparation and characterization of α' -sialon ceramics has been achieved. For development of α' -sialon ceramics, it is essential to have a thorough understanding of the relationships among the material composition, microstructure and properties, since the mechanical and chemical properties, particularly the oxidation resistance, of nitrogen ceramics are microstructure sensitive.

2-7. REFERENCES

1. Jack, K.H., *J. Mater. Sci.*, 1976,11,1135.
2. Jack, K.H., Non-oxide Technical and Engineering Ceramics, Ed. Hampshire, S., 1986, p1, Elsevier Applied Science.
3. Jack, K.H., Progress in Nitrogen Ceramics, ed. Riley, F.L., 1983, p45, NATO ASI Series E65, Martinus Nijhoff, The Hague.
4. Jack, K.H., Alloying, eds. Walter, J.L., Jackson, M.R. and Sims, C.T., 1988, p447, ASM International Metals Park, Ohio 44073.
5. Hampshire, S., Park, H.K., Thompson, D.P. and Jack, K.H., *Nature*, 1978,274,880.
6. Hardie, D. and Jack, K.H., *Nature*, 1957,180,392.
7. Henderson, C.M.B. and Taylor, D., *Trans. J. Brit. Ceram. Soc.*, 1975,74,49.
8. Grieveson, P., Jack, K.H. and Wild, S., Special Ceramics 4, ed. Popper, P., 1968, p237, B.C.R.A., Stoke on Trent.
9. Wild, S., Grieveson, P. and Jack, K.H., Special Ceramics 5 ed. Popper, P., 1972, p385, B.C.R.A., Stoke on Trent.
10. Glemser, O., Beltz, K. and Naumann, P., *Z. Anorg. Allg. Chem.*, 1957,291,51.

11. Ruddlesden, S.N. and Popper, P., *Acta Cryst.*, 1958,11,465.
12. Borgen, O. and Seip, H.M., *Acta Chem. Scand.*, 1961,15,1789.
13. Marchand, R., Laurent, Y. and Lang, J., *Acta Cryst.*, 1969,B25,2157.
14. Grün, R., *Acta Cryst.*, 1979,B35,800.
15. Ziegler, G., Heinrich, J. and Wötting, G., *J. Mater. Sci.*, 1987,22,3041.
16. Feld, H., Ettmayer, P. and Petzenhauser, I.,
Ber. Dt. Keram. Ges., 1974,51,127.
17. Priest, H.F., Burns, F.C., Priest, G.L. and Skaar, E.C.,
J. Am. Ceram. Soc., 1973,56,395.
18. Edwards, A.J., Elias, D.P., Lindley, M.W., Atkinson, A.
and Moulson, A.J., *J. Mater. Sci.*, 1974,9,516.
19. Kohatsu, I. and McCauley, J.W., *Mater. Res. Bull.*, 1974,9,917.
20. Kato, K., Inoue, Z., Kijima, K., Kawada, I. and Tanaka, H.,
J. Am. Ceram. Soc., 1975,58,90.
21. Srinivasa, S.R., Cartz, L., Jorgensen, J.D., Worlton, T.G.,
Beyerlein, S.A. and Billy, M., *J. Appl. Cryst.*, 1977,10,146.
22. Peuckert, M. and Greil, P., *J. Mater. Sci.*, 1987,22,3717.
23. Petzow, G. and Sersale, R., *Pure and Appl. Chem.*, 1987,59,1673.
24. Thompson, D.P. and Pratt, P.L., *Science of Ceramics 3*, ed. Stewart, G.H.,
1967, p33, Academic Press, London.
25. Weiss, J., *Ann. Rev. Mater. Sci.*, 1981,11,381.
26. Singhal, S.C., *Ceram. Int.*, 1976,2,123.
27. Maignon, C., *Bull. Soc. Chim. France*, 1913,13,791.
28. Eriksson, G., *Chem. Scr.*, 1975,8,100.
29. Pehlke, W.B. and Elliott, J.P., *Trans. Met. Soc.*, 1959,AIME215,781.
30. Ryklis, E.A., Bolgar, A.S. and Fesenko, V.V.,
Sov. Powder Metall. Met. Ceram., 1969,73,73.
31. Wild, S., Grieveson, P. and Jack, K.H., *Special Ceramics 5*, ed. Popper, P.,
1972, p271, B.C.R.A., Stoke on Trent.
32. Colquhoun, J., Wild, S., Grieveson, P. and Jack, K.H.,
Proc. Brit. Ceram. Soc., 1973,22,207.
33. Blegen, K., *Special Ceramics 6*, ed. Popper, P., 1975, p223, B.C.R.A.,
Stoke on Trent.

34. Rayl, W.R. and Muan, A., *Science*, 1969,165,1363.
35. Hendry, A., Nitrogen Ceramics, ed. Riley, F.L., 1977, p183, NATO ASI Series, Noordhoff, Leyden.
36. Messier, D.R., Riley, F.L. and Brook, R.J., *J. Mater. Sci.*, 1978,13,1199.
37. Buerger, M.J., Phase Transformations in Solids, eds. Smoluchowski, R. et al., 1951, p183, Wiley, New York.
38. Messier, D.R. and Riley, F.L., Progress in Nitrogen Ceramics, ed. Riley, F.L., 1983, p141, NATO ASI Series E65, Martinus Nijhoff, The Hague.
39. Sarin, V.K., *Mater. Sci. Eng.*, 1988,A105/106,151.
40. Jack, K.H., Phase Diagrams: Materials Science and Technology, ed. Alper, A.M., 1978, p241, Academic Press, New York.
41. Bowen,L.J., Weston,R.J., Carruthers, T.G. and Brook, L.J., *J. Mater. Sci.*, 1978,13,341.
42. Bowen, L.J., Carruthers, T.G. and Brook, L.J., *J. Am. Ceram. Soc.*, 1978,61,335.
43. Drew, P. and Lewis, M.H., *J. Mater. Sci.*, 1974,9,261.
44. Priest, H.F., Burns, F.C., Priest, G.L. and Skaar, E., *J. Am. Ceram. Soc.*, 1973,56,395.
45. Wild,S., Grieveson, P., Jack,K.H. and Latimer.M.J., Special Ceramics 5, ed. Popper, P., 1972, p377. B.C.R.A., Stoke on Trent.
46. Evans, A.G. and Sharp, J. V., *J. Mater. Sci.*, 1971,6,1292.
47. Huseby, I.C., Lukas, H.L. and Petzow, G., *J. Am. Ceram. Soc.*, 1975,58,377.
48. Thompson, D.P. and Gauckler, L.J., *J. Am. Ceram. Soc.*, 1977,60,470.
49. Gauckler, L.J., Lukas, H.L. and Petzow, G., *J. Am. Ceram. Soc.*, 1975,58,346.
50. Naik, I.K., Gauckler, L.J. and Tien, T.Y., *J. Am. Ceram. Soc.*, 1978,61,332.
51. Lewis, M.H., Powell, B.D., Drew, P., Lumby, R.J., North, B. and Taylor, A.J., *J. Mater. Sci.*, 1977,12,61.
52. Jama, S.A.B., Thompson, D.P. and Jack, K.H., Special Ceramics 6, ed. Popper, P., 1975, p299, B.C.R.A., Stoke-on-Trent.
53. Mitomo, M., *Yogyo-Kyokai-Shi*, 1977,85,50.

54. Park, H.K., Thompson, D.P. and Jack, K.H., Science of Ceramics 10, ed. Hausner, H., 1980, p251, DGK.
55. Grand, G., Demit, J., Ruste, J. and Torre, J.P.,
J. Mater. Sci., 1979,14,1749.
56. Greil, P., Nagel, A., Stutz, D. and Petzow, G., Presented at German-Yugoslavian Symposium on Advanced Materials, April, 1985, BRD.
57. Ukyo, Y and Wada, S., Euro-Ceramics, eds. de With, G., Terpstra, R.A. and Metselaar, R., 1989, p566, Elsevier Applied Science.
58. Izumi, F., Mitomo, M. and Suzuki, J., J. Mater. Sci. Lett., 1982,1,533.
59. Stutz, D., Greil, P. and Petzow, G., J. Mater. Sci. Lett., 1986,5,335.
60. Kuang, S.F., Huang, Z.K., Sun W.Y. and Yan, D.S.,
J. Mater. Sci. Lett., 1990,9,72.
61. Huang, Z.K., Tien, T.Y. and Yan, D.S.,
J. Am. Ceram. Soc., 1986,69,C-241.
62. Huang, Z.K., Yan, D.S. and Tien, T.Y., J. Inorg. Mater., 1986,1,55.
63. Huang, Z.K., Sun, W.Y. and Yan, D.S., J. Mater. Sci. Lett., 1985,4,255.
64. Gauckler, L.J. and Petzow, G., Nitrogen Ceramics, ed. Riley, F.L., 1977,
p183, Noordhoff, Leyden.
65. Thompson, D.P., Sun, W.Y. and Walls, P.A., Ceramic Materials and Components for Engines, eds. Bunk, W. and Hausner, H., 1986, p643,
DKG, Berlin.
66. Zernike, J., Chemical Phase Theory, 1955, Kluwer, Deventer,
the Netherlands.
67. Löwenherz, R., Z. Phys. Chem., 1894,13,459.
68. Jännecke, E., Z. Phys. Chem., 1908,51,132.
69. Cao, G.Z., Huang, Z.K., Fu, X.R. and Yan, D.S.,
Int. J. High-techn. Ceram., 1985,1,119.
70. Lange, F.F., Singhal, S.C. and Kurnicki, R.C.,
J. Am. Ceram. Soc., 1977,60,249.
71. Huang, Z.K., Greil, P. and Petzow, G., Ceram. Int., 1984,10,14.
72. Huang, Z.K., Greil, P. and Petzow, G., J. Am. Ceram. Soc., 1983,66,C-96.
73. Stutz, D., Ph.D. Thesis, Institut für Metallkunde der Universität Stuttgart,
1986, D-7000 Stuttgart, FRG.

74. Slasor, S. and Thompson, D.P., Non-oxide Technical and Engineering Ceramics, ed. Hampshire, S., 1986, p223, Elsevier Applied Science.
75. Slasor, S. and Thompson, D.P., *J. Mater. Sci. Lett.*, 1987,6,315.
76. Hampshire, S., O'Reilly, K.P.J., Leigh, M. and Redington, M., High-techn Ceramics, ed. Vincenzini, P., 1987, p933, Elsevier Science Publishers B.V., Amsterdam.
77. Kuang, S.F., Huang, Z.K., Sun, W.Y. and Yan, D.S., *J. Mater. Sci. Lett.*, 1990,9,69.

CHAPTER THREE. EXPERIMENTAL PROCEDURES

3-1. RAW MATERIALS

For all experiment described in this thesis the following powders have been chosen as starting materials: Si_3N_4 (LC-12, Starck), AlN (Grade C, Starck), Al_2O_3 (99.99%, Baikalox CR 10), Y_2O_3 (99.99%, Ventron) and La_2O_3 (99.99%, Fluka AG). Their chemical compositions and properties are given in Table 3-1. The silicon nitride and aluminium nitride are extra fine nitride powders with a very low content of metallic impurities, while the oxygen content in both silicon nitride and aluminium nitride is relatively high, i.e. 1.57 wt% and 1.80 wt%, respectively.

Due to the relatively high free energy of formation of silica, silicon nitride will be oxidized to silica and/or silicon oxynitride in either oxygen or water-containing atmosphere. Surfaces of silicon nitride powders have been found to be covered with an oxygen-rich layer [1-4] (normally the thickness of this layer is less than 10 nm). Oxygen is also proposed to dissolve into the bulk of silicon nitride up to approximately 0.8 wt% content [2]. Therefore, the oxygen impurity in silicon nitride powders is always present, and in general, it increases with the particle surface area. Similar conclusions apply in the case of AlN powders [5-6].

For a better understanding of the influence of the starting silicon nitride powders on the formation and densification of α' -sialon ceramics, two other laboratory grade silicon nitride powders, DFV0014 and DFV0015 have been used, of which the chemical compositions and properties are given in Table 3-2. DFV0015 powder has the lowest oxygen impurity content of 0.34 wt%, which is approximately five times less than that of the LC-12 powder. The α -phase contents in both DFV0014 and DFV0015 powders are lower than that in LC-12 powder. Although the mean particle size of the three silicon nitride powders is quite similar, the particle size distribution exhibits some differences (see Fig. 3-1). In contrast to the silicon nitride powder from Bayer the LC-12 powder shows a relatively wide distribution in particle size. The morphology of the powders is shown in Fig. 3-2.

Table 3-1: Chemical compositions and properties of raw materials as given by the supplier

Si ₃ N ₄	LC-12, HCST,	Starck Berlin
	N: 38.50 wt%	Fe: 0.005 wt%
	C: 0.18 wt%	Al: 0.044 wt%
	O: 1.90 wt%	Ca: 0.004 wt%
	1.57 wt%*	
	FSSS: 0.55 μm	
	BET: 21.1 m ² /g	
α/(α+β): > 95%		
AlN	Grade C, HCST,	Starck Berlin
	Al: >64.0 wt%	O: 2.0 wt%
	N: 33.6 wt%	1.80 wt%*
	C: 0.007 wt%	Fe: < 0.008 wt%
	FSSS: 0.9 μm	
	BET: 5.2 m ² /g	
Al ₂ O ₃	Baikalox CR 10	
	Purity: 99.99 %	
	BET: 10 m ² /g	
	α-Al ₂ O ₃ : > 90 %	
Y ₂ O ₃	Ventron	
	Purity: 99.99%	
La ₂ O ₃	Fluka AG	
	Purity: 99.99%	

* : our analysis results

FSSS: mean particle size as determined by using Fisher Subsieve Sizer

BET: surface area as determined by N₂ adsorption

Table 3-2: Comparison of the chemical composition and properties of the starting silicon nitride powders #

	LC-12	DFV0014*	DFV0015*
O	1.57 wt%	1.10 wt%	0.34 wt%
C	0.18 wt%	0.12 wt%	0.12 wt%
Fe	50 ppm	71 ppm	15 ppm
Al	44 ppm	12 ppm	8 ppm
Ca	4 ppm	3 ppm	3 ppm
$\alpha/(\alpha+\beta)$	95%	71%	73%
FSSS	0.55 μm	0.66 μm	0.53 μm

*: Data from suppliers.

*: Laboratory grade, by courtesy of Dr. G. Wötting, Cremer Forschungsinstitut GmbH, Rödingtal, FRG.

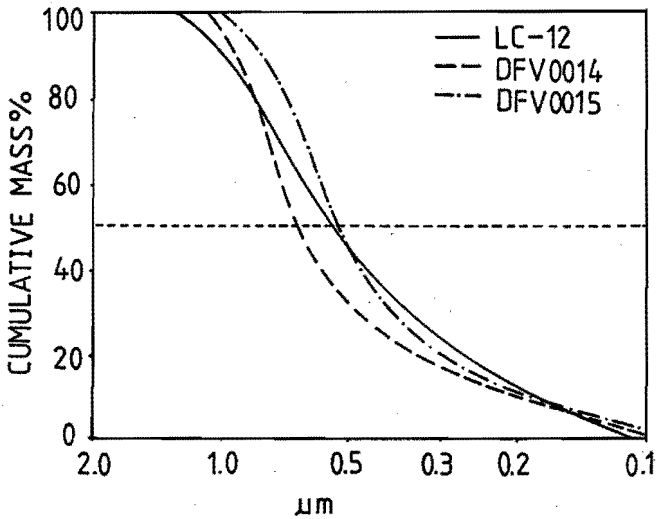


Fig. 3-1: Particle size distribution of silicon nitride powders. Data from suppliers.

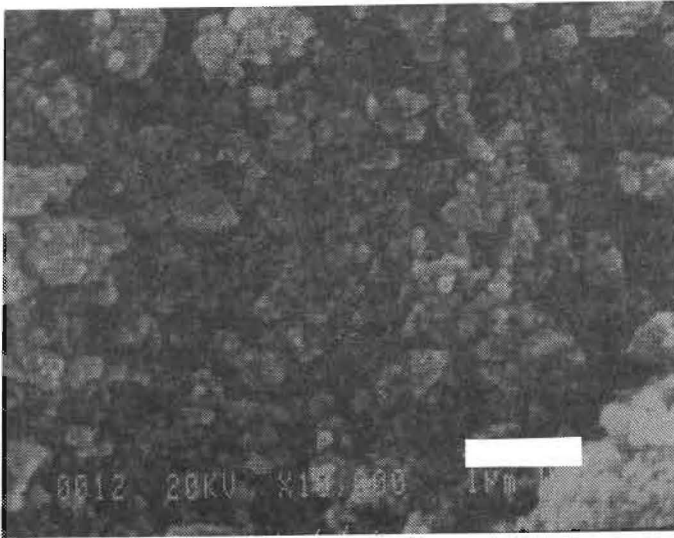


Fig. 3-2A: SEM micrograph of LC-12 silicon nitride powder. The bar is 2 μm .

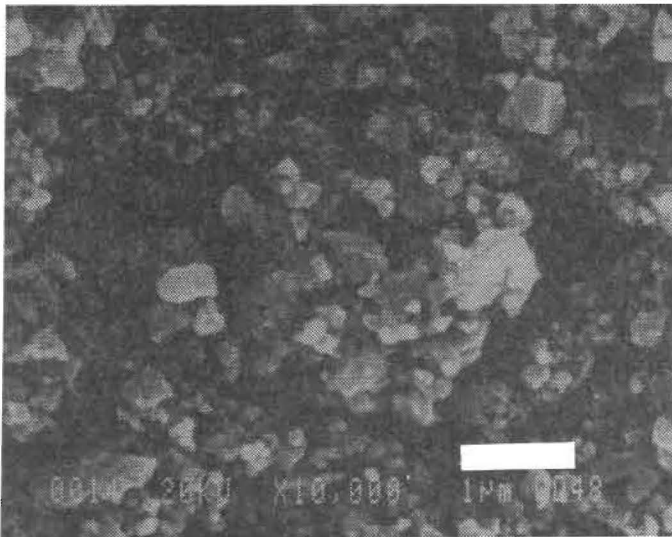


Fig. 3-2B: SEM micrograph of DFV0014 silicon nitride powder. The bar is 2 μm .

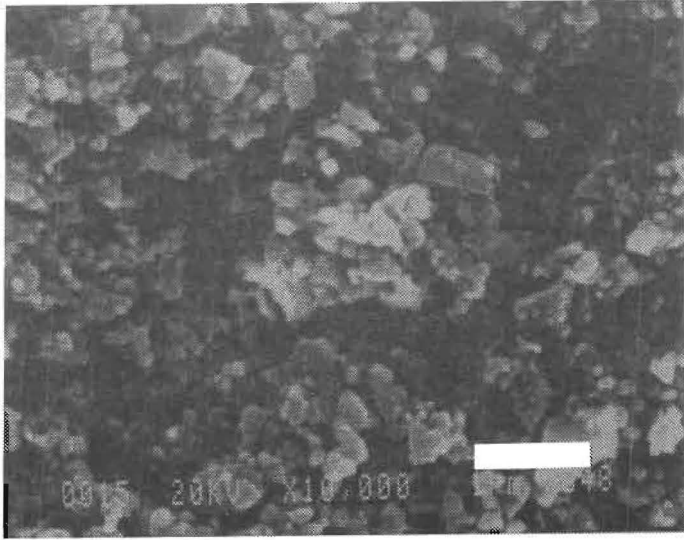


Fig. 3-2C: SEM micrograph of DFV0015 silicon nitride powder. The bar is 2 μm .

3-2. MIXTURE COMPOSITIONS

The composition of the starting mixtures was, in general, restricted to the concentration plane $\text{Si}_{12}\text{N}_{16}-\text{Al}_{12}\text{O}_{12}\text{N}_4-\text{Y}_4\text{Al}_8\text{N}_{12}$, such that the final compositions would be either monolithic α' -sialon or composite $\alpha'+\beta'$ -sialons according to the phase diagram [7-10] (see Fig. 2-13). The specimen compositions used are given in Table 3-3 and also plotted in Fig. 3-3.

The specimens can be classified into five groups:

A) Specimens A1 to A6 lie on the line $\text{Si}_3\text{N}_4-\text{Y}_2\text{O}_3:9\text{AlN}$, i.e. the ratio of Y_2O_3 to AlN kept constant, while the $\text{Y}_2\text{O}_3:9\text{AlN}$ content gradually decreases as the specimen number increases.

B) Specimens A2, A7 and A8 have the same composition parameter $X=0.5$, where X is from the formula $\text{Y}_X(\text{Si,Al})_{12}(\text{O,N})_{16}$, i.e. the same yttrium content per unit cell, while the oxygen and aluminium content increases with the increasing specimen number through the addition of Al_2O_3 powder to the mixtures. Since their final composition would be monolithic α' -sialon ceramics, this series will give information on the influence of various oxide contents as sintering additive on the

Table 3-3: Specimen compositions* (wt%)

No.	X*	Y*	Si ₃ N ₄	AlN	Al ₂ O ₃	Y ₂ O ₃	D*
A1	0.65	0.98	68.71	19.41	0	11.88	0.65
A2	0.50	0.75	75.41	15.25	0	9.34	0.65
A3	0.35	0.53	82.41	10.91	0	6.68	0.64
A4	0.25	0.37	87.37	7.83	0	4.80	0.64
A5	0.17	0.25	91.47	5.29	0	3.24	0.63
A6	0.08	0.12	95.68	2.68	0	1.64	0.63
A7	0.50	1.00	73.45	15.28	1.41	9.33	0.63
A8	0.50	1.20	72.08	16.03	2.53	9.36	0.63
A9	0.25	0.80	83.88	8.83	2.50	4.79	0.62
A10	0.25	1.20	80.62	9.76	4.83	4.79	0.62
B2	A2 with Bayer DFV0014						0.57
C2	A2 with Bayer DFV0015						0.56
L2	A2 + 5 wt% La ₂ O ₃						0.66

*: All samples specified as "A" series consist of LC-12 silicon nitride powder.

*: Here X and Y are independent composition parameters from the general formula: $Y_x Si_{12-(3x+y)} Al_{3x+y} O_y N_{16-y}$.

*: Relative density of the green compacts.

formation and densification of α' -sialon ceramics, although alumina will be incorporated into the lattice of the final products.

C) Specimens A4, A9 and A10 will yield composite $\alpha' + \beta'$ -sialon ceramics and show the differences of the formation, densification, microstructure and properties as a function of oxide content in the mixtures.

D) For specimens A2, B2 and C2, the composition of the mixtures are the same, but different types of silicon nitride powders are used as starting powders.

E) Specimen L2 is derived from the specimen A2 with an extra addition of 5 wt% of La₂O₃ powder. La₂O₃ does not enter the α' -sialon lattice due to the large size of La³⁺ [11].

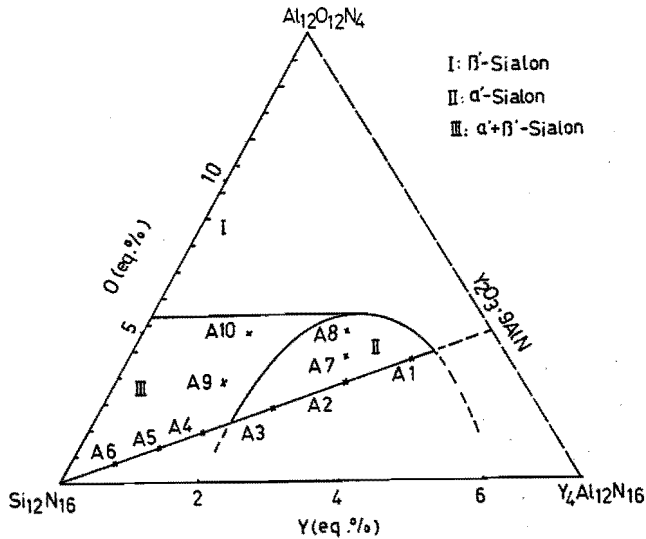


Fig. 3-3: Specimen composition spots in the phase diagram of the Y-Si-Al-O-N system.

3.3. POWDER PROCESSING

All mixtures were mixed and milled by normal ball milling for 50 hr. The milling balls (12 mm in diameter) are made of hot-pressed silicon nitride, a plastic bottle is used as the milling vessel, and the milling liquid is ethylalcohol, which is better to disperse powders compared to hexane. During such a milling process, the oxygen content in the silicon nitride powders is expected to increase. Hot extract chemical analysis was used to measure the increase of oxygen content as shown in Fig. 3-4. These analyses show that the difference in oxygen content between the three silicon nitride powders becomes smaller. The oxygen content increases above 0.2 wt%, and no significant influence of the original oxygen content has been observed.

After the milling step, dried powders were pressed uniaxially (approximately 1 MPa) and then isostatically under 250 MPa. The green density was about 63% theoretical density in the case of using LC-12 powder, while samples B2 and C2 have reached only 57% and 56% theoretical density, respectively (see Table 3-3).

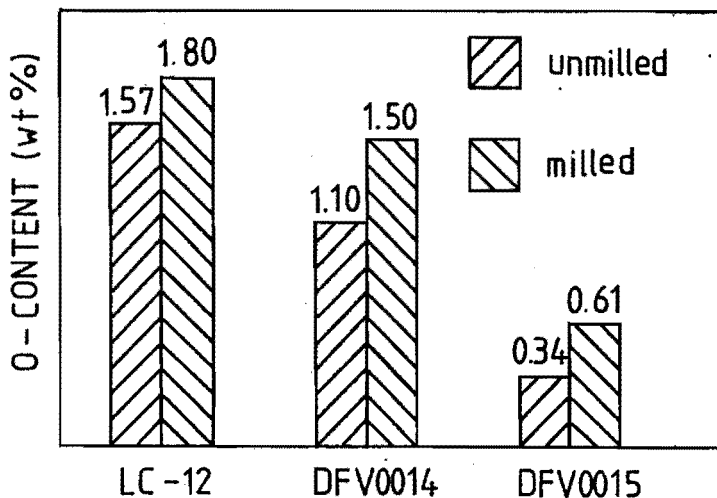


Fig. 3-4: Oxygen content in silicon nitride powders observed before and after powder processing.

3-4. SINTERING PROCESSING

Sintering was conducted in a gas pressure furnace capable of 2200°C under a nitrogen pressure up to 10 MPa equipped with a dilatometer. Three types of sintering powder beds are used: BN, AlN powder and a mixture composed of 70 wt% Si₃N₄, 25 wt% AlN and 5 wt% Y₂O₃. Both graphite and BN crucibles were used in this investigation.

The heating cycle can be generally described as follows: the specimens were heated up to 900°C in vacuum and then to 1200°C in 0.1 MPa N₂, at which the sintering was held 15 min to get a homogeneous temperature distribution. This procedure was followed in all sintering experiments. Various other sintering programs were used in the next step. In general, a heating rate of 10°C/min was used unless specified otherwise.

More details will be specified in following chapters.

have we set in det?

3-5. CHARACTERIZATION

The theoretical densities are estimated from the constituent densities as follows:

$$1/\rho = \sum n_i/\rho_i$$

where n_i is the weight fraction of each constituent and ρ_i is the constituent theoretical density.

Density measurements were carried out by using a water displacement balance. A mercury porosimeter was used as well.

The phase compositions were analysed mainly by using XRD. The fraction of α' - or β' -sialon was estimated by using the intensities of the 101 and combined 210 and 120 diffraction peaks for the β' -phase and those of the 102 and 210 peaks for the α' -phase. We assume that the relation:

$$\beta'/\alpha' = [I_{\beta(101)} + I_{\beta(210)}] / [I_{\alpha(102)} + I_{\alpha(210)}]$$

which is applicable to the case of pure β - and α -silicon nitride, is still valid [12,13].

The microstructure studies were carried out in TEM, SEM and optical microscopes using standard techniques. The composition and crystallinity of the grain boundary phases were determined by using energy dispersive spectrometer (EDS) and select area electron diffraction technique. The neutron diffraction analyses were conducted in the Netherland Energy Foundation (ECN, Petten).

Oxidation resistance experiments were conducted routinely by using a NETZSCH simultaneous thermal analyzer (STA 409). A heating rate of 10°C/min was used for all the experiments and an atmosphere of nitrogen was used in prior to the desired temperatures. A flow rate of 100 ccm/min was selected for all experiments.

The flexural strength at room temperature was determined by "ball-on-ring" testing. In this method, a plate specimen with 20 mm diameter and 1 mm in thickness is supported on a ring and loaded centrally with a ball [14-17]. Fig. 3-5 gives a schematic drawing of the "ball-on-ring" test. This method has the significant advantage that there is minimum friction between the specimen and the jig during loading. Details were given by Kokmeijer [20].

The Vickers hardness was determined routinely with a load of 0.5 N. The fracture toughness was calculated from the equation [18,19]:

$$K_{IC} = 0.016(E/H)^{1/2}P/c^{3/2}$$

where E is Young's modulus which was taken from the literature [21], H is the hardness, P is the Vickers load and c is the radial crack length. The Vickers load for fracture toughness measurement was 15 N.

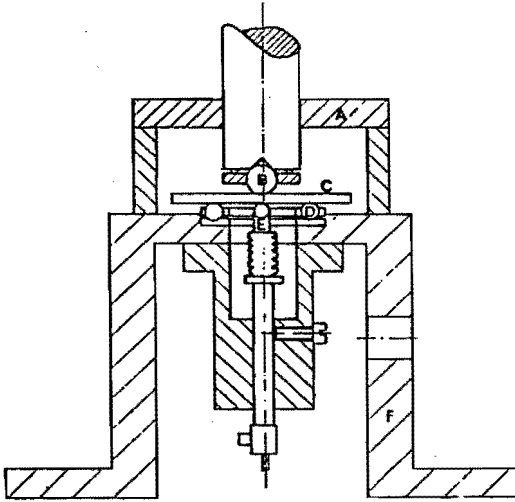


Fig. 3-5: Schematic drawing of the "ball-on-ring" test [14].
 A: centering device, D: support balls,
 B: loading ball, E: deflection sensor,
 C: specimens, F: base plate.

3-6. REFERENCES

1. Raider, S.I., Flitsch, R., Aboof, J.A. and Plisken, W.A.,
 J. Electrochem. Soc., 1976,123,560.
2. Peuckert, M. and Greil, P., J. Mater. Sci., 1987,22,3717.
3. Rahama, M.N., Boiteux, Y. and DeJonghe, L.C.,
 Am. Ceram. Soc. Bull., 1986,65,1171.
4. Jenett, H., Bubert, H. and Grallath, E.,
 Presenius Z. Anal. Chem., 1989,333,502.
5. Slack, G.A., J.Phys. Chem. Solids, 1973,34,321
6. Sakai, T. and Iwata, M., J. Mater. Sci., 1977,12,1659.

7. Huang, Z.K., Greil, P. and Petzow, G.,
J. Am. Ceram. Soc., 1983,66,C-96.
8. Stutz, D., Greil, P. and Petzow, G., J. Mater. Sci. Lett., 1986,5,335.
9. Slasor, S. and Thompson, D.P., Non-oxide Technical and Engineering Ceramics, ed. Hampshire, S., 1986, p223, Elsevier Applied Sciences.
10. Slasor, S. and Thompson, D.P., J. Mater. Sci. Lett., 1987,6,315.
11. Jack, K.H., Progress in Nitrogen Ceramics, ed. Riley, F.L., 1983, p45, NATO ASI Series E65, Martinus Nijhoff, The Hague.
12. Grand, G., Demit, J., Ruste, J. and Torre, J.P.,
J. Mater. Sci. Lett., 1979,14,1749.
13. Noakes, P.B. and Pratt, P.L., Special Ceramics 5, ed. Popper, P., 1972, p300, B.C.R.A., Stoke-on-Trent.
14. de With, G. and Wagemans, H.H.M., J. Am. Ceram. Soc., 1989,72,1538.
15. Shetty, D.K., Rosenfield, A.R., McGuire, P., Bansal, G.K. and Duckworth, W.H., Am. Ceram. Soc. Bull., 1980,59,1193.
16. McKinney, K.R. and Herbert, C., J. Am. Ceram., 1970,53,513.
17. Marshall, D.B., Am. Ceram. Soc. Bull., 1980,59,551.
18. Antis, G.R., Chantikul, P., Lawn, B.R. and Marshall, D.B.,
J. Am. Ceram. Soc., 1981,64,533.
19. Lemaitre, P. and Piller, R., J. Mater. Sci. Lett., 1988,7,772.
20. Kokmeijer, E., Ph.D Thesis, Eindhoven University of Technology, the Netherlands, 1990.
21. Stutz, D., Ph.D Thesis, Stuttgart University, FRG, 1986.

CHAPTER FOUR. FORMATION AND DENSIFICATION OF α' -SIALON CERAMICS

4-1. INTRODUCTION

This chapter describes the study of formation and densification in α' -sialon ceramics as well as the microstructural development during the heating cycle.

For the study of formation of α' -sialon the reaction sequences were determined. The specimens of various mixtures, described in the previous chapter, were placed in a BN crucible embedded with the mixture bed powder and heated at a heating rate of 10°C/min in the gas pressure furnace up to the temperatures desired under a nitrogen pressure of 0.5 MPa, and then cooled down immediately, with a cooling rate 200 °C/min at temperatures above 1200 °C. After sintering the specimens were ground to remove the surface layer and analysed by XRD to determine the composition. The results of the crystalline phases were presented graphically. Although the analyses were done carefully, only approximate data (accuracy is about 5%) were obtained. Hence the data points for minor phases were omitted in the figures and the data are used only in a qualitative way. The density, weight loss, and linear shrinkage of the heat treated specimens were measured, too. The specimens were also used to follow the microstructural development by using SEM.

The densification behaviour was followed by using in-situ dilatometry. The specimens (of 5x4x15 mm) were embedded in BN powder and heated under a nitrogen pressure of 0.5 MPa with a heating rate of 10°C/min. Some other values for the heating rate were used in a number of cases to observe the influence of the heating rate. Since in the dilatometry experiments the samples cannot be covered with the powder bed, the weight loss is relatively high in this case, viz. 4 wt%. No variation of the bulk composition was observed. The specimens from the dilatometry experiments were not used for any further experiments.

It is also noted here that the reaction sequence and shrinkage behaviour of sample A6 are not included, since it does not sinter.

4.2. FORMATION OF SIALONS

A. Formation of α' -sialon

Fig. 4-1 and Fig. 4-2 show the reaction sequences for the formation of α' -sialon during the heating cycle in samples A1 and A2, respectively. The powder mixtures of both samples consisted of silicon nitride, aluminium nitride and yttria (see Table 3-3). The α -silicon nitride content in both samples is less than 80%, lower than that in the silicon nitride starting powder (see Table 3-1). The content of nitrides remains unchanged up till 1360°C, although the yttria content slightly declines as the temperature rises above 1300°C. At about 1360°C silicon nitride starts to react and the formation of α' -sialon as well as melilite $\text{Si}_3\text{N}_4\cdot\text{Y}_2\text{O}_3$ begins. The content of the α' -sialon and melilite phases increases and that of silicon nitride decreases rapidly with rising temperature. The amount of melilite increases to a maximum approximately at 1500°C and then decreases at higher temperatures, vanishing around 1600°C. It is seen that the decrease of melilite is accompanied by a slow decrease of silicon nitride, the latter is accelerated again only after all melilite disappeared. Although Y_2O_3 disappears at a temperature below 1500°C, and nitrides become undetectable at temperatures below 1750°C, the increase of α' -sialon continues approximately until 1800°C.

In spite of the difference in starting compositions of mixtures A1 and A2, the reaction sequences are quite similar and also the reaction temperatures are the same. The ratio of α to β -silicon nitride also does not influence the formation of α' -sialon. Melilite is the only intermediate compound during the heating cycles, it appears simultaneously with the α' -sialon.

Due to the high energy needed to break the Si-N bond and the low diffusivity of silicon and nitrogen in the solid state [1-5], the decrease of silicon nitride and the formation of α' -sialon phase is proposed to occur via a liquid phase. Therefore our results imply the existence of a liquid phase at 1360°C. As the temperature increases above 1300°C, yttria reacts with the oxygen rich surface layer of the nitride particles [6-10] (see the previous chapter) and impurities to form an oxide eutectic liquid phase [11-12]. This allows the dissolution of silicon nitride and the precipitation of α' -sialon at higher temperatures starting approximately at 1360°C according to the present experiments.

Once the dissolution of nitrides and precipitation of α' -sialon start the

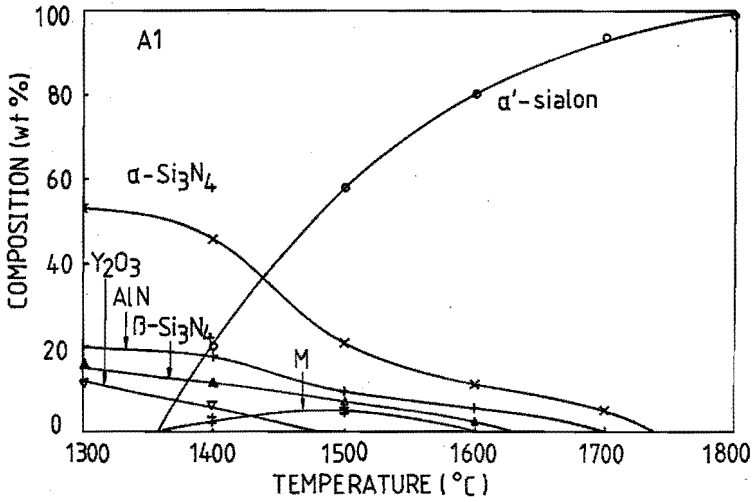


Fig. 4-1: Reaction sequence of the formation of α' -sialon in sample A1, heating rate $10^\circ\text{C}/\text{min}$. M = melilite.

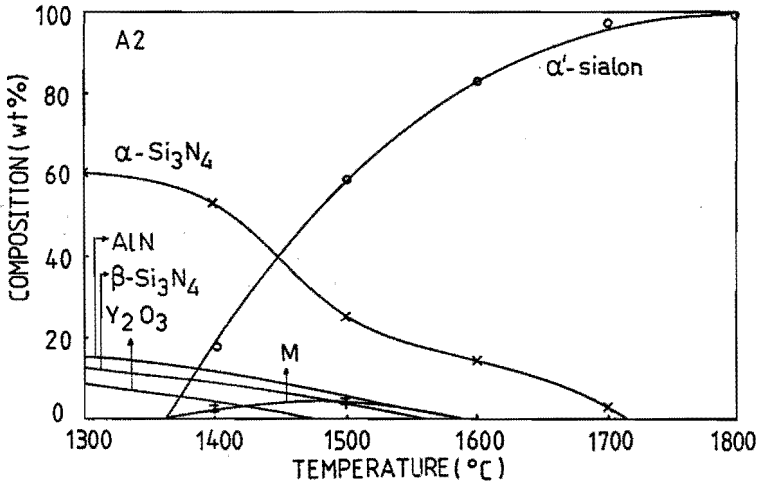


Fig. 4-2: Reaction sequence of the formation of α' -sialon in sample A2, heating rate $10^\circ\text{C}/\text{min}$. M = melilite.

reaction proceeds very quickly. Approximately 20 wt% α' -phase is formed at 1400°C and 60 wt% at 1500°C. The precipitation of melilite starts almost concurrently with that of α' -sialon and accelerates the dissolution of silicon nitride by consuming a lot of silicon nitride from the liquid. However, melilite dissolves again in the liquid at temperatures higher than 1500°C and we have seen that this suppresses the dissolution of silicon nitride.

B. Formation of α' + β' -sialon

The reaction sequences for the formation in composite α' + β' -sialon ceramics are indicated in Fig. 4-3, Fig. 4-4 and Fig. 4-5, for samples A3, A4 and A5, respectively. The decrease of silicon nitride and the formation of α' -sialon occurred approximately at 1360°C just as in Figs. 4-1 and 4-2, while the formation of melilite was only observed in samples A3 and A4, but not in A5. As the temperature increased further to approximately 1460°C the formation of β' -sialon started, and at 1500°C about 10 wt% β' -phase was formed in samples A3 and A4 and 20 wt% in A5. Also it was seen that melilite and the starting materials except α -silicon nitride became undetectable by using XRD at a temperature slightly below 1600°C, while the content of sialons increased further with temperatures rising to approximately 1800°C.

The ratio of Y_2O_3 to AlN remained unchanged in samples A1 to A5, while the amount of silicon nitride increased significantly from A1 to A5 (see Table 3-3). As a result the final product changed from monolithic α' -sialon, as in A1 and A2, to composite α' + β' -sialons in A3 to A5. In spite of these changes the dissolution of silicon nitride and the formation of α' -sialon were found to start approximately at the same temperature of 1360°C. It is seen that the dissolution of silicon nitride and the precipitation of sialons are closely correlated, although the different amount of yttria in the starting mixtures resulted in a different composition and quantity of the oxide liquid phase.

It was also seen that the precipitation of β' -sialon started at 1460°C, about 100°C higher than that of the α' -phase.

As described in the beginning of this chapter the reaction sequences for the formation of sialons only include the crystalline phases, while the amorphous phase is not included. At temperatures higher than 1750°C, though almost all raw

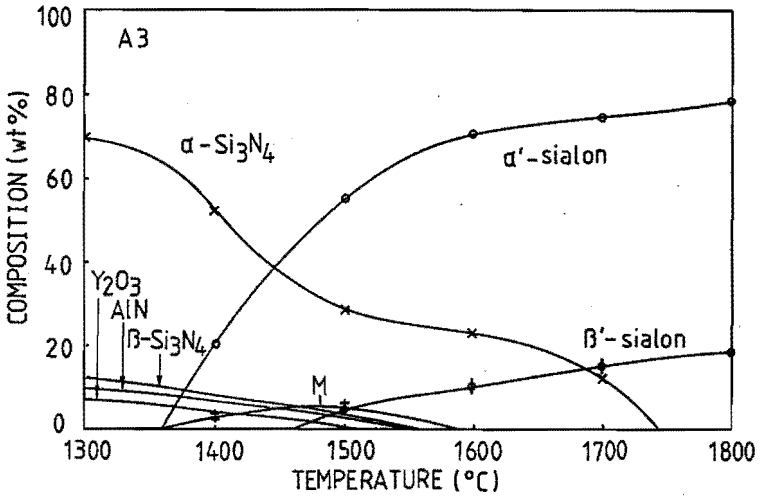


Fig. 4-3: Reaction sequence of the formation of α' -sialon in sample A3, heating rate $10^{\circ}\text{C}/\text{min}$. M = melilite.

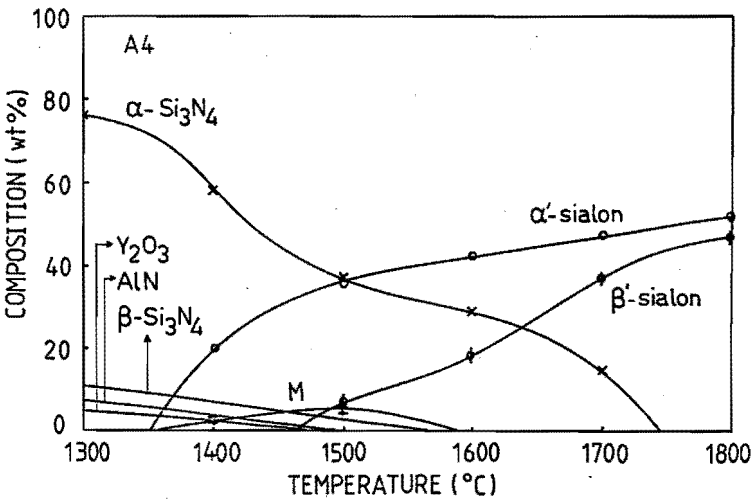


Fig. 4-4: Reaction sequence of the formation of α' -sialon in sample A4, heating rate $10^{\circ}\text{C}/\text{min}$. M = melilite.

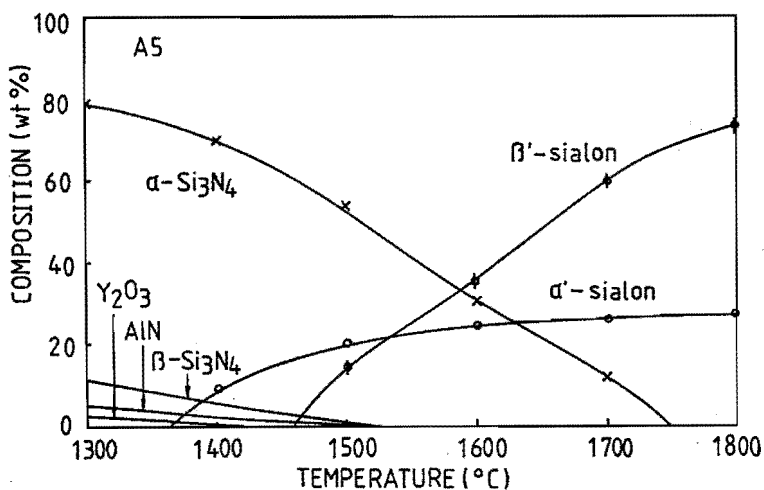


Fig. 4-5: Reaction sequence of the formation of α' -sialon in sample A5, heating rate $10^\circ\text{C}/\text{min}$.

materials dissolved into the liquid, the precipitation of sialons went on by consuming the liquid phase.

It also should be noted that the final product of sample A3 should yield monolithic α' -sialon according to the phase diagrams [13-16]. However, the experimental results presented in Fig. 3-3 indicate that almost 20 wt% β' -sialon was formed, which implies that only a part of the yttria was consumed to form α' -phase, while other part remained in the liquid phase, which cools to glass. Besides, a composition of mixed α' -sialon and β -silicon nitride was expected in the case of samples A4 and A5 (see Figs. 2-13 and 3-4) [13-16]. The discrepancies observed here will be discussed in detail later in chapter six.

C. Addition of Al_2O_3

The reaction sequences for the formation of α' -sialon in alumina containing mixtures (samples A7 and A8) (see Table 3-3) are shown in Figs. 4-6 and 4-7, respectively. YAG, $3\text{Y}_2\text{O}_3 \cdot 5\text{Al}_2\text{O}_3$, was found at a temperature as low as 1300°C , which was the lowest temperature used for the experiments described here. With

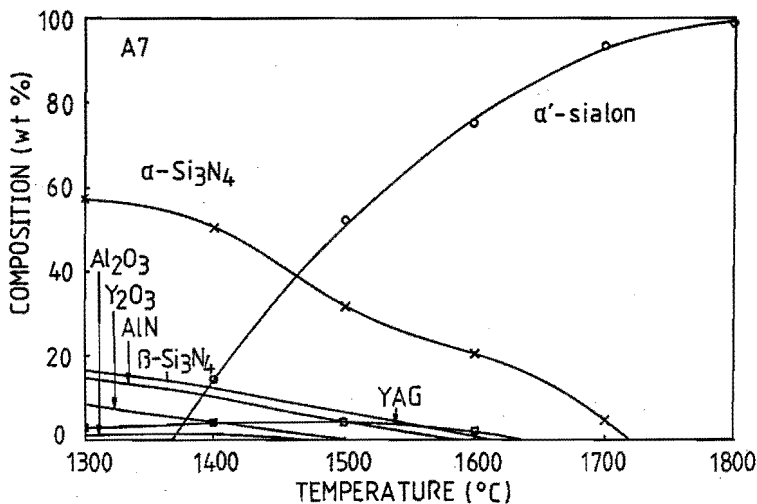


Fig. 4-6: Reaction sequence of the formation of α' -sialon in sample A7, heating rate $10^\circ\text{C}/\text{min}$. $\text{YAG} = 3\text{Y}_2\text{O}_3 \cdot 5\text{Al}_2\text{O}_3$.

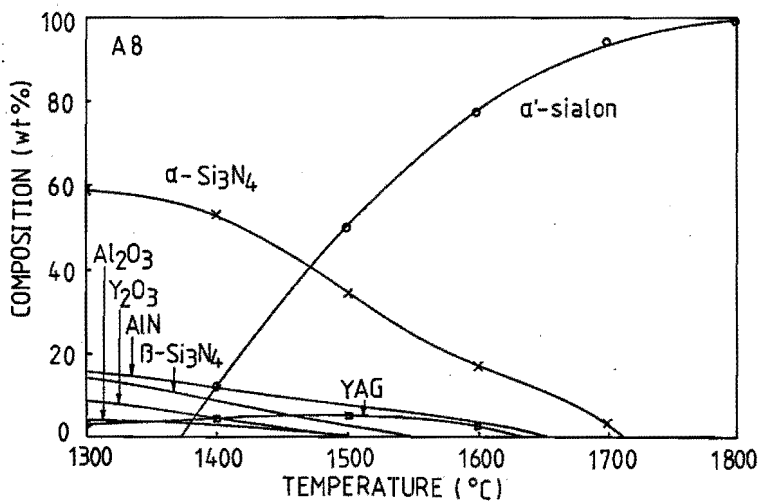


Fig. 4-7: Reaction sequence of the formation of α' -sialon in sample A8, heating rate $10^\circ\text{C}/\text{min}$. $\text{YAG} = 3\text{Y}_2\text{O}_3 \cdot 5\text{Al}_2\text{O}_3$.

rising temperature the content of YAG increased slightly till 1550°C and then gradually decreased at higher temperatures, disappearing below 1650°C. The decrease of silicon nitride and the formation of α' -sialon occurred approximately at 1360°C just as in samples A1 to A5. A significant difference was observed, i.e. no intermediate compound melilite was found, instead YAG was formed.

The effects on the α' + β' -sialon formation of the addition of Al_2O_3 (samples A9 and A10) are given in Figs. 4-8 and 4-9, respectively. The formation of α' -sialon started at 1360°C just as discussed previously. The content of the α' -phase increased very rapidly with rising temperature and became approximately constant at 1500°C. The precipitation of β' -sialon occurred at a slightly higher temperature of 1480°C compared with that in Figs. 4-3 to 4-5. As the temperature was rising further the β' -phase increased, while the content of α' -phase decreased slightly and increased a little at temperatures above 1650°C, after YAG vanished.

The content of YAG is relatively high, but this phase disappeared at a lower temperature of 1600°C, compared with that in Figs. 4-6 and 4-7.

Although Al_2O_3 is expected to be incorporated into the sialon structures, it reacts with Y_2O_3 to form YAG, starting at 810°C [17] which is much lower than the eutectic temperature. Thus when the eutectic liquid phase appeared around 1300°C, much of the Y_2O_3 was trapped in YAG and the yttrium content in the liquid was low. Consequently no Y-N-melilite was formed or the amount formed was so small that its presence could not be observed.

YAG starts to dissolve into the liquid above 1500°C. At a temperature below 1600°C all YAG dissolved in the case of samples A7 and A8. However, in the case of composite α' + β' -sialon ceramics (see Figs. 4-8 and 4-9), the decrease of YAG was accompanied by the decrease of the α' -phase with rising temperature, and the content of the α' -phase increased once again only at temperatures above 1650°C after all YAG dissolved into the liquid. The dissolution of YAG into the liquid increased the content of oxygen, aluminium and yttrium in the liquid. Thus α' -sialon, formed previously, is proposed to react with this oxygen rich liquid phase either to incorporate more oxygen, aluminium and yttrium into the lattice, and/or to form β' -sialon via the reaction of α' -sialon with oxides [18-21].

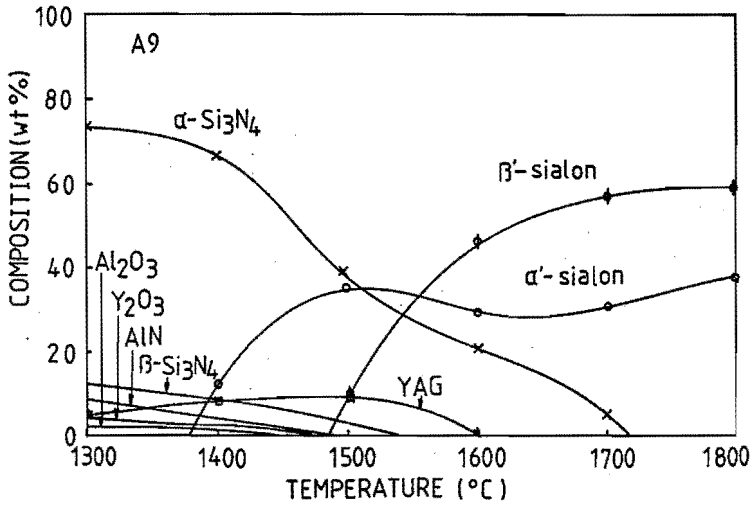


Fig. 4-8: Reaction sequence of the formation of α' -sialon in sample A9, heating rate $10^{\circ}\text{C}/\text{min}$. $\text{YAG} = 3\text{Y}_2\text{O}_3 \cdot 5\text{Al}_2\text{O}_3$.

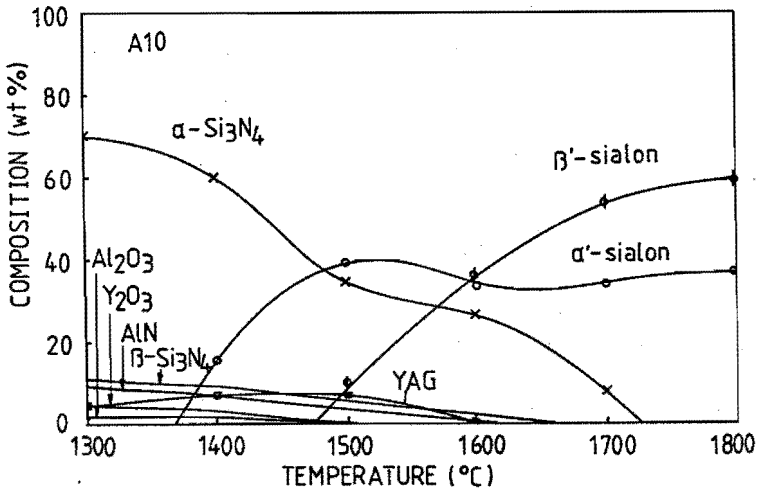


Fig. 4-9: Reaction sequence of the formation of α' -sialon in sample A10, heating rate $10^{\circ}\text{C}/\text{min}$. $\text{YAG} = 3\text{Y}_2\text{O}_3 \cdot 5\text{Al}_2\text{O}_3$.

D. Addition of La₂O₃

Fig. 4-10 shows the reaction sequence of the formation of α' -sialon in the case of the addition of La₂O₃ to the starting mixtures (see Table 3-3). The dissolution of silicon nitride into and the precipitation of α' -sialon from the liquid was approximately the same compared with that in samples A2 (see Fig. 4-2) and A8 (see Fig. 4-7). The precipitation of (Y,La)-melilite solid solutions [22], instead of Y-melilite, occurred. It started simultaneously with that of α' -phase approximately at 1370°C and dissolved into the liquid at 1620°C. Also the amount of this (Y,La)-melilite solid solution was much larger than of Y-melilite observed in sample A2.

The addition of La₂O₃ is expected to lower the eutectic temperature and also increase the quantity and the oxygen content of the liquid phase, although some was consumed to react with yttria and silicon nitride to form (Y,La)-melilite. It also should be noted that La₂O₃ is expected not to be incorporated into the α' -sialon lattice due to the large size of La³⁺ [18], and thus differs in this respect from alumina. Consequently this should result in the formation of two different intermediate compounds. However, no significant difference in the formation of α' -sialon in sample L2 has been observed compared with that in samples A2 and A8.

E. Effects of the characteristics of the silicon nitride starting powders

Samples A2, B2 and C2 possessed the "same" mixture composition but contained different types of silicon nitride powders as described in the previous chapter. The reaction sequences of the formation of α' -sialon in the three samples were the same as indicated in Fig. 4-2.

The amount of oxygen impurity in the silicon nitride starting powders increases from 0.61 wt% in sample C2, to 1.50 wt% in B2, and to 1.80 wt% in A2. Since the oxygen impurity is assumed to be present mainly as silica, the increasing oxygen content in silicon nitride powders thus results in an increased amount of oxides and shifts the oxide composition towards the silica rich side (see Fig. 4-11). Therefore, an increase in the amount and a decrease in the viscosity of the liquid phase is expected, possibly resulting in fast atom diffusion through this liquid phase.

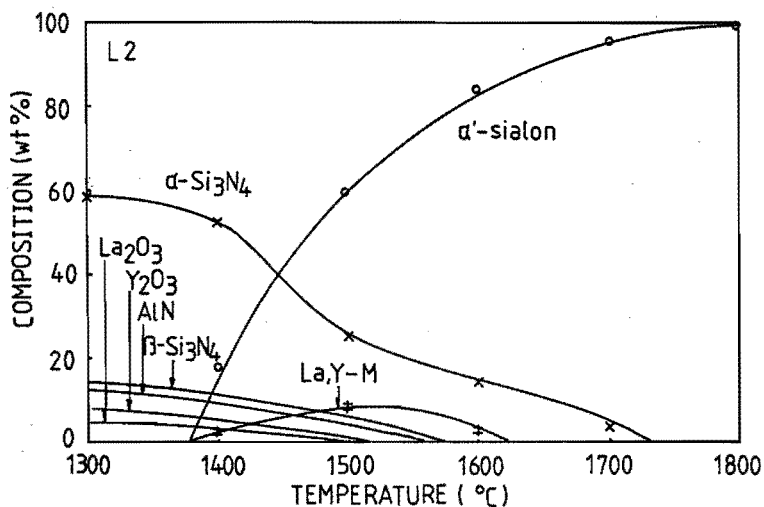


Fig. 4-10: Reaction sequence of the formation of α' -sialon in sample L2, heating rate $10^\circ\text{C}/\text{min}$. La,Y-M = (La,Y)-melilite.

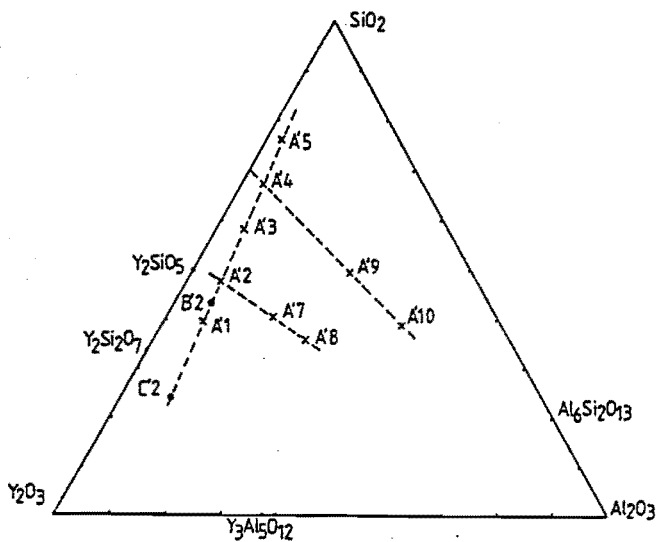


Fig. 4-11: Composition of the oxides present in the starting mixtures. A'1 is for sample A1.

Also the difference of the α/β -silicon nitride ratio in the starting silicon nitride powders used for the three samples was considerable, and there were some differences in other impurities, too. The similar reaction sequences observed for the three specimens imply a very minor or no influence of these impurities and α -phase content on the formation of α' -sialons.

F. Isothermal formation of sialons

The study of isothermal formation of sialons at various temperatures was conducted as well. The experimental results indicate that the formation of both α' - and β' -sialon were complete at a temperature as low as 1600°C, although it took almost 1 hr. However, no further data analysis was conducted here due to the inaccuracy of the data obtained as stated previously.

4.3. DENSIFICATION OF α' -SIALON CERAMICS

A. Densification behaviour

Fig. 4-12 and Fig. 4-13 show the densification behaviour of α' -sialon and composite $\alpha'+\beta'$ -sialon ceramics in samples A2 and A4, respectively. Two peaks in the shrinkage rate versus temperature plot are visible.

For sample A2, the shrinkage started approximately at 1360°C and accelerated with rising temperature. The shrinkage rate reaches the first maximum peak approximately at 1500°C and then decreases as the temperature rises further to 1600°C. The shrinkage rate then speeds up once again and reached the second shrinkage rate peak approximately at 1660°C. Above this temperature the shrinkage proceeds further with a continuous decrease of the shrinkage rate. Regarding to the reaction sequences in sample A2 (see Fig. 4-2), the shrinkage started approximately at 1360°C, at which the decrease of silicon nitride and the formation of α' -sialon occurred concurrently. The oxide eutectic liquid phase appears already slightly below this temperature. As discussed before, the formation of this liquid phase did not result in the occurrence of a shrinkage. The dissolution of nitrides into and precipitation of α' -sialon and melilite from the liquid occurred at about 1360°C and subsequently led to the start of the shrinkage. Also it is seen that the acceleration of the shrinkage speed corresponds well to the rapid dissolution of silicon nitride into the liquid. The increase of the shrinkage

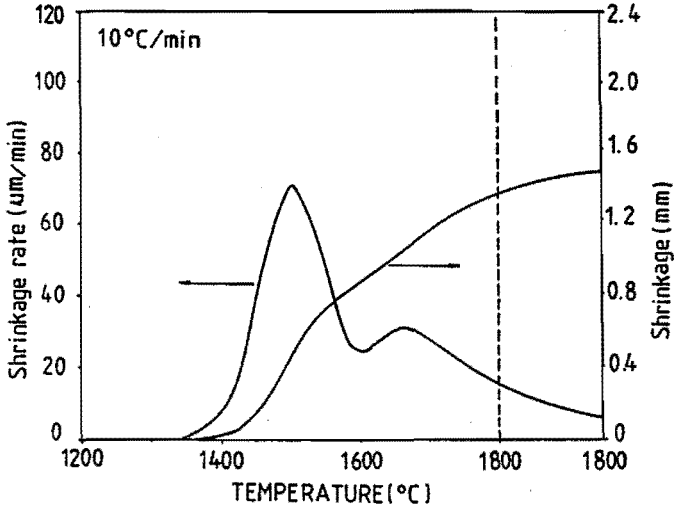


Fig. 4-12: Shrinkage and shrinkage rate curves in the sintering of α' -sialon sample A2.

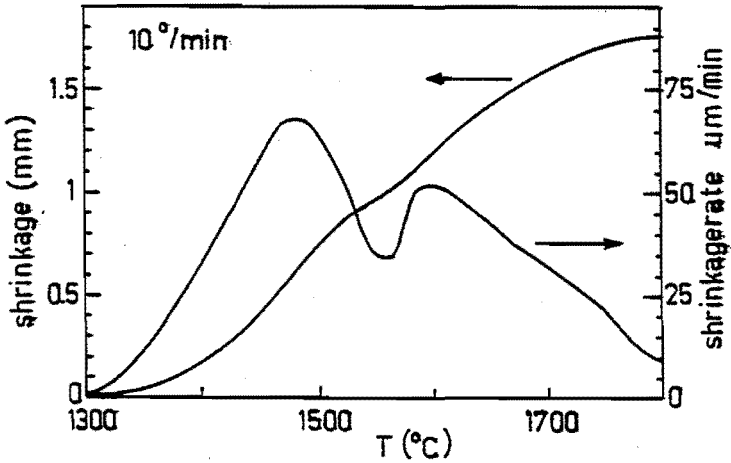


Fig. 4-13: Shrinkage and shrinkage rate curves in the sintering of mixed α' + β' -sialon sample A4.

rate stopped and the melilite content reached a maximum at 1500°C. Then the dissolution of melilite into the liquid, suppressing the dissolution of silicon nitride, was seen to be accompanied by a decrease of the shrinkage rate. When melilite disappeared approximately at 1600°C and the dissolution of silicon nitride was accelerated again, the shrinkage rate reached a second maximum.

However, for sample A4, there are some differences. The shrinkage started at a temperature as low as 1300°C and reaches the first shrinkage rate maximum approximately at 1490°C. The shrinkage rate decreased with temperature rising up to 1570°C, and then increased again to the second peak at approximately 1600°C. Both shrinkage rate peaks appeared at lower temperatures as compared with those of sample A2. The shrinkage started approximately at 1300°C, at which the oxide eutectic liquid phase was formed, but the dissolution of silicon nitride and precipitation of sialon has not occurred with regard to the reaction sequences in A4. This implies the occurrence of primary rearrangement, although the composition of the starting mixture of A4 contained less yttria and more silicon nitride (see Table 3-3). The occurrence of the precipitation of β' -sialon at 1560°C is expected to speed up the dissolution of silicon nitride into the liquid and therefore accelerate the shrinkage rate at 1570°C, prior to the disappearance of melilite.

It is noted that the reaction sequence and the shrinkage behaviour were followed in different experiments with different methods as described in the beginning of this chapter. The reaction and sintering process do not stop immediately during cooling, thus some discrepancies are possible, especially a slight shift of temperatures. Fig. 4-14 shows the density values measured from the specimens used to determine the reaction sequences.

B. Addition of Al_2O_3

Fig. 4-15, as an example, gives the densification behaviour of sample A8. The difference compared to that of sample A2 in Fig. 4-13 is quite large. The densification process started at a temperature below 1250°C. For A8 the first shrinkage rate peak appeared at 1300°C and the second one approximately at 1500°C. Above this temperature the shrinkage rate declined continuously and no shrinkage rate peak was observed around 1600°C, which appeared in the case of

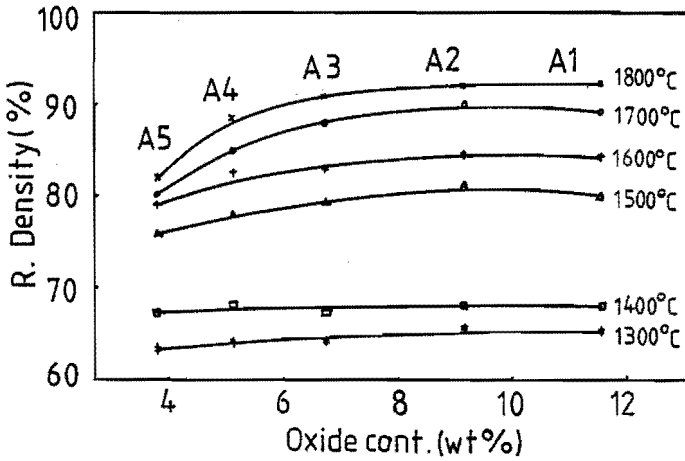


Fig. 4-14: Development of density values of α' - and $\alpha'+\beta'$ -sialon ceramics without alumina in the starting mixtures.

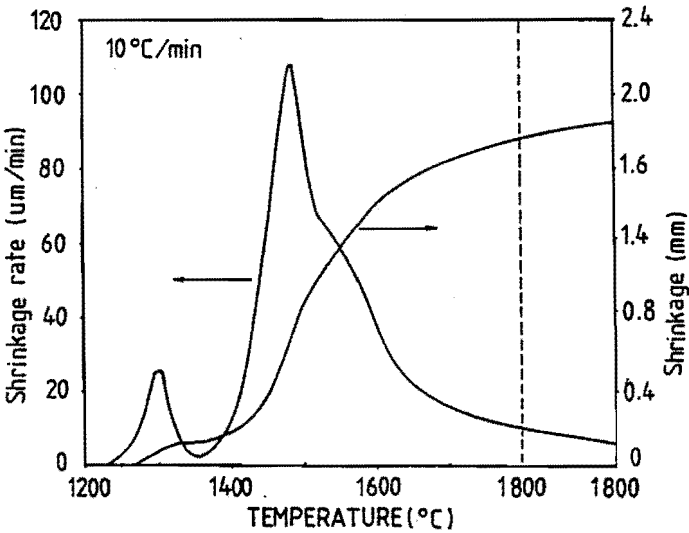


Fig. 4-15: Shrinkage and shrinkage rate curves in the sintering of α' -sialon sample A8 containing Al_2O_3 .

samples A2 and A4. The occurrence of the shrinkage rate peak at approximately 1240°C implies that the oxide eutectic liquid phase appeared at this temperature or lower than that, although there was a solid state reaction of the formation of YAG. The addition of Al₂O₃ powder to the mixture increased the amount of oxides and shifted the oxide composition closer to the eutectic composition (see Fig. 4-11), and subsequently increased the amount of the oxide liquid formed above the eutectic temperature. As a consequence, an extensive primary rearrangement occurred and led to the first shrinkage rate peak around 1300°C. The dissolution of silicon nitride and precipitation of α'-sialon started only when the temperature was above 1350°C, although there was a large amount of the oxide liquid phase. This dissolution-precipitation process resulted in the acceleration of the shrinkage process with rising temperature and reached a second maximum at 1500°C. Above 1500°C YAG dissolves into the liquid gradually, resulting in an increase of the amount of the liquid and a decrease of its viscosity, thus the densification progressed smoothly with rising temperature. The shrinkage rate, of 40 μm/min around 1600°C, was larger than the maximum value, of 30 μm/min, observed in Fig. 4-12, although no shrinkage rate peak was observed. This high shrinkage rate resulted in a quick densification. Approximately 90% of the theoretical density has been reached at about 1600°C, and then the densification proceeds slowly.

The densification behaviour in other samples made from alumina containing mixtures was approximately the same as that in sample A8, even though the dissolution of α'-sialons into the liquid occurred above 1500°C in samples A9 and A10. The similarity in densification behaviour implies two possibilities. One is that the dissolution of the α'-phase above 1500°C exhibits no or little influence on the densification process; another is that the same dissolution process occurred in the case of samples A7 and A8.

Fig. 4-16 shows the development of the density as a function of temperature for various samples with alumina. In general, the densities shown in this figure were higher than those calculated from the dilatometry data, which have been discussed before.

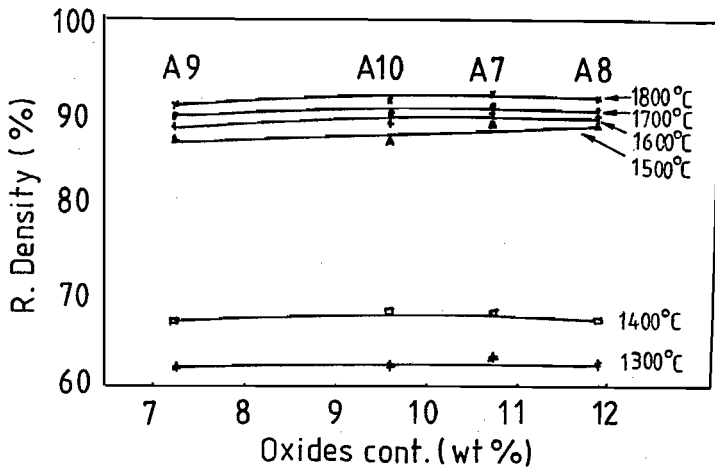


Fig. 4-16: Development of density values of α' - and $\alpha'+\beta'$ -sialon ceramics as a function of total $Y_2O_3 + Al_2O_3$ content.

C. Addition of La_2O_3

The influence of the addition of La_2O_3 on the densification of α' -sialon ceramics has been studied as well (see Fig. 4-17). A considerable difference compared with that in the case of samples A2 and A8 was observed. The densification started approximately at 1210°C and proceeded continuously to the maximum in the shrinkage rate around 1420°C. Then the shrinkage rate decreased rapidly with rising temperature and only about one third of the maximum shrinkage rate remained at 1550°C. Above this temperature the shrinkage rate slightly increased with temperature to approach the second peak in the shrinkage rate at 1610°C.

The addition of La_2O_3 powder to the starting mixture is expected to lower the eutectic temperature and to increase the amount of liquid during firing. The occurrence of the densification at 1210°C implies the existence of a liquid phase, since there was no solid state reaction observed, according to the XRD analyses (see Fig. 4-10). Extensive densification is proposed to start immediately after the formation of the oxide eutectic liquid phase probably due to the large quantity of

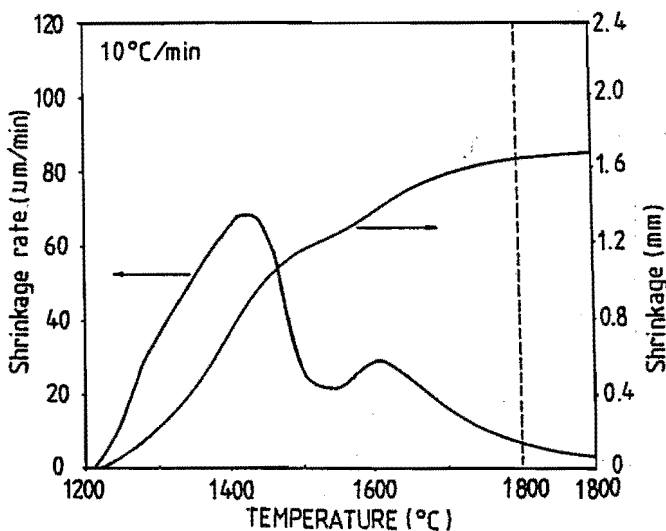


Fig. 4-17: Shrinkage and shrinkage rate curves for the sintering of α' -sialon sample L2 containing La_2O_3 .

the liquid phase. At a temperature of 1380°C the dissolution-precipitation process starts and also contributes to densification (see Fig. 4-10). Thus only one peak in the shrinkage rate is visible. A decrease of the shrinkage rate was observed above 1420°C , although the amount of (Y,La)-melilite solid solutions continued to increase with rising temperature. Also the increase of the shrinkage rate at temperatures above 1500°C did not correspond to the dissolution of this solid solution. This strongly suggests that the dissolution of the (Y,La)-melilite solid solution into the liquid plays an unimportant role for the densification, in contrast to that proposed previously to the case of A2 and A4.

D. Effects of the characteristics of the silicon nitride starting powders

Even though the characteristics of the silicon nitride starting powders have shown a minor influence on the formation of α' -sialon, the densification behaviour changes considerably with various silicon nitride powders used in the mixtures as can be seen from Figs. 4-18 and 4-19. These two figures also show the sintering behaviour of the three samples at higher sintering temperatures under a nitrogen

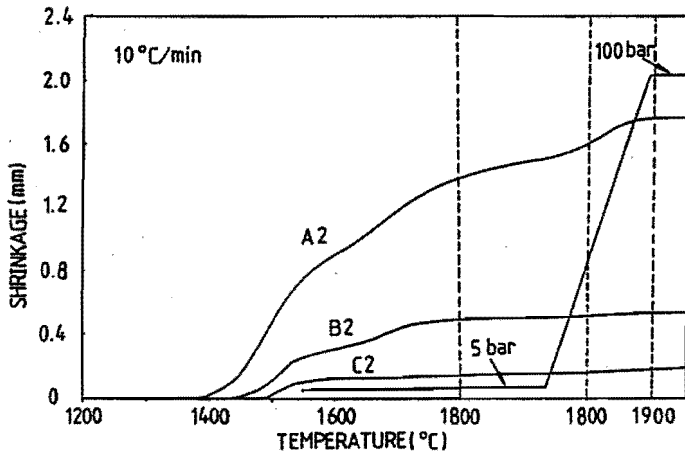


Fig. 4-18: Shrinkage curves for the sintering of the α' -sialon samples A2, B2 and C2.

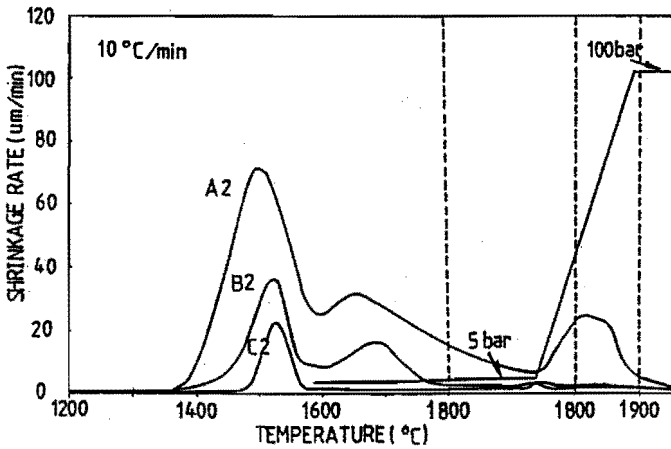


Fig. 4-19: Shrinkage rate curves for the sintering of the α' -sialon samples A2, B2 and C2.

Have you measured out other T-rates?

pressure of 10 MPa. This will be discussed later in chapter five.

The figures show that the shrinkage in the three samples starts approximately at the same temperature of 1360°C. The absolute shrinkage and the shrinkage rate decrease in the order A2 > B2 > C2. There is also a slight shift of the peaks towards higher temperatures. The second shrinkage peak was not observed in the case of C2. As the sintering temperature rised up to 1800°C, relative densities of only 75 % and 72 % were reached in samples B2 and C2, respectively.

Since the reaction sequence was the same in the three samples, the difference observed in the densification process implies again that the dissolution of melilite at higher temperatures exhibits a very minor or no influence on the densification of sialon ceramics. Instead the characteristics of the silicon nitride starting powders have a considerable influence on the sintering process. The mixtures based on the silicon nitride starting powders with a small amount of oxygen impurity and a low α -phase content of samples B2 and C2 exhibited a very poor sinterability.

E. Heating rate

The heating rate is another important process parameter for the densification of sialon ceramics. Fig. 4-20 and Fig. 4-21 show the densification behaviour for various heating rates. The shrinkage rate peaks shift to higher temperature when the heating rate increases. The two peaks overlapped for the highest heating rates. At 1800°C a relative density not less than 90% can be achieved even though a very high heating rate of 120°C/min is employed. Some macrocracks were observed in the specimens sintered by using the heating rate 120°C/min.

The higher heating rate is expected to prevent the formation of the solid skeleton. Furthermore the high heating rate allows the reduction of the liquid quantity [23], i.e. less sintering additives are needed to achieve full densification, since the liquid constituents are absorbed gradually during firing. The high heating rate also resulted in a temperature gradient in the specimens, and consequently led to a high overlap of the different sintering processes due to the delay of the densification of the bulk of the specimen. This inhomogeneous sintering leads to

stresses and microcracking.

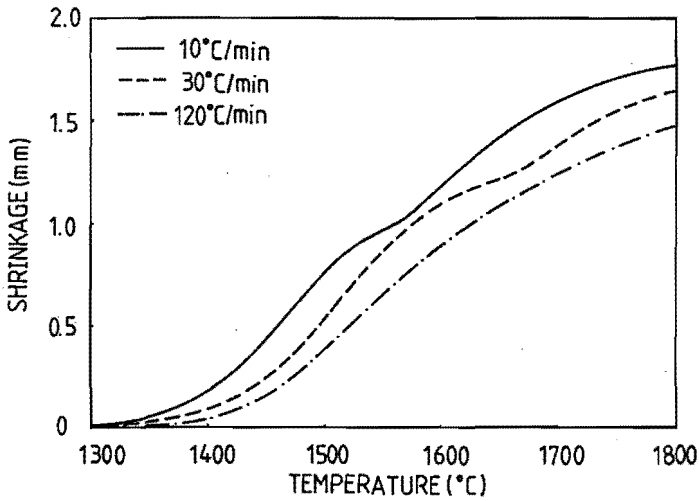


Fig. 4-20: Shrinkage curves for the sintering of α' -sialon ceramics with various heating rates.

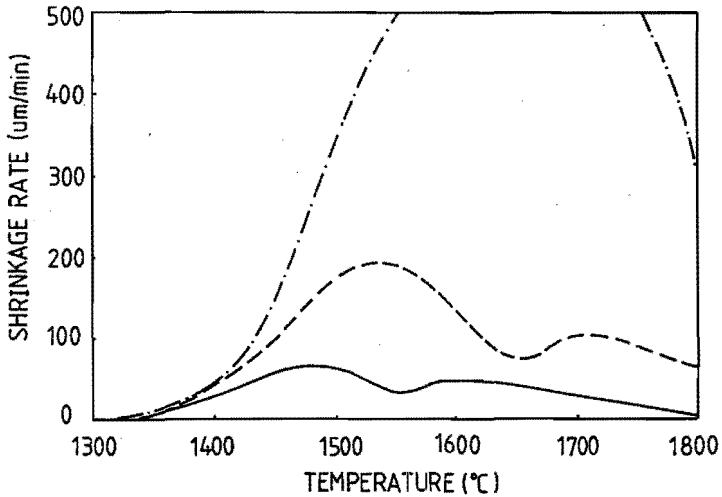


Fig. 4-21: Shrinkage rate curves for the sintering of α' -sialon ceramics with various heating rates as given in Fig. 4-20.

F. Isothermal sintering

Fig. 4-22 shows the isothermal sintering behaviour at 1600°C of α' -sialon ceramics with various starting compositions. It indicates that the densification followed the equation: $\Delta l/l_0 \propto t^n$, where l_0 is the original specimen length and Δl the linear shrinkage at time t . It is seen that the parameter n varied considerably with the composition of the starting mixtures. Sample C2 exhibits the fastest densification rate with $n = 1/3$, while A8 and L2 have the lowest shrinkage rate with $n = 1/11$. This is just opposite to the behaviour observed for sintering with a constant heating rate.

To densify nitrogen ceramics under atmospheric nitrogen pressure, 1800°C is the highest sintering temperature; above this severe thermal decomposition results in a high weight loss and prevents densification. For α' -sialon ceramics, as the temperature rises up to 1800°C with a moderate heating rate of 10°C/min, a relative density above 90% t.d. has been reached for all these samples. The further densification needs isothermal sintering at 1800°C, which progresses very slowly; after 60 min sintering the densities of these samples have been enhanced to about 95%. To achieve fully dense α' -sialon ceramics, a much longer sintering time is required.

The experimental results shown in this figure indicate that the densification of sialon ceramics is a mix of various processes, which vary with the composition of the mixtures and the sintering conditions.

4-4. MICROSTRUCTURAL DEVELOPMENT

Fig. 4-23 gives a series of fractographs of sample A2 as a function of the rising temperatures. Although the formation of an oxynitride liquid phase and the dissolution of nitrides as well as precipitation of α' -sialon had occurred at 1400°C, the remained solid particles were not sufficiently repacked, many large voids still remain and nearly all particles had point-contact with each other. The large voids collapsed at higher temperatures, due to the continuous rearrangement of remaining solid particles resulting from the increasing amount of the liquid phase and the smoothing of the particle surface. Moreover, the contact between particles was considerably improved due to material transport away from the contact-point.

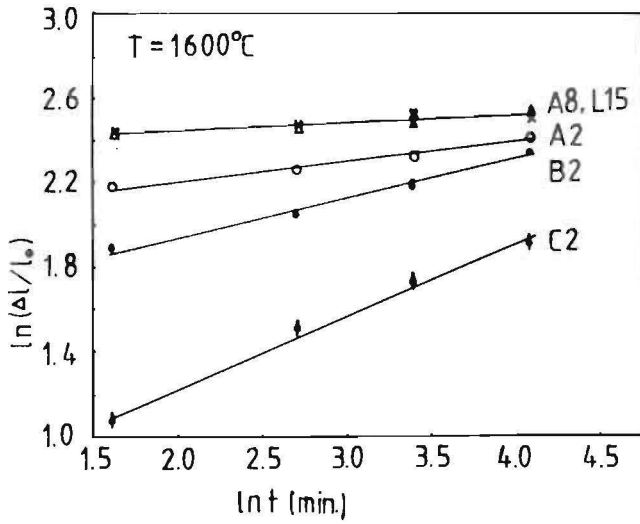


Fig. 4-22: A ln-ln plot of the shrinkage curves of α' -sialon ceramics in the isothermal sintering at 1600°C.

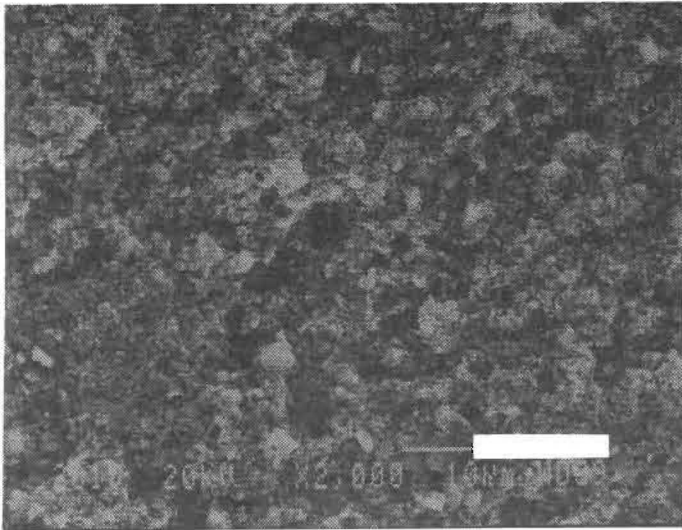


Fig. 4-23A: SEM micrographes of α' -sialon sample A2 after sintering at 1400°C. The bar is 10 μm .

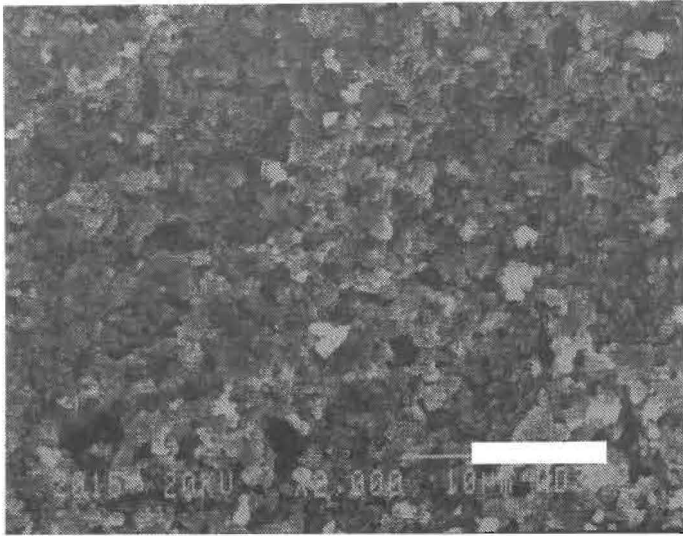


Fig. 4-23B: SEM micrographes of α' -sialon sample A2 after sintering at 1500°C. The bar is 10 μm .

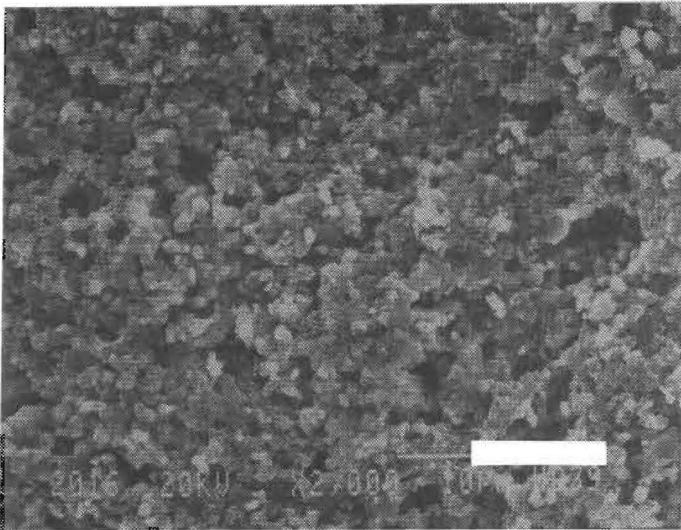


Fig. 4-23C: SEM micrographes of α' -sialon sample A2 after sintering at 1600°C. The bar is 10 μm .

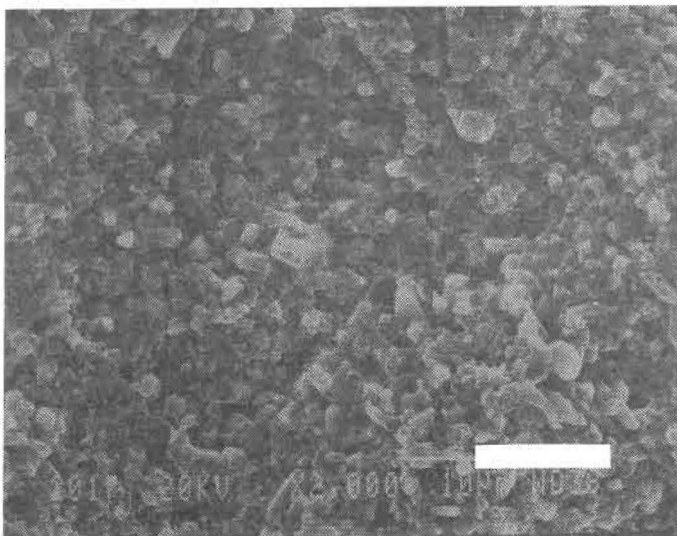


Fig. 4-23D: SEM micrographes of α' -sialon sample A2 after sintering at 1700°C. The bar is 10 μm .

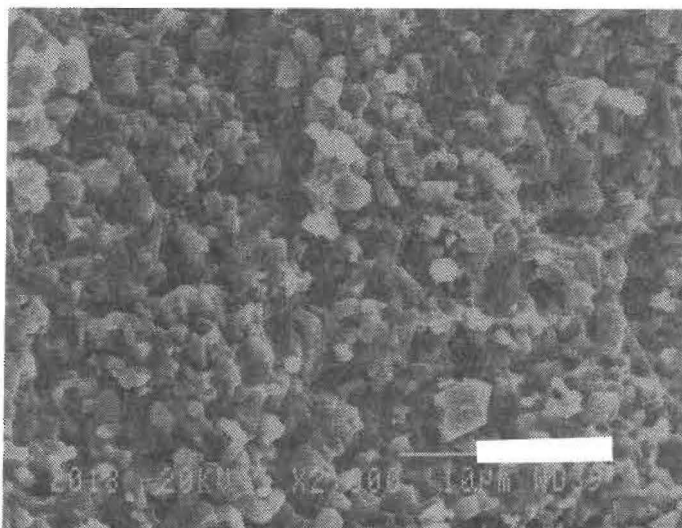


Fig. 4-23E: SEM micrographes of α' -sialon sample A2 after sintering at 1800°C. The bar is 10 μm .

The coarsening of the microstructure, in the case of sample A2, was observed almost at the beginning of the densification process, but proceeded very slowly. At 1600°C an average grain size of only 1 μm was reached. However, the grain growth then progressed rapidly with rising temperature and the mean grain size reached approximately 2.5 μm at 1800°C. The mean grain size together with the density was plotted as a function of the rising temperature in Fig. 4-24. Also the data of sample A8 are included in this figure. It is seen that the rapid grain growth observed in sample A2 above 1600°C corresponds well with the rapid increase of the density. However, the addition of Al₂O₃ powder to the mixtures suppressed the rapid grain growth above 1600°C. It is also seen that there was no rapid increase of the density in case of A8 (see Fig. 4-24). This figure also shows that the density increases very slowly in the isothermal sintering at 1800°C, while, the grain size is seen to increase considerably as a function of the sintering time.

The influence of the addition of Al₂O₃ powder was also followed in the case of the composite α'+β'-sialon samples A4 and A10. At 1400°C these two samples exhibited a minor difference in the microstructure, both with minor grain growth and point-contact among the solid particles, although a relatively extensive

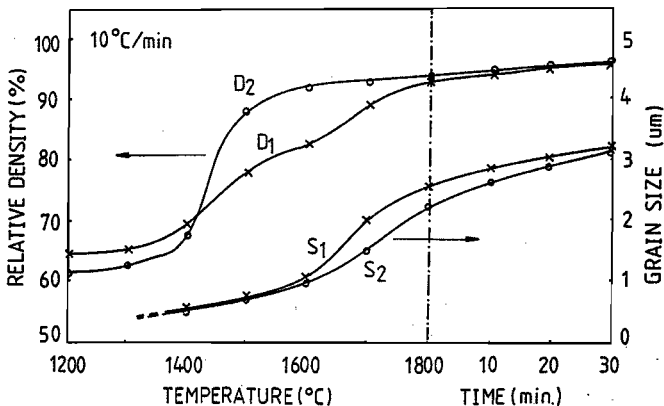


Fig. 4-24: Comparison of the density (D) and mean grain size (S) development during firing. D₁, S₁ are for A2 and D₂, S₂ for A8.

particle rearrangement occurred in A10 just as in A8. For sample A4, the microstructural development was similar to that in sample A2. The formation of the β' -sialon phase started approximately at 1480°C but the elongated grains of the β' -phase became visible only above 1600°C, probably due to the very small particles formed in the beginning. For sample A10, the coalescence of pores resulted in the formation of some very large voids, which was seen to be accompanied by a rapid densification, when the temperature reached 1500°C. These large voids collapsed easily at higher temperatures and subsequently promoted the densification. Thus a relative density higher than 90% was reached at 1600°C. The addition of Al_2O_3 powder to the starting mixtures greatly increases the oxide content and thus results in an increase of the liquid amount and a decrease of the liquid viscosity in the early stage of densification. In general, the grain growth of the β' -phase was observed to be much faster than that of the α' -phase.

The addition of La_2O_3 to the starting mixture exhibited a considerable influence on the grain growth, the rapid grain growth being suppressed. At 1800°C the mean grain size in sample L2 was smaller than 1.5 μm , while that in sample A2 was about 2.5 μm . A similar effect has been observed in the sintering of metallic materials in the presence of impurities [24]. La_2O_3 is expected not to be incorporated into the α' -sialon lattice, as discussed before, and thus to increase the liquid quantity during firing. As a consequence, the material diffusion distance through the liquid was enlarged, reducing the grain size in the final products.

The powder characteristics of the silicon nitride starting powders strongly influenced the microstructural development, as was expected. In samples B2 and C2 very little grain growth was observed during sintering and many large voids formed in the early stage of the sintering, remained at higher temperatures. Consequently porous ceramic products were obtained after sintering. It also should be pointed out that no collapse of large voids at higher temperatures was seen (see Figs. 4-18 and 4-19). The difference in the oxygen impurity content and other powder characteristics is expected to alter the quantity and the composition of the liquid phase existing during sintering. The minor impurities present at the surface of the starting powders also are expected to influence the wetting properties, which probably have an important influence on the microstructural development.

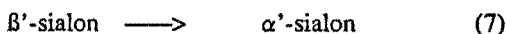
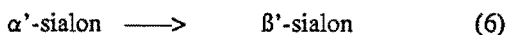
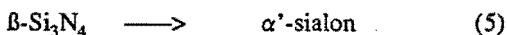
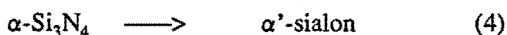
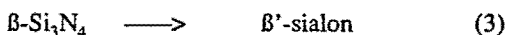
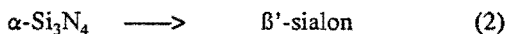
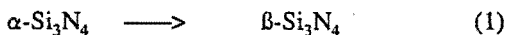
4-5. DISCUSSION AND SUMMARY

A. The mechanism of the formation of α' -sialon

The various compositions and amounts of oxides including sintering additives and impurities in the starting mixtures give different amounts and compositions of the liquid phase as the temperature rises above the eutectic temperature. As a consequence, the properties of the liquid phase, such as viscosity, spreading and wetting properties will vary and furthermore, the solubility of nitrides and oxides as well as the diffusivity in this liquid phase will change as well. In practice, however, the conversion rate from silicon nitride to sialons in both α' -sialon and α' + β' -sialon ceramics is independent of the amount and composition of the liquid phase during firing. Therefore the formation of sialons is assumed to be a reaction controlled process [25].

The mechanism of the formation of β' -sialon from β -silicon nitride was reported as a reconstructive phase transformation, similar to the α - β -phase transformation [26,27]. This phase transformation requires a liquid phase which allows the dissolution of silicon nitride and precipitation of β' -sialon. The similarity observed in the formation of α' - and β' -sialons, therefore, suggests that the mechanism of the phase transformation α - α' could be a reconstructive phase transformation as well [28].

In this system thermodynamically seven chemical reactions concerned with $\alpha(\alpha')$, $\beta(\beta')$ phase transformations would occur:



where reaction 1 is the α - β phase transformation which has been widely investigated [29-32] and has been generally accepted as a reconstructive transformation. It starts at about 1400°C and completes at 1800°C and occurs only in the presence of liquid or gas.

The reactions 2 and 3 are the formation reactions of β' -sialons, while the

reactions 4 and 5 are those for α' -sialons.

The reactions 6 and 7 indicate that the α' , β' could yield each other by chemical reactions [18-21], α' -sialon reacts with oxide giving β' -sialon, β' -sialon reacts with nitride giving α' -sialon. These two reactions also require the presence of a liquid phase. The phase transformation of α' - β' has been confirmed in the present work.

B. The mechanism of sintering of α' -sialon ceramics

Silicon nitride, as a highly covalent compound, possesses very low diffusion coefficients for silicon and nitrogen [1-5] and therefore can be densified only in the presence of sintering additives via liquid phase sintering [34]. Liquid phase sintering for both metallic and ceramic materials can be generally described to proceed in three overlapping stages [35-40]:

Stage I: primary particle rearrangement, immediately following the formation of the liquid phase, is brought about by the remaining solid particles sliding over each other under the action of capillary forces. The rate and extent of shrinkage will depend upon the viscosity and quantity of the liquid and its wetting properties.

Stage II: a solution-precipitation process will become operative if the solid particles have some solubility in the liquid phase. This also leads to a secondary rearrangement. Since the solubility at the contact points of solid particles is greater than that of other solid surfaces, material transport away from the contact points will allow the "centre to centre" distance between particles to decrease. Besides this contact flattening mechanism, a shape accommodating Ostwald ripening plays an important role.

Stage III: coalescence and closed pore elimination, requires a solid state sintering mechanism.

The densification of sialon ceramics certainly proceeds via the liquid phase, although it is more complicated than in the well known hard metals, since during the heating cycle, intermediate compounds form, phase transformations occur and some liquid constituents are incorporated into the structure.

The primary rearrangement is strongly dependent upon the amount and composition of the liquid phase, which appears around the eutectic temperature.

A low fraction and a high viscosity of the liquid phase will not lead to the primary rearrangement. Besides, the particle characteristics such as surface roughness, particle shape and size distribution as well as the solid contacts will sensitively influence this process as well.

The addition of Al_2O_3 or La_2O_3 powders to the starting mixtures increases the amount of oxides, and subsequently increases the amount of oxide liquid phase. Thus the primary rearrangement occurs immediately after the formation of the liquid phase. The composition of the liquid phase is another important factor for the primary rearrangement. For instance, sample A2 contains more oxide, but the oxide composition in A4 is SiO_2 -richer, and as a consequence, the primary rearrangement occurs in sample A4 as well.

Following the primary rearrangement, the dissolution precipitation process starts as the temperature increases. In the early stage, the contact flattening mechanism is dominant due to a large amount of the liquid phase and a small contact area [23,41]. As the sintering process goes on, the amount of the liquid phase decreases due to the incorporation of some liquid constituents into the sialon crystal lattice and the contact area increases. The sintering via the contact flattening mechanism slows down dramatically. Experimental results indicate that shape accommodating Ostwald ripening plays an essential role for densification in the later stage. It is always accompanied by evident grain growth, while contact flattening plays an unimportant role. One example is the sintering of samples B2 and C2, in which no evident grain growth is observed and consequently further densification is not successfully obtained.

Furthermore, the formation and dissolution of some intermediate compounds exhibit some influence on the densification as well, but they hardly influence the density and microstructure of the final ceramics.

C. Summary

In summary, it is seen that the preparation of α' -sialon ceramics with a direct formation method is a very complicated process. The formation of α' -sialon is a process which requires the presence of a liquid phase but proceeds independent of the quantity and composition of this liquid phase. Thus the formation of α' -sialon is assumed to be a reaction controlled process. Furthermore

the similarity of the formation of α' -sialon and β' -sialon suggests that the formation of α' -sialon occurs via a secondary reconstructive phase transformation, just as for β' -sialon. In general, the formation of α' -sialon and $\alpha' + \beta'$ -sialons is complete as the temperature rises up to 1800°C, but can be reached also at lower temperatures, e.g. 1600°C for 1 hr.

In contrast, the densification of α' -sialon ceramics is strongly affected by the addition of some oxides either as a modifier or an extra sintering additive. Furthermore, the characteristics of the silicon nitride starting powders also strongly influence the densification process. The experimental results indicate that in the early stage, contact flattening is very important for the densification. After the particle contact has improved and some liquid constituents have been incorporated into the α' -sialon lattice, thus the quantity of the liquid is decreased, the Ostwald ripening mechanism becomes dominant for the further densification. This is often accompanied by a rapid grain growth.

Since the constituents of the liquid are gradually absorbed during sintering, the completion of the densification is rather difficult and proceeds mainly by solid state sintering. This often results in a coarsening of microstructure. To overcome this difficulty, we have used gas pressure sintering as described in the next chapter.

4-6. REFERENCES

1. Kijima, K. and Shirasaki, S., J. Chem. Phys., 1976,65,2668.
2. Kunz, K.P., Sarin, V.K., Davis, R.F. and Bryan, S.R., Mater. Sci. and Eng., 1988,A105/106,47.
3. Batha, H.D. and Whitney, E.D., J. Am. Ceram. Soc., 1973,56,365.
4. Cooper, A.R. and Major, L.D., NTIS, Rep. AD-A-069004, 1979.
5. Wuensch, B.J. and Vasilos, T., NTIS, Final Rep. AD-A-021175, 1975.
6. Raider, S.I., Flitsch, R., Aboof, J.A. and Plisken, W.A., J. Electrochem. Soc., 1976,123,560.
7. Peuckert, M. and Greil, P., J. Mater. Sci., 1987,22,3717.
8. Schwier, G. and Nietfeld, G., Sprechsaal, 1988,121,175.
9. Rahama, M.N., Boiteux, Y. and DeJonghe, L.C., Am. Ceram. Soc. Bull., 1986,65,1171.

10. Jenett, H., Bubert, H. and Grallath, E.,
Fresenius Z. Anal. Chem., 1989,333,502.
11. Levin, E.M. and McMurdie, F.H.(eds.), Phase Diagrams for Ceramists,
1975, Fig. 2586, Am. Ceram. Soc., Columbus, Ohio.
12. O'Meara, C., Dunlop, G.L. and Pompe, R., High-tech Ceramics,
ed. Vincenzini, P., 1987, p265, Elsevier Applied Publishers B.V.,
Amsterdam.
13. Huang, Z.K., Greil, P. and Petzow, G., J. Am. Ceram. Soc., 1983,66,C-96.
14. Stutz, D., Greil, P. and Petzow, G., J. Mater. Sci. Lett., 1986,5,335.
15. Slasor, S. and Thompson, D.P., J. Mater. Sci. Lett., 1987,6,315.
16. Slasor, S. and Thompson, D.P., Non-oxide Technical and Engineering
Ceramics, ed. Hampshire, S., 1986, p223, Elsevier Applied Sciences.
17. Gowda, G., J. Mater. Sci. Lett., 1986,5,1029.
18. Jack, K.H., Progress in Nitrogen Ceramics, ed. Riley, F.L., 1983, p45,
NATO ASI Series E65, Martinus Nijhoff, The Hague.
19. Sun, W.Y., Walls, P.A. and Thompson, D.P., Non-oxide Technical and
Engineering Ceramics, ed. Hampshire, S., 1986, p105, Elsevier Applied
Science.
20. Cao, G.Z., Metselaar, R. and Ziegler, G., Euro-Ceramics, eds. de With, G.,
Terpstra, R.A. and Metselaar, R., 1989, p346, Elsevier Applied Science.
21. Thompson, D.P., Sun, W.Y. and Walls, P.A., Ceramic Materials and
Components for Engines, eds. Bunk, W. and Hausner, H., 1986, p643,
DKG, Berlins.
22. Cao, G., Huang, Z.K. and Yan D.S., Science in China, 1989,A32,429.
23. German, R.G., Liquid Phase Sintering, 1985, Plenum Press, New York.
24. Kingery, W.D., Bowen, H.K. and Uhlmann, D.R., Introduction to
Ceramics, 1976, John Wiley & Sons.
25. Cao, G.Z., Metselaar, R. and Ziegler, G., Presented at the 7th Cimtec,
Italy, June 1990.
26. Hampshire, S. and Jack, K.H., Progress in Nitrogen Ceramics,
ed. Riley, F.L., 1983, p225, NATO ASI Series E65, Martinus Nijhoff,
The Hague.

27. Hwang, C.M. and Tien, T.Y., Sintering 87, ed. Somiya, S. et al., 1988, p1028, Elsevier Applied Science.
28. Cao, G.Z. and Metselaar, R., to be published in Chemistry of Materials.
29. Messier, D.R., Riley, F.L. and Brook, R.J., J. Mater. Sci., 1978,13,1199.
30. Buerger, M.J., Phase Transformations in Solids, eds. Smoluchowski,R. et al., 1951, p183, Wiley, New York.
31. Messier, D.R. and Riley, F.L., Progress in Nitrogen Ceramics, ed. Riley, F.L., 1983, p141, NATO ASI Series E65, Martinus Nijhoff, The Hague.
32. Sarin, V.K., Mater. Sci. and Eng., 1988,A105/106,151.
33. Xu, Y.R., Huang, L.P., Fu, X.R. and Yan, D.S., Scientia Sinica, 1985,A28,556.
34. Wild, S., Grievesson, P., Jack, K.H. and Latimer, M.J., Special Ceramics 5, ed. Popper, P., 1972, p377, B.C.R.A., Stoke-on Trent.
35. Kingery, W.D., J. Appl. Phys., 1959,30,301.
36. Petzow, G. and Kaysser, W.A., Science of Ceramics 10, ed. Hausner, H., 1980, pp269, DKG.
37. Popper, P., Progress in Nitrogen Ceramics, ed. Riley, F.L., 1983, pp187.
38. Weiss, J., Ann. Rev. Mater. Sci., 1981,11,381.
39. Weiss, J. and Kaysser, W.A., Progress in Nitrogen Ceramics, ed. Riley, F.L., 1983, p169, NATO ASI Series E65, Martinus Nijhoff, The Hague.
40. Greskovich, C. and Rossolowski, J.H., J. Am. Ceram. Soc., 1976,59,336.

CHAPTER FIVE. GAS PRESSURE SINTERING OF α' -SIALON CERAMICS

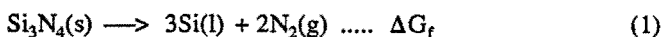
5-1. GAS PRESSURE SINTERING

As has been discussed before, traditional methods of sintering ceramics cannot be used to densify nitrogen ceramics. Therefore some methods have been developed, which are described in literature as [1]: "reaction-bonding" [2-3], "sintering reaction bonding" [4-5], "pressureless sintering" [6-7] and "sintering under elevated pressures" [8-14].

To achieve fully dense α' - and mixed $\alpha'+\beta'$ -sialon ceramics, gas pressure sintering as an advanced sintering method was used. In this chapter, after a brief overview of the fundamentals of gas pressure sintering, we will mainly focus on the investigation of the gas pressure sintering parameters. The two step sintering process will be discussed, and then the sintering parameters are to be optimized by using a statistic evaluation method. Some other variables for sintering are discussed, too. The discussion and summary is presented at the end of this chapter.

Gas pressure sintering (GPS), in which an isostatic pressure is employed at high temperatures, was developed in recent years for densification of high purity silicon nitride powder with a small amount of additives, so that fully dense nitrogen ceramics with complex shapes and good mechanical properties can be expected [11-14]. High nitrogen gas pressure employed during sintering will hinder the thermal decomposition of nitrides and oxynitrides that occurs roughly above 1850°C under one bar of nitrogen. This higher sintering temperatures can be used in gas pressure sintering.

The fundamentals of gas pressure sintering of silicon nitride based ceramics have been elaborated by Prochazka et al. [15-16]. It is well known, that the basic problem in sintering nitrogen ceramics is the thermal decomposition of silicon nitride at high temperature:



Once the decomposition reaction occurs the equilibrium silicon partial pressure, P_{Si} , is built up:



so the partial pressures over silicon nitride have to obey the following equation:

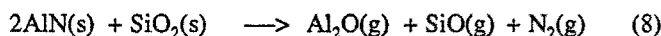
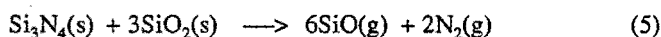
$$P_{\text{Si}}^3 \times P_{\text{N}_2}^2 = K$$

where the equilibrium constant K at temperature T , is given by:

$$K = \exp \{-(\Delta G_f + 3\Delta G_g)/RT\} \quad (3)$$

From thermodynamic data the silicon vapour pressure in equilibrium with silicon nitride as a function of nitrogen pressure and temperature can be calculated as demonstrated in Fig. 5-1. The coexistence limit between silicon and silicon nitride runs from bottom left to top right. This figure shows that a certain silicon partial pressure and nitrogen pressure are required to prevent the continuous thermal decomposition during firing; it also suggests to use a sufficiently high nitrogen pressure to keep the system to the right of the solid-liquid coexistence boundary. However, in addition to silicon gas, silicon nitride is also in equilibrium with other gaseous substances, such as SiN , Si_2N and Si_2 [17].

When a mixture of silicon nitride, aluminium nitride and the additive oxides, such as Y_2O_3 , Al_2O_3 is fired at high temperatures, the following thermal decomposition reactions can occur [18-21]:



Thermodynamic analysis [21] indicates these volatilization reactions can be suppressed effectively by using high pressure nitrogen gas. Therefore, a "rule of thumb" is to carry out the sintering process at a nitrogen pressure at least 1 MPa higher than the equilibrium pressure given in Fig. 5-1.

Secondly, in the case of sintering nitride ceramics under elevated nitrogen pressures, high temperatures can be employed to achieve complete densification of silicon nitride ceramics, so that a higher atom mobility is expected. As a consequence the amount of additive oxides can be reduced [22] as compared with that in pressureless sintering. The use of a lower additive concentration is expected

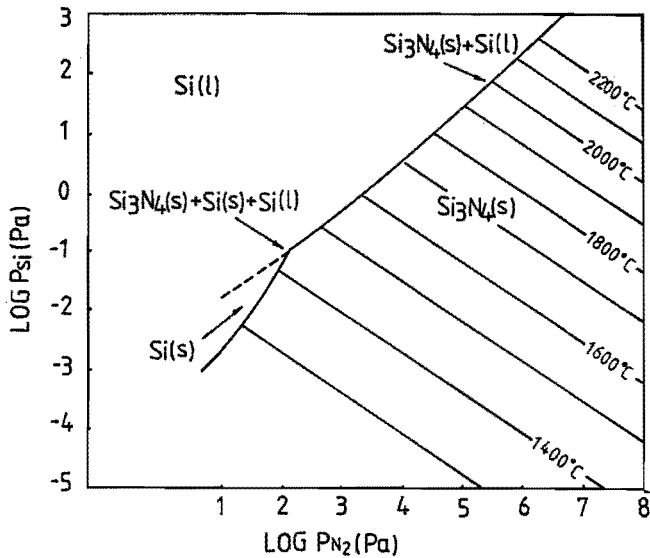


Fig. 5-1: Silicon vapour partial pressure in equilibrium with silicon nitride as a function of temperature and nitrogen partial pressure (15,16).

to yield a lower residual glass content at grain boundaries, and therefore would improve the mechanical properties of the densified materials, especially at high temperatures.

Thirdly, a high nitrogen gas pressure also provides an extra sintering driving force. A typical magnitude of the driving force in pressureless sintering (surface tension divided by the neck radius) is about 1 MPa [23,24]. The applied nitrogen gas pressure of 7-10 MPa (70-100 bar), which is about one order higher than the driving force in liquid phase sintering, is a very important factor for the final densification of nitride ceramics because residual pores can be removed effectively due to this additional driving force [25].

Finally, compared with hot pressing and hot isostatic pressing, gas pressure sintering is an inexpensive way to mass produce complicated shaped, fully dense silicon nitride and oxynitride ceramic components with improved mechanical properties at high temperatures [26].

5-2. GAS PRESSURE SINTERING WITH TWO STEPS

To achieve full densification of nitrogen ceramics, a gas pressure sintering process with two steps was proposed in literature [11,15,27-28]: a) the first step is to close surface pores under low nitrogen pressure at moderate sintering temperatures, and b) at the second step a high sintering temperature together with a higher nitrogen gas pressure are subsequently used for the final densification.

According to literature [29-30], after the closed-pore condition is reached these closed pores will decrease in size corresponding to

$$R_e = [P_o R_o^3 / (P_a R_e + 2\tau_{sg/lg})]^{1/2} \quad (9)$$

where R_e = final pore size

R_o = initial pore size

P_o = pressure in the initial pore

P_a = applied nitrogen pressure

$2\tau_{sg/lg}$ = surface tension

so that the final densification will be promoted effectively by use of external high gas pressures. If the closed-pore condition is not obtained during the first step, the applied high nitrogen gas pressure will act in the pore too and oppose to the driving force for pore closure.

Figs. 4-18 and 4-19 show the densification behaviour of samples A2, B2 and C2 during firing with two isothermal sintering steps. The first was a presintering step at a moderate temperature of 1800°C for 10 min under a low nitrogen pressure of 0.5 MPa, and then the second step (the final step) followed at 1900°C for 15 min under 10 MPa N₂. The densification behaviour and the sintering mechanism during heating up (to 1800°C) were discussed in chapter four. The further densification in the case of sample A2 was considerable by heating at high temperature under high nitrogen pressure, while a very minor or no further shrinkage was observed in the case of B2 and C2. Fig. 5-2 shows the density and weight loss for these three samples A2 (LC-12), B2 (DFV0014) and C2 (DFV0015). The first bars are the densities achieved after the presintering step, the second and the third are the density and total weight loss observed after the final sintering step, respectively. It is seen that the high nitrogen pressure employed at the second sintering step caused the further densification only in the case of sample A2, where the density increased from 97% to above 99% and the

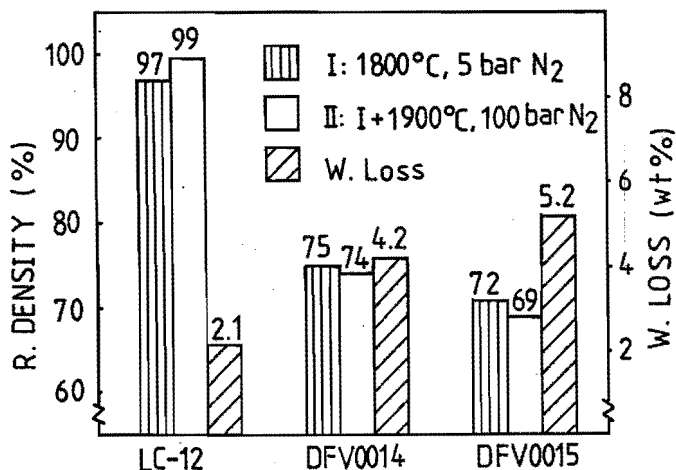


Fig. 5-2: Relative densities of α' -sialon from different Si_3N_4 powders before and after high pressure sintering. Also the overall weight loss is presented.

total weight loss was less than 2.0 wt%. However, for samples B2 and C2, the relative density was slightly decreased by undergoing the final sintering step and a high weight loss (above 4 wt%) was observed. This can be understood from the microstructure observation after the first sintering step. Fig. 5-3 shows that sample A2 has reached a closed pore structure, while B2 and C2 (Fig. 5-4) have a large number of interconnected pores. The increased weight loss for B2 and C2 is due to the large internal surface area in comparison with A2.

The effect of the high nitrogen pressure employed at the second sintering step on the densification is also demonstrated in Fig. 5-5, which shows that the high pressure promoted the final densification effectively. Samples with a relative density less than 82% were further densified as well under high nitrogen pressures. Microstructure observation indicates that even though there was a number of pores existing both in the surface and bulk, most of them were not connected to each other, i.e. some pores were closed, so that the high nitrogen pressure applied also led to a further densification in these samples, as can be expected according

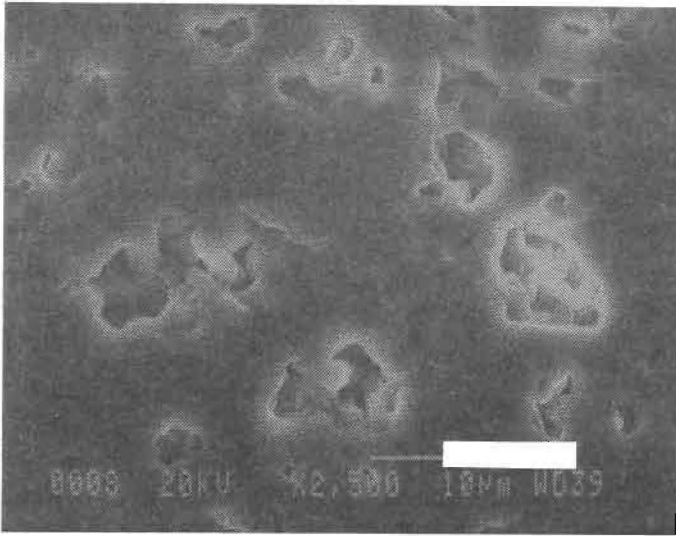


Fig. 5-3: SEM micrograph of sample A2 indicating a closed pore structure after presintering. The bar is 10 μm .

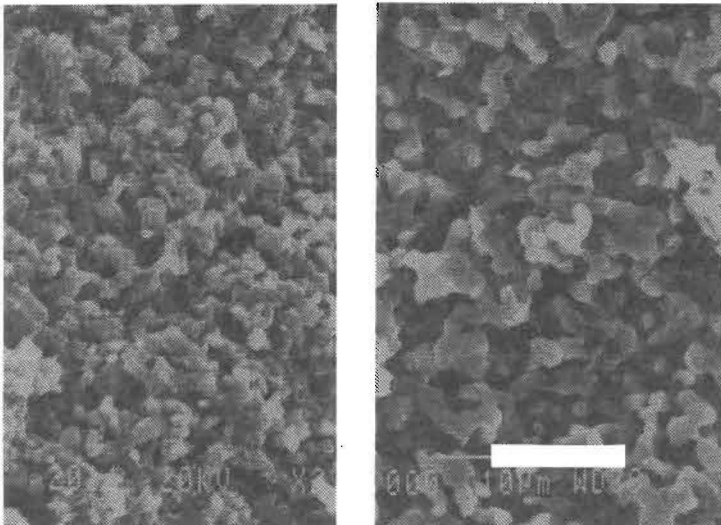


Fig. 5-4: SEM micrographes showing the interconnected pores existing in samples B2 (left) and C2 (right) after presintering. The bar is 10 μm .

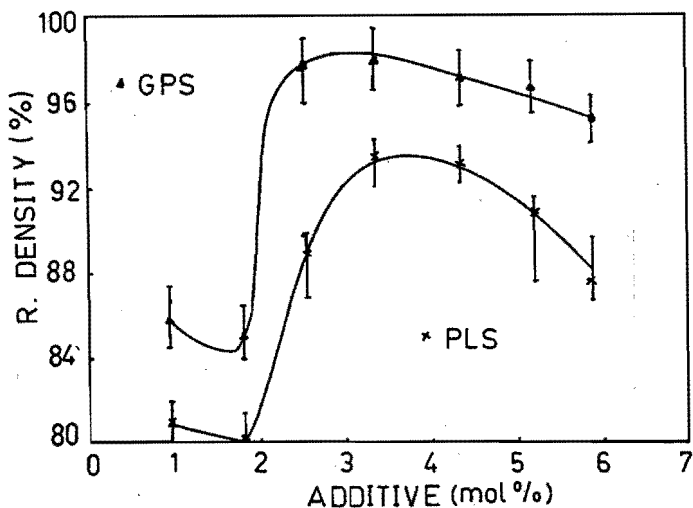


Fig. 5-5: Relative densities of various α' -sialons and $\alpha'+\beta'$ -sialons achieved before (PLS) and after high pressure sintering (GPS). The additive is yttria and lanthanum oxide (with samples A1 to A6, and L2, see Table 3-3).

to equation (9). It is also seen that the final density was slightly declined with increasing oxide additive(s), which will be discussed later in this chapter.

Regarding to equation (9), the initial pressure in the presintering step should be as low as possible, but in practice, a minimum nitrogen pressure is required to suppress the thermal decomposition of silicon nitride and aluminium nitride during sintering. Hence in the present investigation an initial nitrogen pressure of 0.5 MPa was selected for all experiments.

Theoretically a higher pressure during the second step should lead to a smaller pore size and a higher density. However, the experimental results indicate that the influence of the final pressure decreases as the pressure increases. There is a very minor difference in the final densification by using a high nitrogen pressure of 7 MPa or 10 MPa. However, the higher nitrogen pressure favours to enhance the solubility of silicon nitride into the liquid [41]. Furthermore it inhibits grain growth, so that a nitrogen pressure of 10 MPa, as the highest pressure allowed in the furnace, was selected for the final sintering step.

The temperature in the presintering step is another process parameter which sensitively influenced the weight loss as shown in Fig. 5-6. The weight loss rapidly increased with temperatures above 1850°C due to the severe thermal decomposition of nitride or oxynitride, while the holding time during presintering showed a negligible influence on the weight loss (see Fig. 5-7), unless the temperature was above 1850°C. The weight loss at the final step was very small if the closed surface pore condition was reached during presintering.

Besides the effect on the weight loss, the temperature and holding times of both the presintering and the final step played an even more important role for the densification and the microstructure. A higher temperature and longer sintering time favour not only the densification but also the negative effects such as grain growth and coalescence [22]. Therefore, a careful selection of the sintering conditions should be made to achieve a fully dense nitrogen ceramic with a fine-grained microstructure.

The heating rate of 10°C/min was used for heating up as stated in chapter three, and the high nitrogen pressure was applied immediately at the end of the presintering, in such a way that the desired pressure of 10 MPa was reached simultaneously with the desired final temperature.

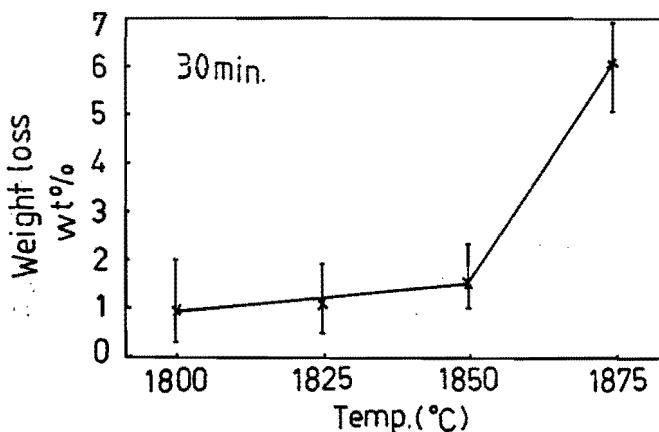


Fig. 5-6: The influence of temperature during presintering on the mean weight loss of all samples described in this thesis except B2 and C2.

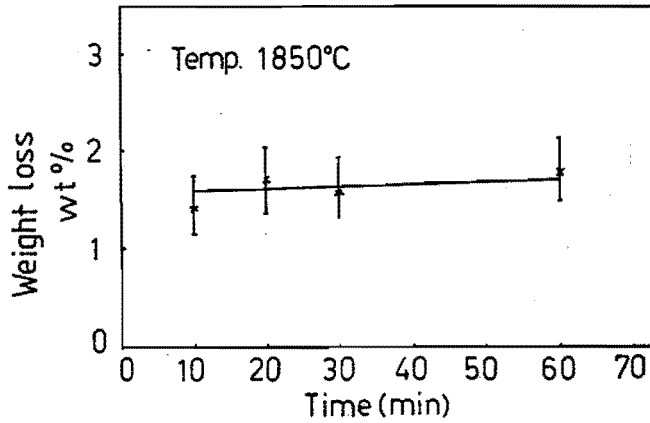


Fig. 5-7: The influence of the holding time during the presintering step on the weight loss for all samples except B2 and C2.

5-3. STATISTICAL EVALUATION

If we neglect the influence of the heating rate, there are temperature, holding time and pressure as variables. This means six variables for a two step process. Preliminary experimental results show that the density values vary with the conditions during both the first and second step, as can be seen from Fig. 5-8. Therefore, the attention is focussed first on the influence of the presintering condition. The second step was performed at 1900°C for 30 min under 10 MPa nitrogen pressure, while the pressure in the presintering step was fixed at 0.5 MPa. Thus only two of six sintering parameters are left as shown in Fig. 5-9. Even with this simplification, a large number of experiments is necessary.

In order to find the optimum sintering condition for α '-sialon ceramics with various mixture compositions, a statistical evaluation method proposed by Hurst et al. [31] for ceramic materials was used. The method, known as response surface methodology, is a technique for mathematically mapping the experimental data resulting from the designed experiments [32-33]. Equations are generated, which describe a response surface and can therefore be used to predict optimum

conditions for sintering of silicon nitride based ceramics [22]:

$$Y = C_0 + C_1T + C_2t + C_3T^2 + C_4t^2 + C_5Tt + E$$

where Y is the "Yield", such as the density, weight loss or other properties, T, t are the respective isothermal sintering temperature and time during presintering, C_i are constants and E error. Thus each experiment leads to one equation. With a minimum number of six experiments, the C_i-constants can be evaluated by numerical calculation. More than six experiments allow also estimates of the errors involved. With these C_i-values curves for constant density values are calculated and the contour-curves can be plotted as a function of temperature-time-conditions.

Experimental sintering conditions, for the statistical evaluation in the present investigation were plotted in Fig. 5-10. Only the density was selected here to optimize the sintering conditions, while the microstructure evolution will be

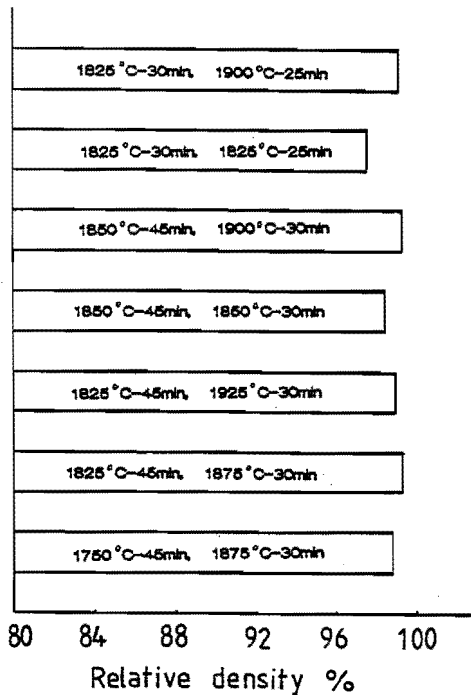


Fig. 5-8: The mean relative densities as a function of sintering conditions for all samples except B2 and C2.

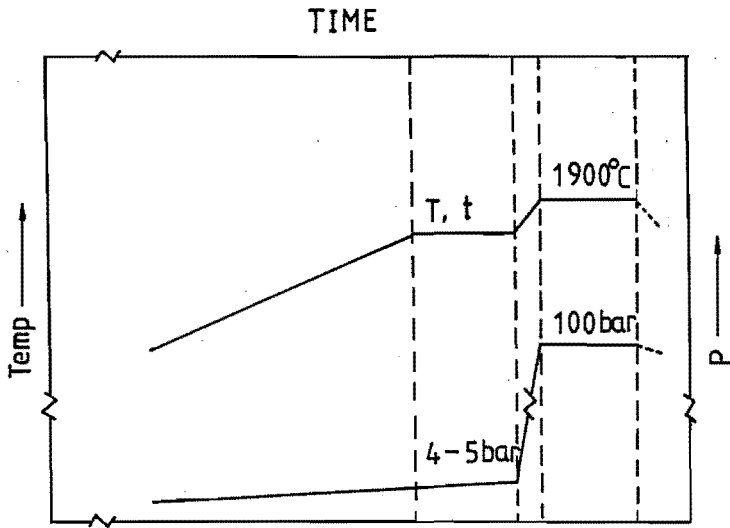


Fig. 5-9: A schematic diagram of the gas pressure sintering process with two varying parameters.

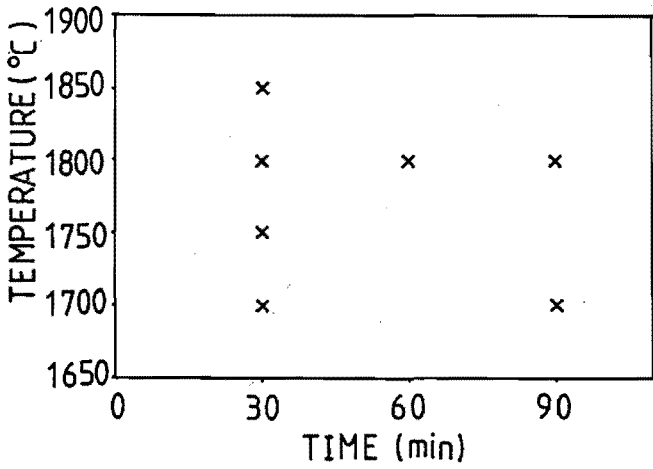


Fig. 5-10: Sintering conditions chosen for the statistical evaluation.

discussed later in this chapter. It also should be noted that for all experiments the weight loss was less than 2 wt%. The specimens, densified by using gas pressure sintering, were first ground to remove the surface layer of about 0.5 mm and then used to measure the density.

The corresponding densities are given in Table 5-1. The experiments were conducted at least three times for each specimen. Since there are very little or no open pores left in the final products, the density value can be determined very precisely.

The C_i -constants calculated from the density are presented in Table 5-2. Some of the isodensity contours as a function of the sintering temperature and time are shown in Figs. 5-11 to 5-18. The density data and the isodensity contours for sample L2 were not included because of the swell of some specimens in some experiments, as will be discussed later in this chapter.

Fig. 5-11 shows the isodensity contours for sample A1. It indicates that the optimum condition for densification is approximately 1775°C for about 75 min. The density decreases as the sintering condition shifts away from this optimum one, e.g. if the temperature used was lower than 1700°C the density was lower than 3.32 g/cm³. In this figure the crosses indicate the density data observed in experiments. It is seen that the experimental results are well in agreement with the calculated isodensity contours. Similar conclusions can be drawn from the other figures with an exception of Fig. 5-12.

Fig. 5-12 is unlikely in practice, probably due to improper design of experimental conditions, since temperatures higher than 1850°C during presintering resulted in a very severe thermal decomposition and thus no further densification can be achieved.

The optimum sintering conditions derived from the respective figures are summarized in Table 5-3.

The optimum temperature is always in the range 1775°C to 1820°C with a holding time of 50 min to 75 min. Therefore, a general conclusion can be drawn that the variation of the composition of the mixtures and the final products exerts a minor influence on the densification in the presintering step.

It should be noted here that if a higher sintering temperature and/or a longer holding time are used in the second step, the isodensity contours will

Table 5-1: The density values for statistical evaluation

Temp. (°C)	1700	1700	1750	1800	1800	1800	1850
time(min)	30	90	30	30	60	90	30
A1	3.2810	3.3193	3.3206	3.3292	3.3319	3.3238	3.3125
A2	3.2223	3.2489	3.2856	3.2843	3.2926	3.2839	3.2794
A3	3.2125	3.2349	3.2549	3.2806	3.2839	3.2338	3.2794
A4	3.2061	3.2131	3.2217	3.2259	3.2314	3.2139	3.2200
A7	3.2653	3.2220	3.2812	3.2751	3.2842	3.2594	3.2715
A8	3.2337	3.2361	3.2368	3.2613	3.2705	3.2586	3.2591
A9	3.1460	3.2042	3.2212	3.2178	3.2226	3.2158	3.2089
A0	3.1029	3.2181	3.2236	3.2217	3.2311	3.2273	3.2158

Table 5-2: Constant values of C_i

	$C_0+E(10^1)$	$C_1(10^{-2})$	$C_2(10^{-1})$	$C_3(10^{-6})$	$C_4(10^{-2})$	$C_5(10^{-4})$
A1	-1.3275	1.8325	0.1203	-5.0600	-0.0006	-0.0633
A2	0.1344	2.3600	-0.0907	-0.7200	-0.0009	0.0567
A3	-1.5363	2.0010	0.2660	-5.3800	-0.0030	-0.1323
A4	-0.3476	0.7344	0.0664	-2.0200	-0.0013	-0.0295
A7	-0.5358	0.9766	-0.0451	-2.7667	-0.0014	0.0324
A8	-1.4951	1.9713	0.1732	-5.3400	-0.0012	-0.0887
A9	-0.0025	0.3772	-0.0313	-1.1000	-0.0006	0.0215
A0	0.0829	0.2757	-0.0173	-0.8000	-0.0007	0.0150

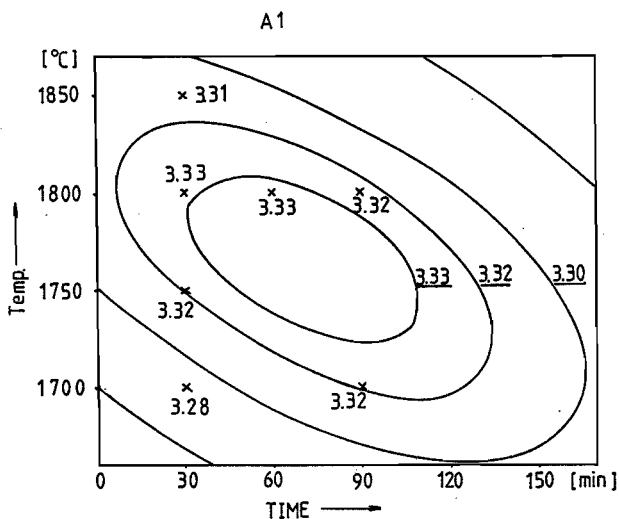


Fig. 5-11: Isodensity contours for sample A1, as a function of time and temperature during presintering under 0.5 MPa N_2 . Final sintering was performed at 1900°C for 30min under 10 MPa N_2 .

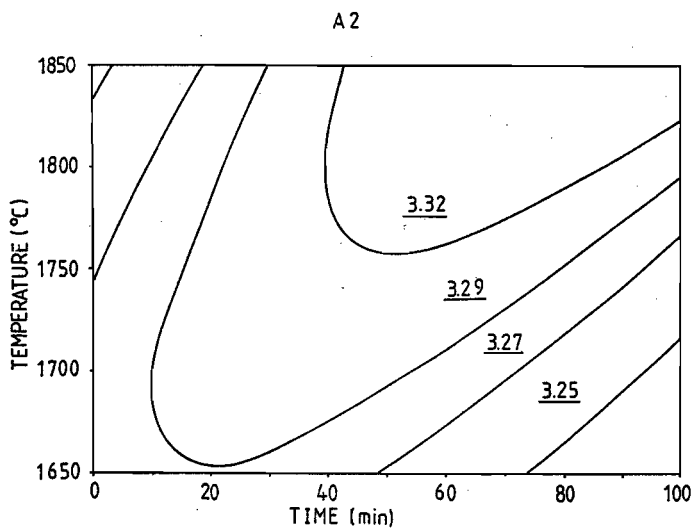


Fig. 5-12: Isodensity contours for sample A2, as a function of time and temperature during presintering under 0.5 MPa N_2 . Final sintering was performed at 1900°C for 30min under 10 MPa N_2 .

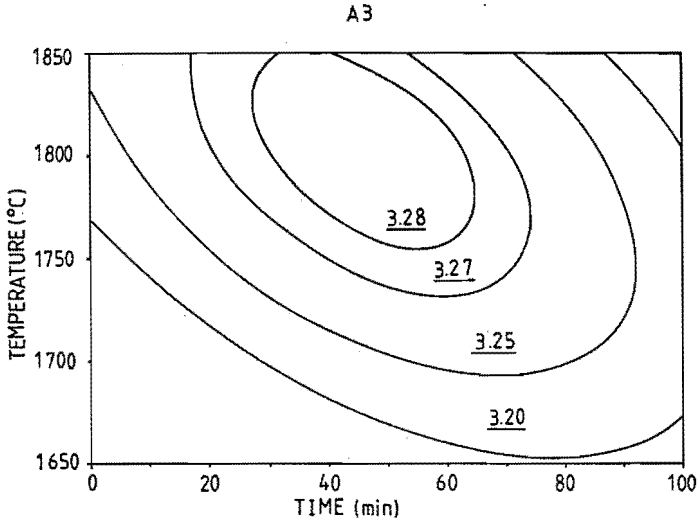


Fig. 5-13: Isodensity contours for sample A3, as a function of time and temperature during presintering under 0.5 MPa N₂. Final sintering was performed at 1900°C for 30min under 10 MPa N₂.

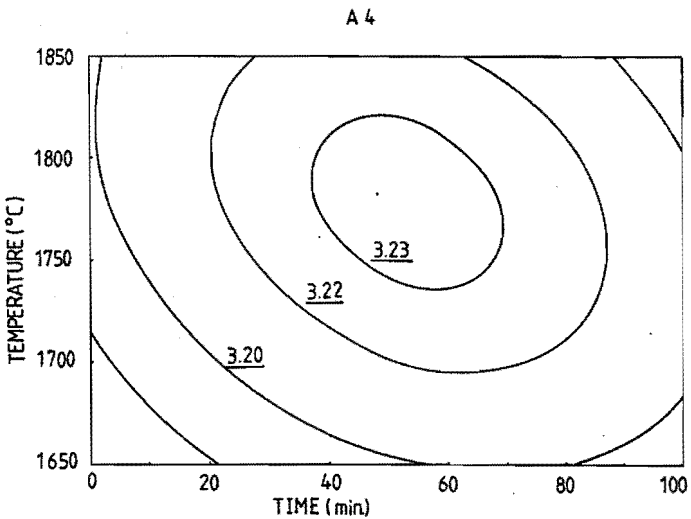


Fig. 5-14: Isodensity contours for sample A4, as a function of time and temperature during presintering under 0.5 MPa N₂. Final sintering was performed at 1900°C for 30min under 10 MPa N₂.

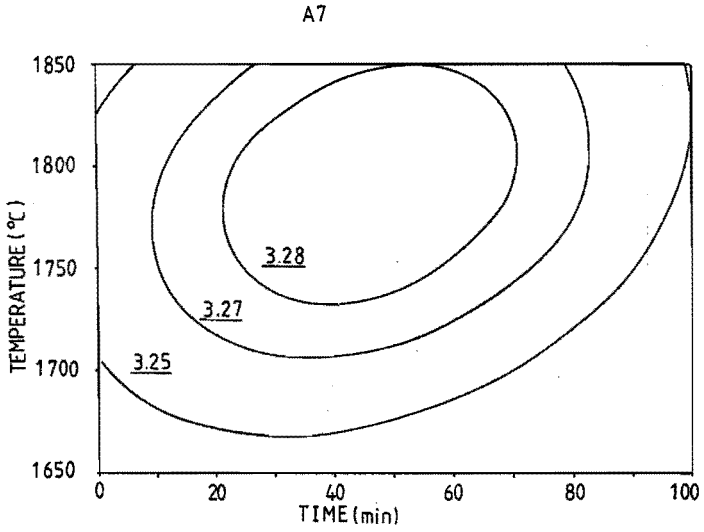


Fig. 5-15: Isodensity contours for sample A7, as a function of time and temperature during presintering under 0.5 MPa N_2 . Final sintering was performed at 1900°C for 30min under 10 MPa N_2 .

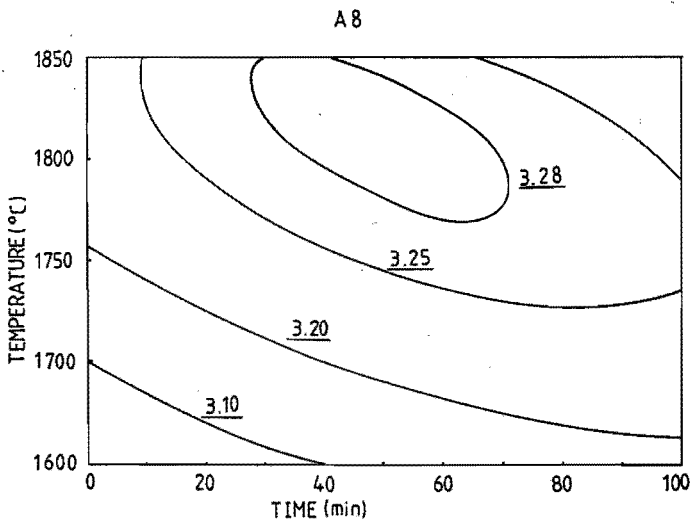


Fig. 5-16: Isodensity contours for sample A8, as a function of time and temperature during presintering under 0.5 MPa N_2 . Final sintering was performed at 1900°C for 30min under 10 MPa N_2 .

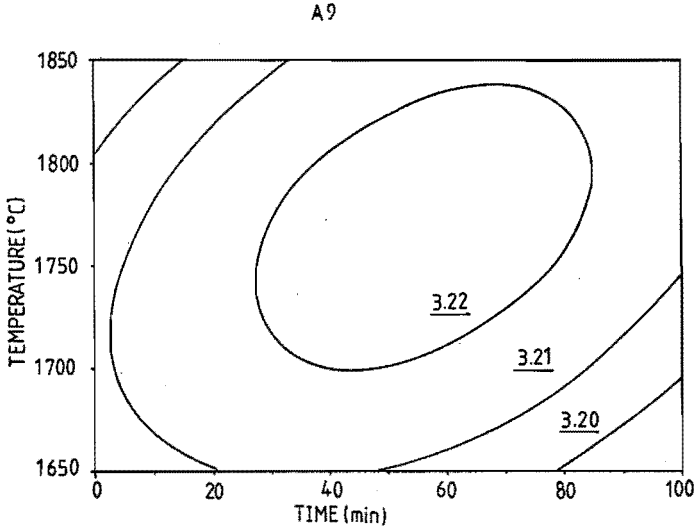


Fig. 5-17: Isodensity contours for sample A9, as a function of time and temperature during presintering under 0.5 MPa N_2 . Final sintering was performed at 1900°C for 30min under 10 MPa N_2 .

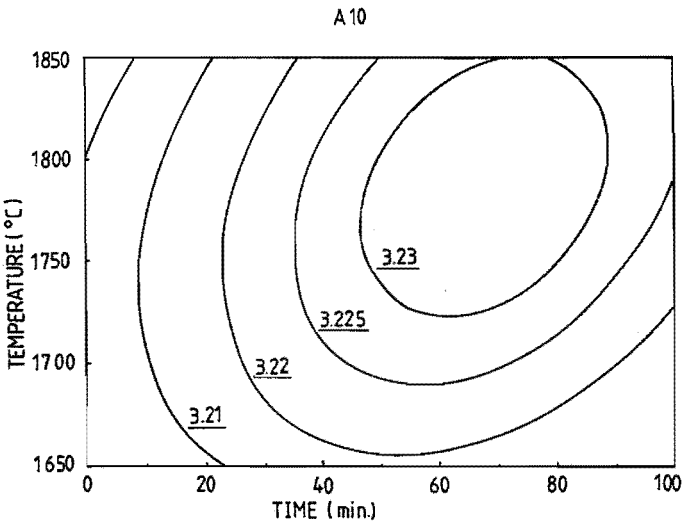


Fig. 5-18: Isodensity contours for sample A10, as a function of time and temperature during presintering under 0.5 MPa N_2 . Final sintering was performed at 1900°C for 30min under 10 MPa N_2 .

expand. The contours with lower density values will expand faster. As a consequence, the density differences generated in the presintering step will be greatly reduced by prolonging the final sintering process or using higher temperatures.

To optimize process parameters, it is necessary to consider the influence on the microstructure and the subsequent properties of the final products. This will be discussed later in this chapter.

Table 5-3: The optimum presintering parameters

Sample	Temperature	Time
A1	1775°C	75 min
A2	—	—
A3	1800°C	50 min
A4	1775°C	55 min
A7	1800°C	50 min
A8	1820°C	50 min
A9	1775°C	55 min
A10	1800°C	65 min

5-4. OTHER FACTORS

A. Nitrogen gas

Fig. 5-19, a back-scattered SEM micrograph, gives a comparison of the composition between the surface layer and the bulk of the composite α' + β' -sialon sample A4, densified by using gas pressure sintering. In the bulk there are black bars dispersed in a grey matrix phase, also with a small amount of white spots, but in the surface layer no black bars are observed. The selected area electron diffraction and EDS analysis (see next chapter) indicates that the black bars are β' -sialon and the grey matrix is the α' -sialon phase, while the white spots are an yttrium-rich amorphous phase retained at grain boundaries.

Further analysis results are given in Fig. 5-20, which shows the composition determined by using XRD as a function of the depth from the surface. It is seen

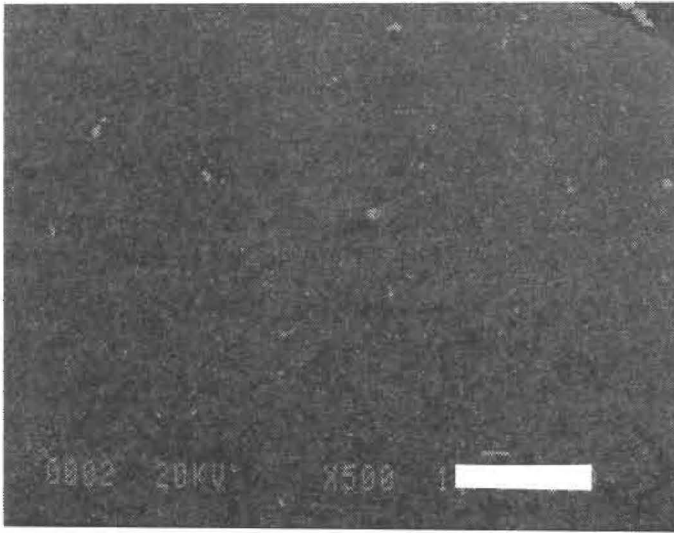


Fig. 5-19: The back scatter SEM picture showing the difference in the surface (top right) and the bulk composition (bottom left) of α' + β' -sialons after gas pressure sintering in case of sample A4. The bar is 50 μm .

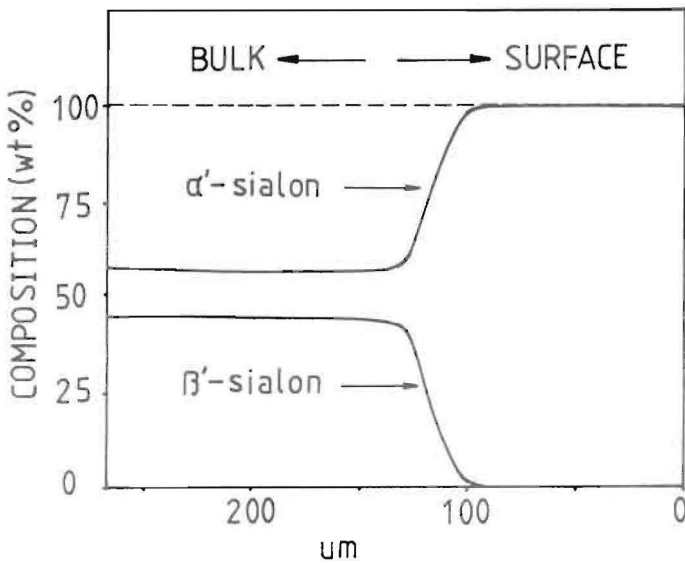


Fig. 5-20: The composition profile as a function of the depth from the surface in sample A4 determined by XRD.

that the surface layer consists of α' -sialon, as the only crystalline phase observed. The bulk exists of a two-phase mixture of α' - and β' -sialon. The yttrium-rich amorphous phase was not detectable by using XRD and therefore was not included in the figure. The thickness of the surface layer was approximately 100 μm , but varied with the temperature and time of the second step in the sintering schedule.

The effects of the nitrogen gas have been discussed before under the assumption of no solubility of nitrogen gas both in the liquid and solid phases, and of no reaction between the specimen and the nitrogen gas during sintering. In practice, however, nitrogen gas both trapped in pores in the specimen and from the surrounding gas is expected to dissolve into the liquid in spite of a low solubility. Probably this solubility is also increased by increasing nitrogen pressure. Besides, at high temperatures, the high pressure nitrogen gas is also expected to react with oxides or/and oxynitrides to form oxynitrides or/and nitrides, especially with the liquid phase remaining at grain boundaries. The presence of carbon vapour, which is generated from the graphite heating elements, will play a role to promote this nitridation process just like carbon powder used for carbothermal reductions. This nitrogen-rich liquid phase will subsequently react with the crystalline phases, the sialons. In the case of composite α' + β' -sialon ceramics, some β' -sialon as an oxygen-rich phase will be transferred to the more nitrogen-rich, α' -sialon phase. In the same way, the amount of nitrogen gas trapped in bulk pores of the specimens can be considerably reduced due to the dissolution into the liquid, and therefore the pores can be removed from the bulk. In this way the high pressure nitrogen gas provides not only an extra mechanical force but also a decrease of the free energy. Therefore the densification of sialon ceramics is expected to be improved significantly by using high gas pressure.

B. Powder bed & crucibles

As stated previously in chapter three, in the investigation described in this thesis three different types of powder beds were used: AlN, BN powders and a mixture consisting of 75 wt% Si_3N_4 , 20 wt% AlN and 5 wt% Y_2O_3 . The experimental results indicate that if sintering was conducted at a temperature below 1850°C under 0.5 MPa N_2 or below 1950°C under a nitrogen pressure of

10 MPa, the weight loss was approximately the same, normally less than 2 wt%. A variation of the composition of the surface layer was not detectable and no decomposition product was observed by using XRD and SEM with EDS, although different powder beds were used. However, if no powder bed was used during firing, the weight loss was considerably increased, sometimes above 10 wt%. Si, as a decomposition product, and also a lot of pores were always found in the surface layer of the specimens, under the sintering conditions mentioned above.

According to the literature [34-35], the powder bed for sintering of silicon nitride or oxynitride ceramics is required, since thermal decomposition reactions, described previously in this chapter, become operative at sintering temperatures. Thus a certain silicon partial pressure is supposed to be necessary to prevent the decomposition of silicon nitride even though a high nitrogen pressure is employed during firing. The powder bed used normally in the literature is a mixture consisting of silicon nitride and sintering additives, of which the composition, in most cases, was approximately the same as that of the compact, and this powder bed was thus proposed to provide a silicon partial pressure as well as other necessary vapours during firing.

However, in the present experiments, only one powder bed was able to provide silicon and other vapours. AlN or BN powders obviously cannot provide Si. The fact that the same results were observed here for the three different powder beds implies that the vapour phases provided by the powder beds were not necessary to suppress the thermal decompositions. However, the occurring of considerable weight loss and significant decomposition when no powder bed was applied shows the necessity of using powder bed. The results above therefore suggest that the vapour partial pressures are necessary to prevent the thermal decomposition and are provided by the compacts. The powder bed used is to keep silicon and other vapours around the compacts. In this way, the continuous thermal decompositions of nitrides and/or oxynitrides is suppressed. Besides, reactions between powder beds and compacts were hardly detectable and thus supposed to be negligible. The influence of the composition of powder beds therefore is considered to be not important.

Although two types of crucibles, made of graphite and BN respectively, were used, no significant influence of using different crucibles was observed,

probably due to the relative thick layer (normally not less than 1 cm) of powder beds present between the specimens and the crucibles.

C. Grain growth

Grain growth in α' -sialon ceramics starts simultaneously with formation and densification approximately at a temperature as low as 1360°C and continues as the temperature rises. Above 1600°C the grain growth progresses rapidly due to the Ostwald ripening process as discussed previously in chapter four.

During the presintering step, the grain growth proceeds rather slowly. Fig. 5-21 shows the SEM pictures of sample A4 sintered under various presintering conditions. The pictures show a very small variation of the grain size and morphology. Grain growth becomes much faster during the final sintering step. A higher sintering temperature or a longer holding time lead to a coarse-grained microstructure. The amount of liquid phase remaining at grain boundaries in the final stage is much smaller than during presintering. The smaller amount of the liquid leads to a faster grain growth [36-38] due to a shorter diffusion distance. Besides, a higher sintering temperature used at the final step results in a higher atom mobility.

D. Swelling phenomena

Swelling was observed in the sintering of sample L2 under a high nitrogen pressure and a very large hole was formed inside the specimen. These swell phenomena were also found in the case of β' -sialon [42], silicon nitride [43] and Alon [44] ceramics sintered by using gas pressure sintering, if a relatively large amount of sintering additive oxide(s) was used.

During sintering two types of pore diffusion are expected to occur. The first is pore diffusion out of samples, and the second is the merge of small pores to form large pores, i.e. pore growth. This pore growth generally results in a decrease of the density [37].

In the case of gas pressure sintering, the high pressure nitrogen reacted with the surface layer increasing thereby the liquid viscosity. Besides, the use of a high nitrogen pressure led to a faster densification of the surface layer than the bulk due to the temperature decreasing from the surface to inside, when the nitrogen

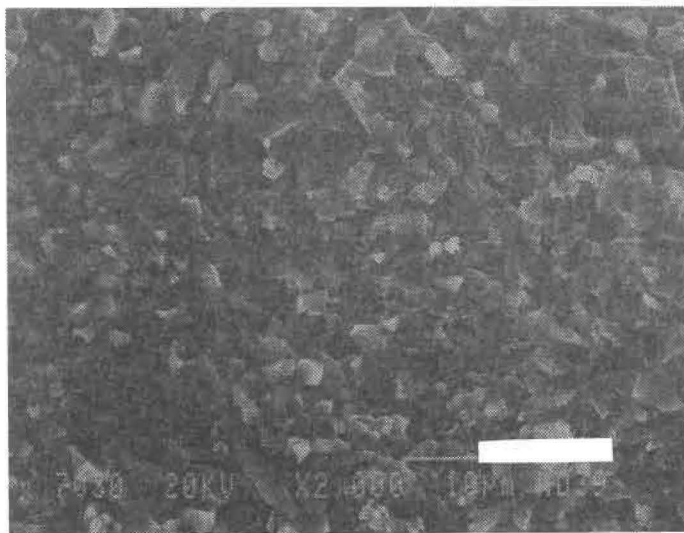


Fig. 5-21A: SEM micrograph of the fracture surface of $\alpha'+\beta'$ -sialon (A4) with presintering at 1700°C, 30 min. The bar is 10 μm .



Fig. 5-21B: SEM micrograph of the fracture surface of $\alpha'+\beta'$ -sialon (A4) with presintering at 1700°C, 90 min. The bar is 10 μm .

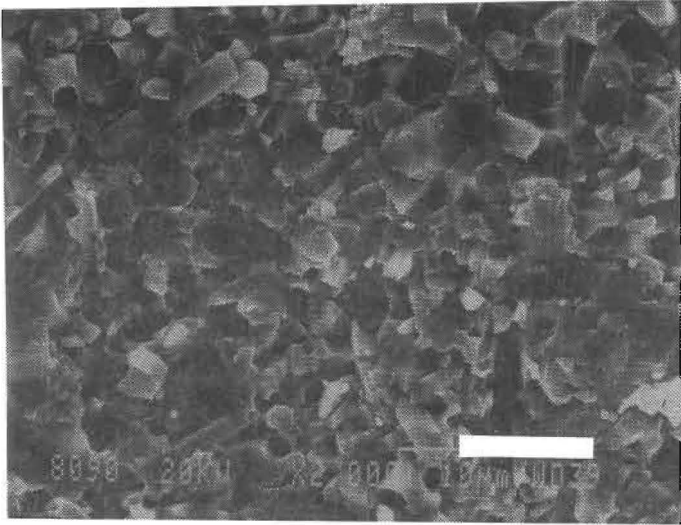


Fig. 5-21C: SEM micrograph of the fracture surface of $\alpha'+\beta'$ -sialon (A4) with presintering at 1800°C, 90 min. The bar is 10 μm .

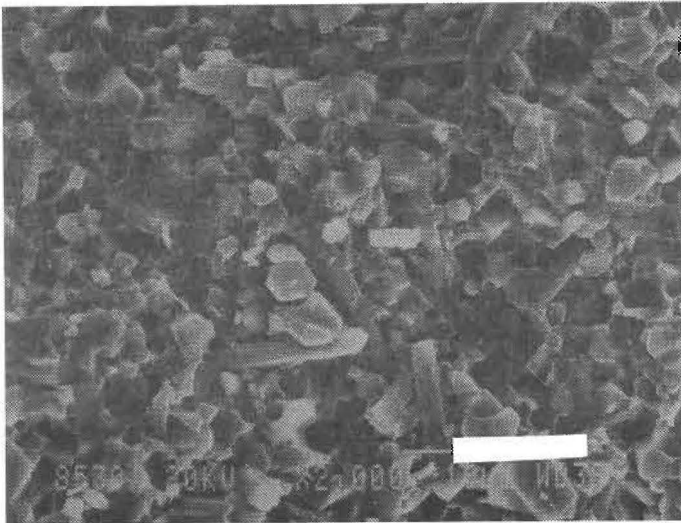


Fig. 5-21D: SEM micrograph of the fracture surface of $\alpha'+\beta'$ -sialon (A4) with presintering at 1850°C, 30 min. The bar is 10 μm .

pressure increased simultaneously with the temperature. The formation of this highly densified nitrogen rich surface layer is expected to be enhanced when a large amount of extra sintering additives is used. Thus the difficulty of pore diffusion out through the surface layer is enhanced. As a consequence, the merge of small pores results in an increase of the pore volume, which subsequently results in swelling.

The pore growth during the final stage of sintering is also proposed to explain the decrease of the density of the final products with the increase of the amount of sintering oxides added into the starting mixtures as shown in Fig. 5-5.

5-5. DISCUSSION AND SUMMARY

The experimental results have demonstrated that the high nitrogen pressure applied during the final sintering step promoted a significant densification only in the case of a closed pore condition achieved previously. However, the build up of the high pressure inside pores opposed to the further densification.

It is seen that to optimise the sintering parameters a statistical evaluation method is very useful. In the present investigation, the optimum presintering parameters are found to be approximately 1800°C for about 60 min under a low nitrogen pressure of 0.5 MPa, followed by a final sintering step at 1900°C for 30 min under 10 MPa N₂. The similar optimum presintering parameters observed imply that a similar sintering process occurred in these samples, although the compositions of the starting mixtures and the final products were considerably different. The liquid phase formed during sintering plays a predominant role for the densification. The constituents of the liquid phase were gradually consumed to form sialons and most of the liquid phase was absorbed as the sintering temperature reached about 1800°C. Only a very minor amount of highly viscous liquid phase remained. It is therefore proposed that a liquid phase with similar composition and properties remains at the final densification stage. Although the starting composition of these samples varied considerably, at later stage of densification the liquid phase remaining could be very similar. This possibly explains the similar optimum presintering parameters obtained for various samples.

The classical gas pressure sintering model of equation (9) assumes that the

gas is inert and does not react with the matrix. In that case the high pressure gas employed solely provides a mechanical force, which exerts its effect on the densification only by reducing the size of the closed pores. However, the experimental results show that the nitrogen gas either trapped in pores or surrounding the specimens will react with the liquid phase at grain boundaries by replacing oxygen. This nitrogen-rich liquid phase will further react with the β' -sialon to give nitrogen-rich phase, α' -sialon as proposed in literature [39]. In this way the composition of the gas trapped in pores becomes richer in oxygen which might influence the gas diffusion out through the matrix. A recent investigation [40] reported that pores existing in sintered silicon nitride based ceramics can be filled by liquid under high nitrogen pressures and also suggested that pores can be eliminated due to diffusion of the trapped gas through the matrix. Therefore, fully dense nitrogen ceramics can be obtained by sintering under high nitrogen pressures.

The reaction between the high pressure nitrogen and the surface layer of the specimens and the fast densification in the surface layer compared to the bulk hampers gas diffusion out of the pores. When a large amount of liquid phase existed, swelling of the specimens was observed.

It also should be noted that the grain growth in the presintering step was not very significant but it became much faster during the final sintering step. This is probably due to the decrease of the amount of the liquid phase and also higher temperatures.

In summary, fully dense α' -sialon ceramics can be obtained by gas pressure sintering with optimized sintering parameters. With two sintering steps, it is suggested that a certain minimum densification level should be reached in the presintering step, since the high sintering temperature favours not only densification but grain coarsening as well.

5-6. REFERENCES

1. Ziegler, G., Heinrich, J. and Wötting, G., J. Mater. Sci., 1987,22,3041.
2. Moulson, A.J., J. Mater. Sci., 1979,14,1017.
3. Ziegler, G., Z. Werkstofftech., 1983,14,147.

4. Giachello, A., Martinengo, P.C., Tommasini, G. and Popper, P.,
J. Mater. Sci., 1979,14,2825.
5. Mangels, J.A. and Tennenhouse, G.J., Am. Ceram. Soc. Bull.,
1980,59,1216.
6. Loehman, R.E and Rowcliffe, J., J. Am. Ceram. Soc., 1980,63,144.
7. Terwilliger, G.R. and Lange, F.F., J. Amer Ceram. Soc., 1974,57,25.
8. Lange, F.F., Int. Metal. Rev., 1980,1,1.
9. Bowen, L.J., Weston, R.J, Carruthers, T.G. and Brook, R.J.,
J. Mater. Sci., 1978,13,341.
10. Ziegler, G. and Wötting, G., Int. J. High-tech. Ceram., 1985,1,31.
11. Mitomo, M., J. Mater. Sci., 1976,11,1103.
12. Rowcliffe, D.J. and Jorgensen, P.J., Rept. NSF/RA-770-443,
NTIS-PB28-0.653, 1977.
13. Priest, H.F., Priest, G.L. and Gazza, G.E.,
J. Am. Ceram. Soc., 1977,60,80.
14. Wötting, G. and Ziegler, G., Sprechsaal 1986,119,265.
15. Prochazka, S. and Greskovich, C.D.,
Rept. AMMRC-TR78-32, SRD-77-178,1978.
16. Greskovich, C., Progress in Nitrogen Ceramics, ed. Riley, F.L., 1983,
p283, NATO ASI Series E65, Martinus Nijhoff, The Hague.
17. Singhal, S.C., Ceram. Int., 1976,2,123.
18. Hirosaki, N. and Okada, A., Advanced Ceram. Mater., 1988,3,515.
19. Greskovich, C. and Prochazka, S., J. Am. Ceram. Soc., 1981,64,C-96.
20. Messier, D.R. and Deguire, E.J., J. Am. Ceram. Soc., 1984,67,602.
21. Hirosaki, N. and Okada, A., Yogyo-kyokaiishi, 1987,95,235.
22. Wötting, G. and Ziegler, G., High-tech Ceramics, ed. Vincenzini, P., 1987,
p983, Elsevier Applied Science Publishers B.V., Amsterdam.
23. Larker, H.T., Progress in Nitrogen Ceramics, ed. Riley, F.L., 1983, p717,
NATO ASI Series E65, Martinus Nijhoff, The Hague.
24. Coble, R.L., Sintering – Theory and Practice, eds. Kolar, D., et al.,
1982, p145.
25. Kwon, O.H. and Messing, G.L., Sintering '85, eds. Kuczynski, G.C., et al.,
1986, p165.

26. Kessel, H.U. and Engel, W.P., *cfi/Ber. DKG*, 1989,66,227.
27. Wötting, G. and Ziegler, G., *cfi/Ber. DKG*, 1988,65,471.
28. Hausner, H., Science of Ceramics 12, ed. Vincenzini, P., 1983, p229.
29. Greskovich, C.D. and Palm, J.A., AMMRC TR80-46, SRD-80-111, 1980.
30. Greskovich, C., *J. Am. Ceram. Soc.*, 1981,64,725.
31. Hurst, J.B. and Millard, M.L., *J. Am. Ceram. Soc.*, 1985,68,C-178.
32. Box, G.E.P., Hunter, W.G. and Hunter, J.S., Statistics for Experimenters, Wiley, NY, 1978.
33. Cochran, W. and Cox, G., Experimental Designs, Wiley, New York, 1957, p42-47.
34. Sun, W.Y., Wu, F.Y. and Yan, D.S., *Mater. Lett.*, 1987,6,11.
35. Xu, J. and Sheng, X.M., Proc. Conf. on Microstructure and Properties of Ceramic Materials, ed. Yen, T.S., 1983,pp518.
36. Voorhees, P.W. and Glicksman, M.E., *Metall. Trans. A*, 1984,15A,1081.
37. German, R.G., Liquid Phase Sintering, 1985, Plenum Press, New York.
38. Kingery, W.D., Bowen, H.K. and Uhlmann, D.R., Introduction to Ceramics, 1976, John Wiley & Sons.
39. Jack, K.H., Progress in Nitrogen Ceramics, ed. Riley, F.L., 1983, p45, NATO ASI Series E65, Martinus Nijhoff, The Hague.
40. Kang, S.J.L., Greil, P., Mitomo, M. and Moon, J.H., *J. Am. Ceram. Soc.*, 1989,72,1169.
41. Loehman, R.E., *J. Non-cryst. Solids*, 1983,56,123.
42. Kokmeijer, E., Ph.D., Thesis, Eindhoven University of Technology, 1990, Eindhoven, the Netherlands.
43. Huang, Z.K., personal communication, 1989.
44. Willems, H.X., personal communication, 1990.

CHAPTER SIX, MICROSTRUCTURE AND PROPERTIES OF α' -SIALON CERAMICS

6-1. INTRODUCTION

In the previous chapters, we have discussed the material composition and the fabrication conditions. We have seen that fully dense α' - and composite $\alpha'+\beta'$ -sialon ceramics can be obtained routinely by using gas pressure sintering with optimized process parameters. In this chapter, we will first present the microstructure analysis results, and then the mechanical properties of α' - and mixed $\alpha'+\beta'$ -sialons. The oxidation resistance of α' - and mixed $\alpha'+\beta'$ -sialon ceramics at various conditions will be presented at the end.

In general, the attention here was concentrated mainly on the α' - and mixed $\alpha'+\beta'$ -sialons which were fully densified at 1800°C for 60 min under 0.5 MPa N₂ followed by 1900°C for 30 min under 10 MPa N₂. It means that samples A5, A6, B2 and C2 are not included in this chapter, and for L2 only the microstructure analysis is discussed.

6-2. MICROSTRUCTURE

A. Neutron diffraction analysis

The crystal structure of yttrium containing α' -sialon was studied by using neutron powder diffraction [1-2]. This technique is very sensitive for the light elements like oxygen and nitrogen. The purpose of this work is to refine the structure parameters and to obtain the site distribution of the elements aluminium and oxygen in the α' -sialon lattice.

The Rietveld refinement technique [3-4] was applied. This method has found wide spread application in the structure determination of compounds which are not available as single crystals. In Rietveld analysis the parameters in a structural model, plus necessary instrumental parameters, are adjusted in a computer calculation until the least-squares best fit is obtained between the entire calculated and observed powder diffraction patterns. The neutron diffraction analysis was performed at ECN in Petten. A range of scattering angle $5^\circ < 2\theta <$

155° was investigated 0.1° in step with a count time of 2 min per step. The total scan time was approximately 50 hr. The structure refinements were conducted approximately the same as that given by Izumi et al. for X-ray diffraction refinements [5-6].

The α' -sialon powder was prepared from the mixture of A2 (see Table 3-3). The starting composition was $Y_{0.5}Si_{9.75}Al_{2.25}O_{0.75}N_{15.25}$. After mixing and/or milling, the mixture was fired in a gas pressure furnace first at 1800°C for 60 min under a nitrogen pressure of 0.5 MPa and then followed at 1900°C for 30 min under 10 MPa N_2 , which is the same as for the preparation of dense sialon ceramics described previously. The powder obtained contains Y- α' -sialon as the only crystalline phase detectable.

For the Rietveld refinement, space group P31c was assumed for α' -sialons and the Y^{3+} content was treated as a free parameter. Table 6-1 lists the final R factors (fitting criteria) and structure parameters for the Y- α' -sialon phase. The definition of the R factors in the table is identical with that described by Young and Wiles [7]. Rather low R factors were obtained and the full powder pattern calculated from the refined parameters matched the experimental result very well as demonstrated in Fig. 6-1. In this figure, the observed data are indicated by dots and the calculated ones by the solid line overlying them. The short vertical lines mark the positions of possible Bragg reflections and the lower dots show the differences between the observed and calculated intensities. The results above clearly support the model that α' -sialon has the expanded α -silicon nitride structure built up of $[(Si,Al)(O,N)_4]$ tetrahedra with yttrium ions partially occupying the interstitial sites [8-10]. No significant preference of the oxygen distribution was observed, thus a random distribution of the oxygen is assumed. However, the distribution of aluminium is seen to have a significant preference for the position [0.1631, 0.24889, 0.0093] with atom ratio Si:Al = 3.9:2.1, instead of the statistic ratio 4.9:1.1, whereas silicon prefers the position [0.5051, 0.0771, 0.2192] with Si:Al = 5.9:0.1. This is contrary to that was proposed [5].

Table 6-2 shows the Y-(N,O) and (Si,Al)-(O,N) tetrahedral bond lengths calculated by using UNICS III [11]. Each yttrium ion is coordinated by seven nitrogen or oxygen cations [5-6]. The Y-(O,N) bond lengths range from 0.2326 nm to 0.2662 nm, with the shortest bond parallel to the c-direction.

Table 6-1: Results of Rietveld Refinements for Y- α' -sialon with composition $Y_{0.34}Si_{9.8}Al_{2.2}O_{0.85}N_{15.15}$ *

Atom	Position	X	Y	Z	Occupation
Y	2b	1/3	2/3	0.242(8)	0.34(2)
Si(1)	6c	0.505(1)	0.077(1)	0.219(2)	5.9(3)
Al(1)	6c	0.505(1)	0.077(1)	0.219(2)	0.1(3)
Si(2)	6c	0.163(1)	0.2488(9)	0.009(3)	3.9(3)
Al(2)	6c	0.163(1)	0.2488(9)	0.009(3)	2.1(3)
N(1)	2a	0	0	0	1.9062
O(1)	2a	0	0	0	0.0938
N(2)	2b	1/3	2/3	0.651(2)	1.9062
O(2)	2b	1/3	2/3	0.651(2)	0.0938
N(3)	6c	0.3422(5)	-0.0480(4)	-0.014(2)	5.7186
O(3)	6c	0.3422(5)	-0.0480(4)	-0.014(2)	0.2814
N(4)	6c	0.3155(5)	0.3175(5)	0.253(2)	5.7186
O(4)	6c	0.3155(5)	0.3175(5)	0.253(2)	0.3814
R_p		= 2.71%	Temp. Factor: 0.36(4) \AA^2		
R_{wp}		= 3.54%	a = 7.8154(2) \AA		
χ^2		= 3.73	c = 5.6963(1) \AA		
R_b		= 2.20%			

*: Standard deviations of last significant figures in parentheses.

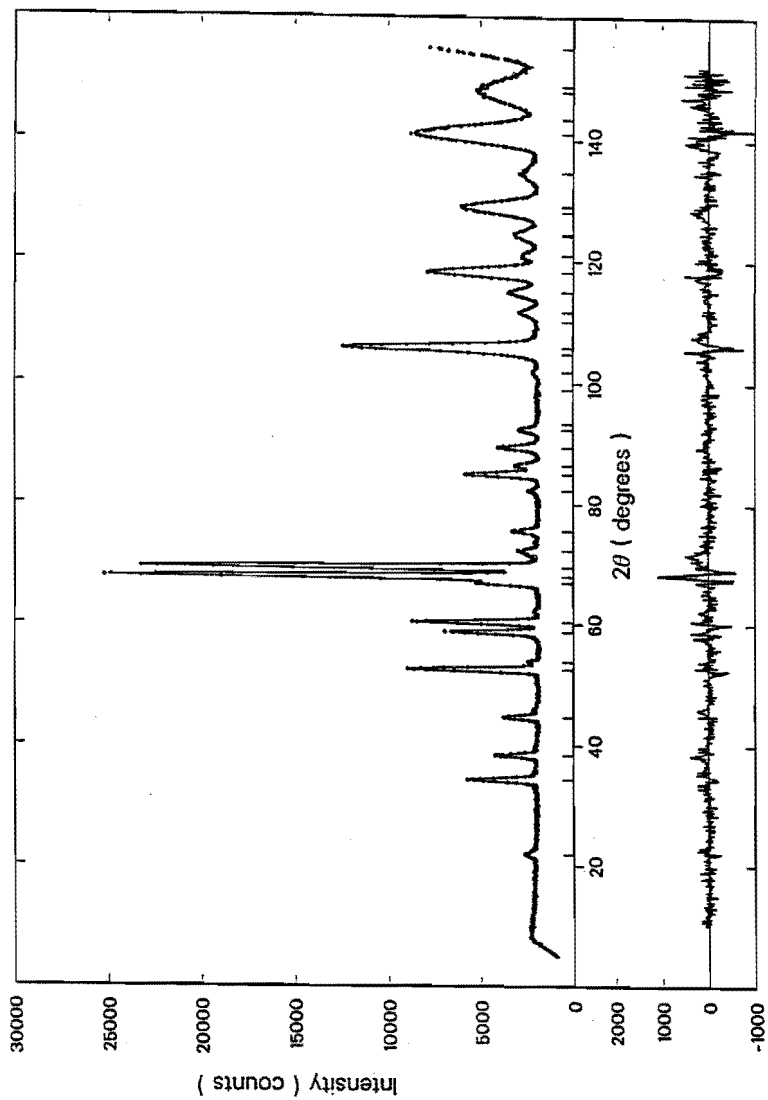


Fig. 6-1: Rietveld refinement patterns for the Y- α' -sialon.

The length of the (Si,Al)-(O,N) bond is in the range from 0.1712 nm to 0.1796 nm, with an average length of 0.1752 nm. It is larger than the mean Si-N length in α -silicon nitride 0.174 nm, but smaller than the mean Al-N length in aluminium nitride 0.187 nm. Also it is seen that the mean length of the (Si,Al)₁-(O,N) bonds, 0.1757 nm, is slightly longer than 0.1746 nm of (Si,Al)₂-(O,N) bonds. It is explained in corresponding to the distribution preference of the element aluminium.

The observed composition of the α' -sialon powder is $Y_{0.34}Si_{9.8}Al_{2.2}O_{0.85}N_{15.15}$, which is slightly different from that calculated from the starting mixtures. The yttrium content is smaller, whereas the oxygen content is slightly higher. Also the lattice parameters observed here, $a = 0.78154(2)$ nm and $c = 0.56963(1)$ nm, are slightly smaller than $0.782927(7)$ nm and $0.570757(6)$ nm of $Y_{0.3}Si_{9.75}Al_{2.25}O_{0.75}N_{15.25}$, respectively [5-6]. The results above clearly support the idea that only a part of yttrium was incorporated into the crystal lattice of the α' -sialon, and another part is consumed in the formation of the oxynitride amorphous phase which is necessary for the formation of the α' -sialon.

B. X-ray diffraction analysis

Table 6-3 gives a comparison of the products observed in the final products and calculated according to the phase diagrams [12-15] (see Figs. 2-10 and 3-3) for various samples. It shows that there was only one crystalline phase of α' -sialon in the final products in the case of samples A1, A2, A7 and A8, while α' - and β' -sialon phases were observed for others. It is seen that composite α' + β' -sialons were obtained in the case of A3, instead of monolithic α' -sialon as expected according to the phase diagram. Also there was no β -silicon nitride phase observed in A4, but β' -sialon. The same result was seen in the case of sample A5 (see Fig. 4-5). Also the table shows that for all composite α' + β' -sialon ceramics the ratios of β' : α' were found to be higher than that calculated. For instance for sample A9 the ratio of β' : α' was expected to be about 50:50 but 60:40 is observed. Besides, the lattice parameters both of α' and β' -sialons were observed to be smaller than expected. For example, in the case of A2, the lattice parameters of the α' -sialon determined by using both XRD and neutron diffraction are smaller than those calculated according to the composition. The data was given in the previous

paragraph.

The experimental results above imply that there was a shift of the composition of the crystalline phases for both monolithic α' -sialon and composite α' + β' -sialon ceramics. However, there was only a small weight loss (less than 2 wt%) during sintering as discussed in the previous chapters, and thus the overall composition of the specimens is proposed to have not changed. The shift of the composition of the crystalline phase(s) is explained to occur in two ways. The first is that in the final products there is some amorphous material that consumed a part of yttria and aluminium nitride. The second is due to the existence of the oxygen impurity in the starting mixtures.

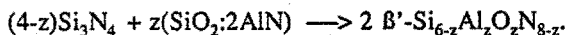
Table 6-3: A comparison of the final product compositions observed and calculated from the phase diagram.

No.	Observed		Calculated	
	Phases	Ratio of α' : β'	Phases	Ratio of α' : β'
A1	α'	100:0	α'	100:0
A2	α'	100:0	α'	100:0
A3	α' , β'	90:10	α'	100:0
A4	α' , β'	75:25	α' , β -SN*	80:20
A7	α'	100:0	α'	100:0
A8	α'	100:0	α'	100:0
A9	α' , β'	40:60	α' , β'	50:50
A10	α' , β'	35:65	α' , β'	50:50

*: β -SN is β -silicon nitride

In chapter three we have stated that there was oxygen impurity content of 1.57 wt% present in the silicon nitride starting powder (LC-12, Starck), but it was not counted into the composition of the starting mixtures. The oxygen impurity in general is assumed to be in the form of SiO_2 , and thus approximately 3.0 wt% SiO_2 was present in the silicon nitride starting powder. At high temperatures SiO_2 was proposed to react with silicon nitride and aluminium nitride to form β' -sialons

in the following reactions [16]:



A similar conclusion can apply for the oxygen impurity in the aluminium nitride starting powder.

As a consequence, β' -sialon was obtained in the case of sample A4. In a similar way a shift of the composition towards to the oxygen rich side in the phase diagram (see Figs. 2-10 and 3-3) resulted in the formation of mixed α' + β' -sialons in sample A3. In all samples, the crystalline phase composition was observed to shift towards to a higher oxygen content in the lattices than indicated in the phase diagrams, along with the overall decrease of the crystal lattice parameters of α' - and β' -sialons.

C. OM and SEM study

For the investigation of the microstructure of α' - and composite α' + β' -sialon ceramics, the method of plasma etching was used to prepare the specimens. The fundamental of the plasma etching was described in great detail in literature [17] and therefore is not repeated here. The etching experiments were conducted by using Plasma Enhanced CVD under the following conditions: temperature 300°C, pressure 600 mtorr, 300 kHz, 100 W, a gas of mixed CF_4/O_2 (5 vol%) with a flow rate of 200 ml/min for 10 minutes. Other etching methods were tried as well, by using a mixture of acids: 6 vol% HF, 5 vol% H_2O_2 , 1 vol% HNO_3 and 5 vol% H_2O , and molten KOH or KOH/ KNO_3 , which are normally used for etching silicon nitride and β' -sialon ceramics. However, neither acid nor alkaline etching for times up to one hour was successful.

Fig. 6-2 is the SEM fractograph of α' -sialon of sample A2, densified by using gas pressure sintering. α' -sialon has a homogeneous microstructure and appears with equi-axed grains approximately with a mean grain size 4 μm . Fig. 6-3 shows the SEM fractograph of the composite α' + β' -sialon A4. It is seen that in this composite the α' -phase has the same micromorphology as in monolithic α' -sialon ceramics, whereas the mean grain size is about 3 μm . β' -sialons possess needle or fibre-like grains, the ratio of length to width, in general, was about 7. For β' -sialon grains, an average length of about 14 μm and a width of about 2 μm were observed.

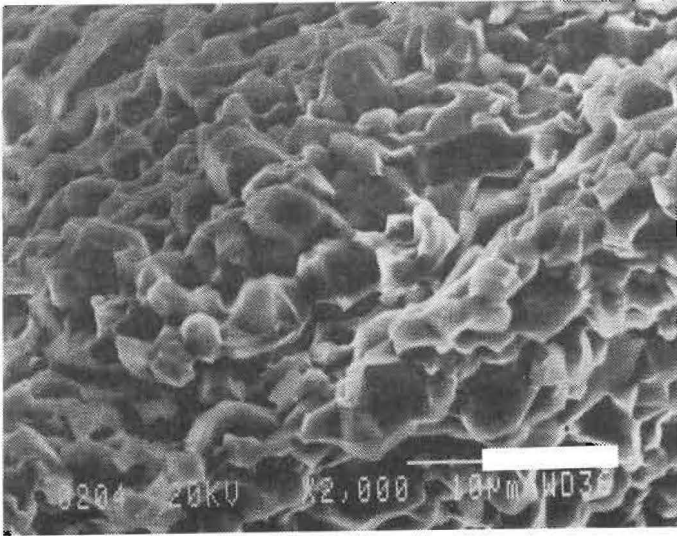


Fig. 6-2: SEM micrograph of the fracture surface of sample A2. The bar is 10 μm .

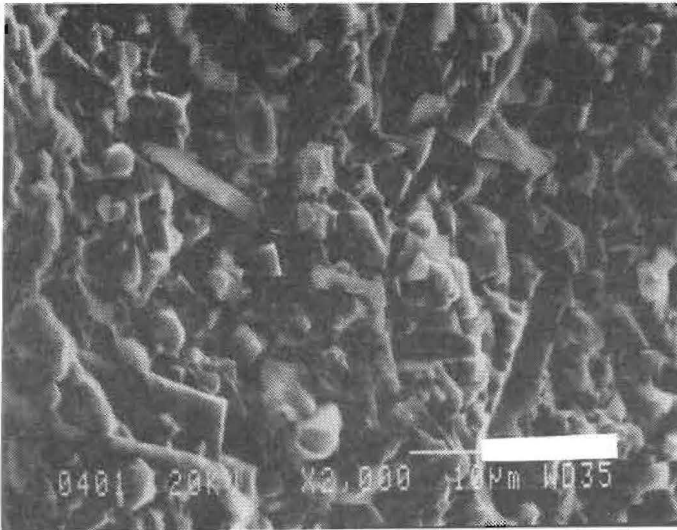


Fig. 6-3: SEM micrograph of the fracture surface of sample A4. The bar is 10 μm .

The influence of the addition of alumina on the microstructure was studied as well. The micromorphology and the grain size in the case of monolithic α' -sialon samples A7 and A8 were approximately the same as those in A2. The increasing amount of alumina in the mixtures is expected to increase the amount and to decrease the viscosity of the liquid phase during sintering. The former consequently results in an increase of the diffusion distance, and thus the grain growth during sintering is expected to be slower. In contrast, the latter enhances the diffusivity of the atoms or/and ions through the liquid phase resulting in faster grain growth. The experimental results therefore imply two possible explanations. The first is that the influence of both the amount and the viscosity of the liquid were very small, which seems not very likely according to the literature [18-19]. The second is that the influences of the increasing amount and the decreasing viscosity of the liquid phase approximately compensate each other, so that a small influence is observed experimentally.

For composite $\alpha'+\beta'$ -sialon ceramics the increasing amount of alumina in the starting mixtures was seen to result in a decrease of the ratio of the length to width (see Fig. 6-4). The mean ratio was observed to be approximately 4, and the length 10 μm and width 2.5 μm .

Fig. 6-5 shows the intergranular fracture surface of sample L2. The mean grain size of the α' -sialon phase is only about 2 μm . The addition of the extra sintering additive La_2O_3 into the mixture results in a fine-grained microstructure. The La_2O_3 is expected not to be incorporated into the crystal lattice [8-10] and thus solely to increase the amount of the liquid. Therefore, the presence of La_2O_3 in the mixture L2 suppressed the grain growth due to the longer diffusion distance.

D. TEM study

For a close study of the grain boundaries, TEM studies with EDS analysis and selected area electron diffraction technique were done.

Fig. 6-6 shows the TEM photomicrograph of α' -sialon ceramics in the case of sample A2. The selected-area electron diffraction technique was used to determine the crystallinity and EDS was used to analyse the composition of the different phases. The amount of secondary phase was calculated from TEM photomicrographes. There is only one crystalline phase viz. α' -sialon and

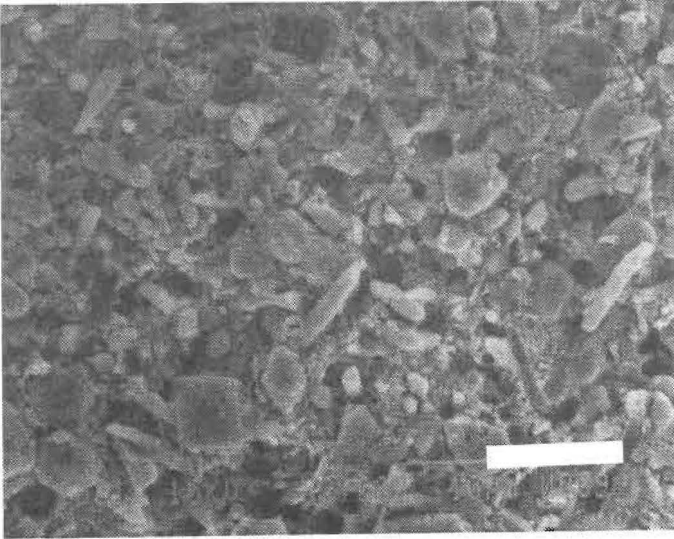


Fig. 6-4: SEM photograph of mixed α' + β' -sialon of A8 with alumina powder used in the starting mixture. The bar is 10 μm .

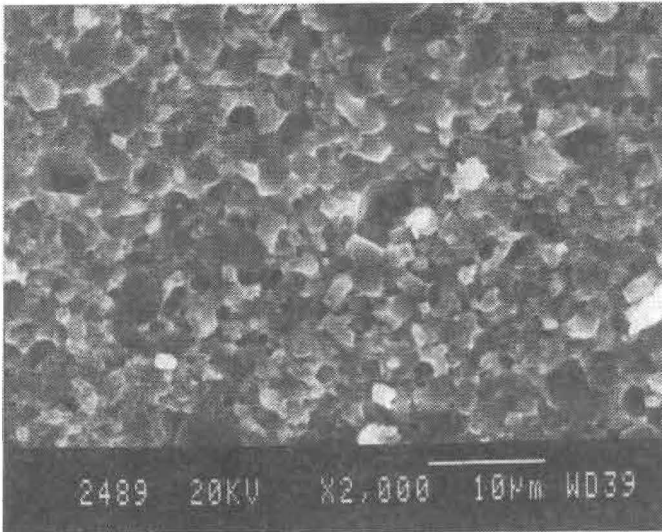


Fig. 6-5: SEM micrograph of the fracture surface of sample L2 with addition of La_2O_3 to the starting mixture. The bar is 10 μm .



Fig. 6-6: TEM micrograph and the composition of the grain boundary amorphous phase determined by EDS in sample A2.

approximately 8.5 vol% of an amorphous phase, which remains not only at the intersections of three grains (triple junctions) and four grains, but also at the intersections of two grains. That means that all crystal grains are covered with a thin film of amorphous material. In sample A2 the amount of yttria used is much smaller than the upper solubility limit, thus theoretically all yttria should have been incorporated into the lattice of the α' -structure. The present investigation shows, however, that it is very difficult to complete the formation of the α' -phase. The EDS analysis indicates that the amorphous phase at grain boundaries is rich in yttrium with an atom ratio Si:Al:Y = 1:0.6:0.8. This is different from the average content in the overall composition of the sample, Si:Al:Y = 1.00:0.23:0.05. Also it is seen that the aluminium content at grain boundary phase is higher than that in the overall composition. The results obtained above are in good agreement with the literature [13, 20-22].

Fig. 6-7, as an example, shows a TEM photomicrograph of composite α' + β' -sialon ceramics of sample A4. Similar to monolithic α' -sialons, a glassy phase is always observed at grain boundaries although the amount of grain boundary phase, about 3.5 vol% in A4, is much smaller. Furthermore, the composition of the glassy phase, in atom ratio Si:Al:Y = 1:0.5:0.8, in comparison with the overall composition Si:Al:Y = 1.00:0.10:0.02, appears quite similar to that in α' -sialon ceramics, even though the amount of yttria is much smaller than the solubility limit in the α' -phase. Only a very thin glass film is present at the intersections of two grains. This is also the case at the intersections of three and four grains junctions. It is seen that the amount of glassy phase at grain boundaries is increased with the increased amount of alumina in the mixtures, even though the alumina theoretically is totally soluble into the structures of α' - and β' -sialons. No clear explanation is available at the moment.

Fig. 6-8 shows the TEM micrograph and the grain boundary composition of sample L2. We have seen earlier that the addition of the extra sintering additive La_2O_3 into the mixture of L2 suppresses the grain growth during sintering. It is also seen that the addition of La_2O_3 promotes the incorporation of yttria into the lattice of the α' -phase as expected and the composition of the grain boundary phase was changed to Si:Al:Y:La = 1:0.4:0.6:1.2, whereas the overall composition is Si:Al:Y:La = 1.00:0.23:0.05:0.003. However, the amount of glass phase at grain

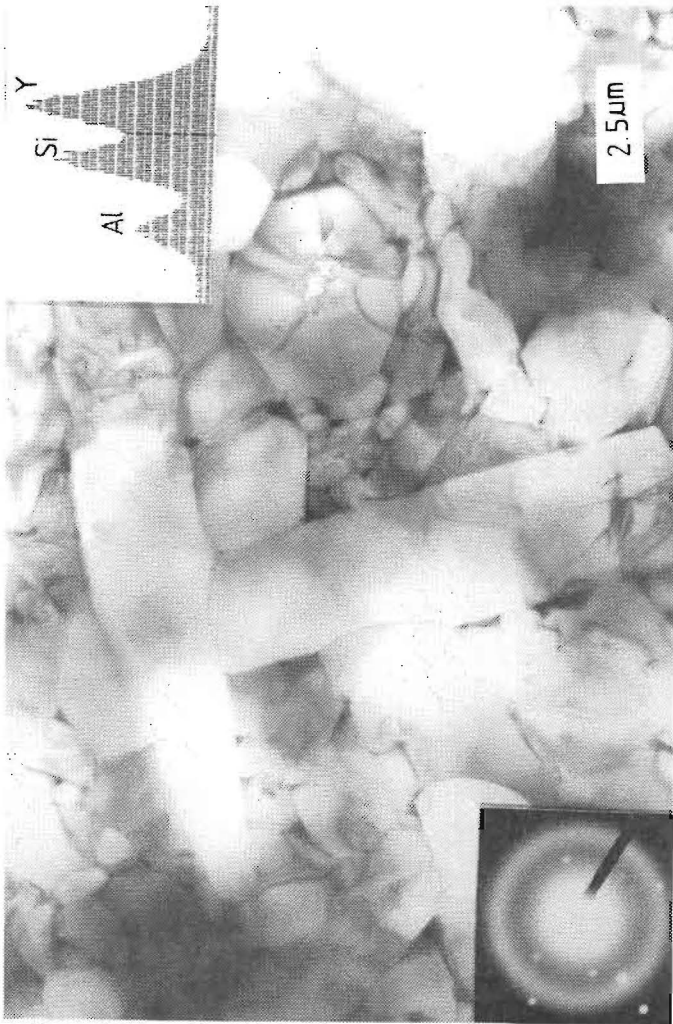


Fig. 6-7: TEM micrograph and the composition of the grain boundary amorphous phase determined by EDS in sample A4.

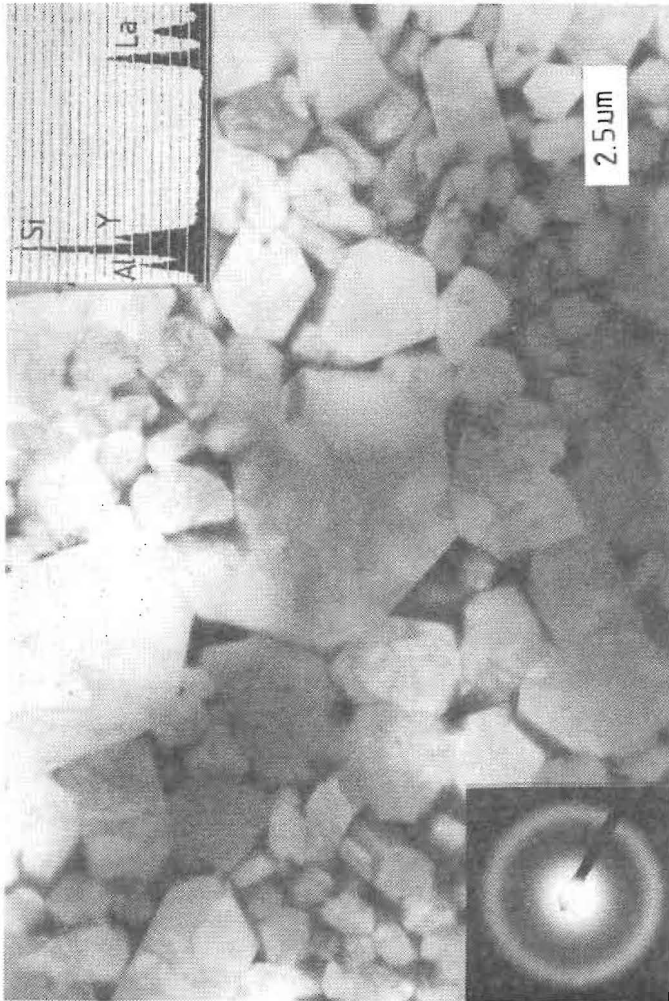


Fig. 6-8: TEM micrograph and the composition of the grain boundary amorphous phase determined by EDS in sample L2.

boundaries is greatly increased to about 16 vol%, almost doubled compared with A2. Due to the large size of the La^{3+} ion, the addition of La_2O_3 solely contributes to increase the amount of amorphous phase remaining at grain boundaries after cooling. Thus it is expected that a reduction of the amount of La_2O_3 will consequently result in a decrease of the amount of the grain boundary phase.

It is also seen that the addition of La_2O_3 to the mixture resulted in the formation of crystal defects inside of the α' -sialon crystal as demonstrated in Fig. 6-9. Such crystal defects were hardly observed when no La_2O_3 was added into the starting mixtures. Some possible explanations are as follows. The first is that a small amount of La^{3+} entered the α' -sialon lattice and thus the crystal lattice was greatly distorted due to the large size of La^{3+} ions. The second is the merge of two grains during sintering and amorphous phase was trapped in crystal grains. Further detailed investigation is needed.

The TEM observations, together with the EDS analysis and the selected-area electron diffraction technique, reveals that in all of our α' - and mixed $\alpha'+\beta'$ -sialon ceramics, a small amount of yttrium-rich amorphous phase is always present at grain boundaries.

6-3. MECHANICAL PROPERTIES

A. Vickers hardness and fracture toughness

Table 6-4 gives the Vickers hardness (HV0.5) and fracture toughness (K_{IC}) of α' - and composite $\alpha'+\beta'$ -sialon ceramics. The details of the methods used were described previously in chapter three. Not less than 15 measurements were conducted for each sample.

The highest Vickers hardness achieved is 21.0 GPa in monolithic α' -sialon ceramics in the case of sample A1. The hardness is seen to decrease in the order of $A1 > A2 > A3 > A4$, which corresponds to an increase of the amount of mixed $\text{Y}_2\text{O}_3:9\text{AlN}$ in the starting mixtures (see Table 3-3). This rises the amount of the amorphous phase at grain boundaries of the final products. Although the composition of the final products varies from monolithic α' -sialon in the case of samples A1 and A2, to composite $\alpha'+\beta'$ -sialon in A3 and A4, no discontinuous change of the hardness was observed (see Fig. 6-10). Therefore the decrease of the

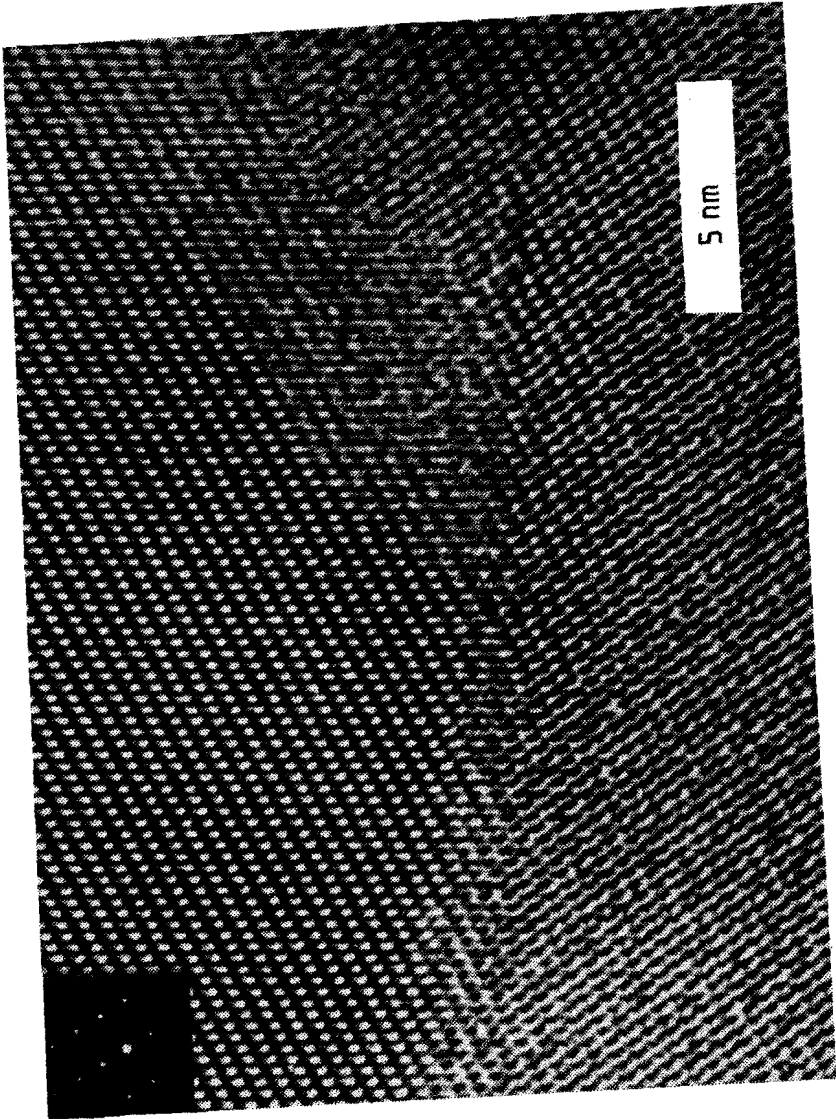


Fig. 6-9: High resolution TEM micrograph of sample L2, showing the crystal structure defect.

Vickers hardness is explained due to the increased amount of the yttrium-rich amorphous phase at grain boundaries of the final products. In case of monolithic α' -sialon ceramics the hardness is also seen to decrease in the order of A2 > A7 > A8, in correspondence to the increasing amount of alumina in the starting mixtures. Similar results apply to the composite $\alpha'+\beta'$ -sialons of samples A4, A9, and A10. However, the microstructure observation showed that the increase of the amount of alumina in the starting mixtures hardly influenced the amount and the composition of the grain boundary phase, thus the decrease of the hardness is proposed to correspond to the increased amount of aluminium in the lattice of the α' -sialon crystalline phase.

Table 6-4: Vickers Hardness and Fracture Toughness of α' - and $\alpha'+\beta'$ -sialon ceramics

No.	HV(0.5N) (GPa)	K_{IC} (MPa.m ^{1/2})
A1 (α')	21.0 ± 1.6	5.7 ± 0.5
A2 (α')	19.6 ± 0.6	5.6 ± 0.3
A3 (α',β')	19.0 ± 2.0	5.6 ± 0.4
A4 (α',β')	17.2 ± 1.5	6.0 ± 0.7
A7 (α')	19.4 ± 0.8	5.4 ± 0.4
A8 (α')	18.9 ± 1.0	5.3 ± 0.3
A9 (α',β')	16.8 ± 1.0	5.8 ± 0.6
A10(α',β')	14.5 ± 1.0	5.7 ± 0.7

In contrast to the Vickers hardness, Table 6-4 indicates that the fracture toughness (K_{IC}) is almost constant for samples A1, A2 and A3. The highest fracture toughness is 6.0 MPa.m^{1/2} in composite $\alpha'+\beta'$ -sialon ceramics in the case of sample A4. It is seen in Fig. 6-10 that the fracture toughness shows a discontinuity as the composition of the final products changes from monolithic α' -

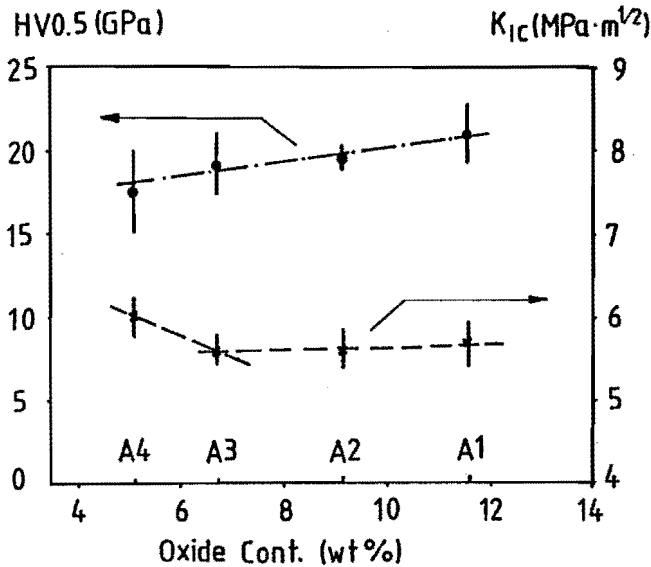


Fig. 6-10: Vickers hardness and fracture toughness of α' - and composite $\alpha'+\beta'$ -sialon ceramics.

sialon to composite $\alpha'+\beta'$ -sialons. We propose that this is due to the presence of elongated grains of the β' -sialon phase. Besides, the fracture toughness of the composite $\alpha'+\beta'$ -sialons decreases with increasing amount of alumina, which correlates with the decrease of the aspect ratio of the β' -grains. A similar variation of the Vickers hardness and fracture toughness of α' - and composite $\alpha'+\beta'$ -sialons has been observed by other investigators [23-26].

B. Biaxial bending strength

The bending strength of α' -sialon and composite $\alpha'+\beta'$ -sialon ceramics measured with the "ball-on-ring" test are given in Table 6-5. The measurement was conducted at ambient temperature (about 20°C) under 0.1 MPa nitrogen at a dew point of -35°C (relative humidity 1%). A crosshead speed of 85 mm/h was used. The specimens were 20 mm in diameter and 1 mm in thickness. The surface roughness was approximately 0.2 μm . Not less than 12 measurements were performed for each sample.

In general, composite $\alpha'+\beta'$ -sialon ceramics show higher bending strength than monolithic α' -sialon ceramics. The highest bending strength achieved is 734

± 55 MPa in the case of sample A4, and the lowest is 517 ± 36 MPa in sample A1. It is seen that the bending strength of composite α' + β' -sialon ceramics decreases in the order of $A4 > A9 > A10$, corresponding to the increase of the amount of alumina used in the starting mixtures. This is not observed in the case of monolithic α' -sialon ceramics.

Microstructure observation reveals that both monolithic α' -sialon and composite α' + β' -sialon ceramics show a typical intergranular fracture surface along with cracks propagated at grain boundaries. For composite α' + β' -sialon ceramics, the elongated grains of β' -sialon phase thus have increased the fracture surface and consequently increased the strength.

The bending strength observed here are biaxial strength data. As shown by Dortmans and de With the three-point bending strength is about 75 % of the biaxial strength [52], the precise percentage dependent on specimen size. Thus the highest three-point bending strength is calculated to be 550 MPa and the lowest 388 MPa. A comparison with literature will be given later in the discussion section.

Table 6-5: Biaxial Bending Strength of α' - and α' + β' -sialons

Sample No.	Density (g/cm ³)	σ_{bi} (MPa)
A1	3.33	517 ± 36
A2	3.29	519 ± 55
A3	3.28	—
A4	3.23	734 ± 36
A7	3.28	570 ± 40
A8	3.27	553 ± 101
A9	3.22	680 ± 50
A10	3.23	598 ± 73

C. Wear resistance

Some preliminary experiments on wear resistance were conducted as well. The experiments were performed with a pin-on-plate apparatus. The details of the instrument parameters are given by Kokmeijer [28]. The experimental condition was selected as follows: 4 N load, pin frequency of 1 Hz, a tracklength of 10 mm, 70 hr under 0.1 MPa nitrogen at room temperature, with steel pins. The specimens used are the same as for biaxial bending strength measurement.

Figs. 6-11 and 6-12 show the friction coefficients and the wear depths as a function of wear time for both monolithic α' -sialon (sample A1) and composite $\alpha'+\beta'$ -sialons (sample A9), respectively. The friction coefficient for α' -sialon ceramics was seen to be about 0.5, whereas for composite $\alpha'+\beta'$ -sialons 0.4 was obtained, both are constant in time. After 65 hr wear, wear depths were 0.033 mm and 0.020 mm for α' -sialon and composite $\alpha'+\beta'$ -sialons, respectively. The composite $\alpha'+\beta'$ -sialon shows a better wear resistance than the monolithic α' -sialon ceramics. Microstructure observation indicates that polishing wear is the only process during these 65 hr wear experiments, no fatigue and/or abrasive wear was observed for both monolithic α' -sialon and composite $\alpha'+\beta'$ -sialon ceramics.

In comparison with the wear resistance of β' -sialon reported by Kokmeijer [28], it is seen that the α' -sialon has a relatively poor wear resistance (with a wear depth of 0.033 mm after 65 hr wear), whereas the composite $\alpha'+\beta'$ -sialon (a wear depth of 0.020 mm) shows a similar wear resistance as the β' -sialon (a wear depth of 0.015 mm). For a better understanding a further study is necessary.

D. Discussion

Although the mechanical properties of α' -sialon ceramics have been widely investigated in comparison with other properties, only a limited understanding has been achieved [10]. The mechanical properties of α' -sialon ceramics, including the $\alpha'+\beta'$ -sialon composites, reported in literature can be summarized as follows [20,21,23-26, 29-39]. The Vickers hardness is in the range of 16.2 to 19.6 GPa, K_{IC} varies from 3.7 to 7.0 MPa·m^{1/2}, and the bending strength (three or four-point bending strength) from 256 to 900 MPa, but an extremely high bending strength of 1300 MPa was also reported [35]. The large variation of the mechanical properties is probably due to different material compositions, process conditions

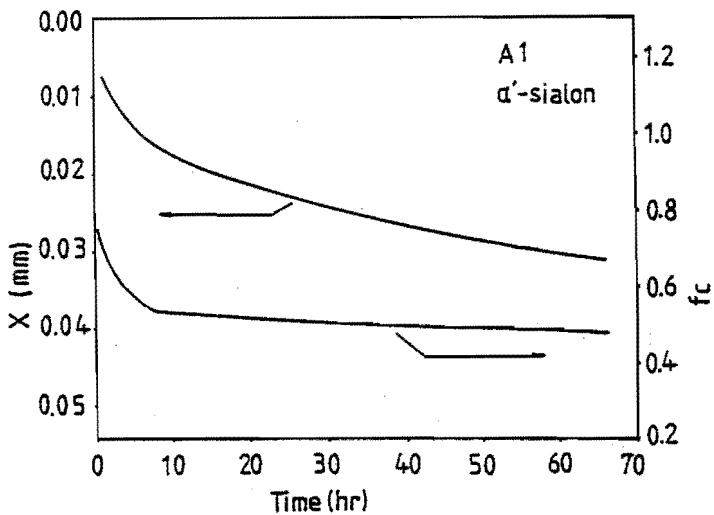


Fig. 6-11: Wear and friction coefficient as a function of time for α' -sialon (sample A1) (4 N, 1 Hz).

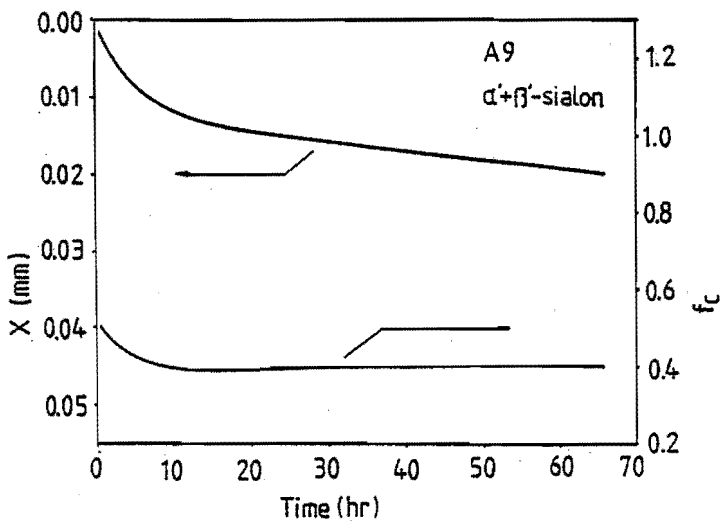


Fig. 6-12: Wear and Friction coefficient as a function of time for mixed $\alpha'+\beta'$ -sialons (sample A9) (4 N, 1 Hz).

and testing methods used in various research groups. Thus a comparison of the mechanical properties observed in the present work with those reported in literature is very difficult. However, an analysis of the literature data reveals that the most reproducible mechanical properties would be as follows: the Vickers hardness is 17.0 to 19.6 GPa, the K_{IC} between 4.5 and 6.0 MPa $m^{1/2}$ and the three or four-point bending strength between 450 and 580 MPa. The mechanical properties above were obtained in α' - and composite $\alpha'+\beta'$ -sialon ceramics. It is seen that the mechanical properties of α' - and composite $\alpha'+\beta'$ -sialons achieved in the present investigation are very good compared to the literature data.

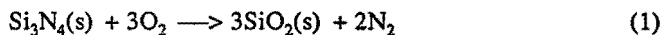
Kokmeijer [28] reported a strength of 490 MPa for the β' -sialon. The β' -sialon ceramics were made under approximately the same GPS condition and the biaxial bending strength was measured under the same test condition as for the α' - and $\alpha'+\beta'$ -sialons in the present investigation. It is seen that the composite $\alpha'+\beta'$ -sialons have the highest biaxial bending strength with a maximum of 730 MPa, in comparison with monolithic α' - and β' -sialon ceramics. This enhancement of the biaxial bending strength can be explained in terms of the microstructure of mixed $\alpha'+\beta'$ -sialon ceramics. Firstly, it is seen that the pull-out of β' -grains, with high aspect ratio, results in increasing the fracture energy, and also the mean grain size of the α' -phase in the case of mixed $\alpha'+\beta'$ -sialons is somewhat smaller than in monolithic α' -sialon ceramics. Secondly, the amount of the amorphous phase remaining at grain boundaries is much smaller in mixed $\alpha'+\beta'$ -sialons than that in monolithic sialon ceramics, which probably results in a reduced the size of the flaws.

6-4. OXIDATION RESISTANCE

A. Thermodynamic aspects

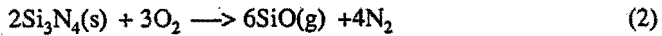
The thermodynamics of the oxidation of silicon nitride has been well documented in literature and can be briefly summarized as follows.

Silicon nitride and oxynitride, including sialons, can have two distinctive types of chemical reactions [40-42], just like silicon and silicon carbide [43-44]. At high partial oxygen pressures, a passive oxidation takes place:



and a dense silica layer (mainly amorphous) is subsequently formed, which inhibits

further oxidation, and thus provides excellent oxidation resistance, e.g. at 1600 K this layer is stable at partial oxygen pressures above $8 \cdot 10^{-4}$ bar. However, at lower partial oxygen pressures so-called active oxidation occurs, and volatile SiO is formed according to the reactions:



As opposed to passive oxidation, active oxidation causes a continuous loss of material from the surface due to the formation of silicon monoxide gas.

Although the oxidation of sialons is a more intricate process than silicon nitride, in principle the thermodynamic fundamentals above are still applicable.

Extensive investigations of the oxidation of various types of silicon nitride ceramics have shown that passive oxidation follows a parabolic relationship of the form $X^2 = kt$, where X is the oxide layer thickness or the weight gain at time t, and k is the temperature dependent rate constant [45-48]. The rate of this reaction is controlled by the oxygen diffusion through the oxide layer and thus is greatly influenced by the composition, crystallinity and quantity of the intergranular phase.

Investigations of B'-sialon ceramics [49-50] also showed the occurrence of passive oxidation in air. For B'-sialon with yttria as sintering aid an oxidation mechanism was proposed [50-51]; oxygen ions diffuse through the silica layer; yttrium ions diffuse to the surface and can form different phases in the Y-Si-Al-O-N system, but eventually yttria precipitates are formed. Sialon decomposes and forms mullite and silicon oxynitride. The resulting nitrogen diffuses to the surface and forms craters in the oxide layer.

Up to now only little is known of the oxidation of α' - and mixed α' +B'-sialons [10] in comparison with silicon nitride and B'-sialon ceramics. The following section is concentrated on our work of the oxidation resistance of α' - and α' +B'-sialons.

B. Oxidation behaviour of α' - and α' +B'-sialons

Figs. 6-13 and 6-14 give the experimental results of the oxidation resistance of samples A1 to A4, and the experiments were performed at 1450°C under an atmosphere of air for 50 hr in a NETZSCH simultaneous thermal analyzer.

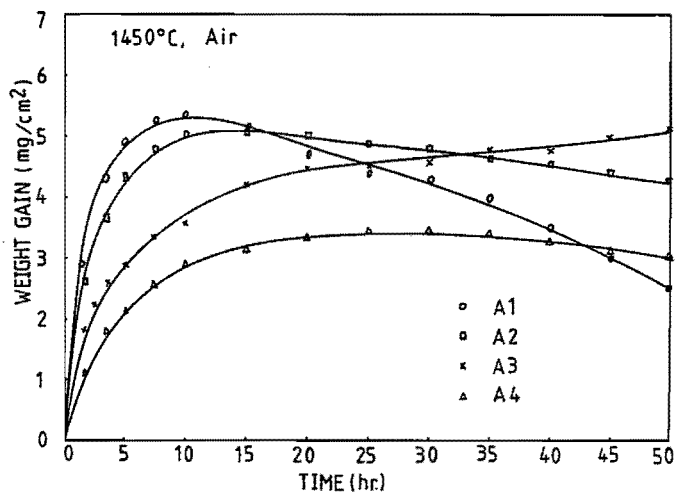


Fig. 6-13: Weight gain per unit area as a function of time.

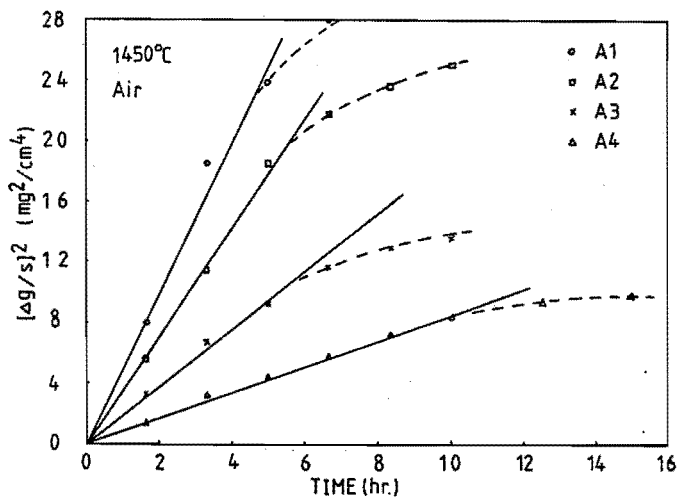


Fig. 6-14: Parabolic plot of data given in Figure 6-13.

Fig. 6-13 shows that the weight increased very rapidly in the first 10 hr for all samples. After 5 hr the weight gain per unit surface area was seen to be 4.9, 4.2, 2.8 and 2.1 mg/cm² for samples A1 to A4, respectively. It is also seen that the weight gain increases in the array of A1 to A4, in correspondence to the increasing amount of Y₂O₃:9AlN in the starting mixtures. The further oxidation is seen to result in a weight decrease in the case of samples A1 and A2 and a small change of the overall weight in A4, while a slow continuous weight increase was observed in A3. Fig. 6-14 indicates that in the early stage the oxidation of both α' - and α' + β' -sialons follows the parabolic relationships. As the oxidation progresses, the rate decreases strongly.

The oxidation behaviour of the α' -sialon ceramics of samples A7 and A8 is quite similar to that of A2 as demonstrated in Fig. 6-15. A rapid weight increase was observed for all three samples in the beginning until about 10 hr, followed by a weight decrease for longer oxidation times. A decrease of the weight gain from A2 to A7, and then to A8 correlates with the increase of the alumina content in the starting mixtures. Also an irregular weight increase occurred between 20 to 25 hr during the oxidation experiment in the case of sample A7.

For composite α' + β' -sialons the results of the oxidation experiments in samples A9 and A10 are compared with those for A4 in Fig. 6-16. The rapid weight increase in the beginning can be described by the parabolic oxidation relationship for all three samples. However, a slow weight increase followed as the experiment continued after 10 hr. For sample A10 another rapid weight increase was seen to occur after 25 hr and a small irregularity in the weight change also appeared in the case of sample A9. It should be noted here that in contrast to monolithic α' -sialon ceramics, the increase of the alumina content in the starting mixtures led to a deterioration of the oxidation resistance of composite α' + β' -sialon ceramics.

For all samples above, an oxide layer formed on the surface of the specimens during oxidation. There were always a lot of pores at the interface between the oxide layer and the bulk. The oxide layer consists mainly of amorphous silicate and a small amount of α -cristoballite (α -SiO₂), mullite (3Al₂O₃:2SiO₂) and sometimes also B-phase (Y₂SiAlO₅N). Fig. 6-17A, as an

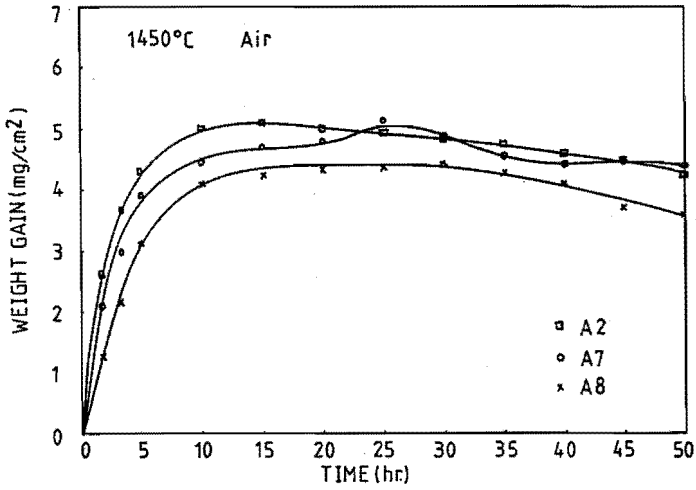


Fig. 6-15: Weight gain per unit area as a function of time for α' -sialons.

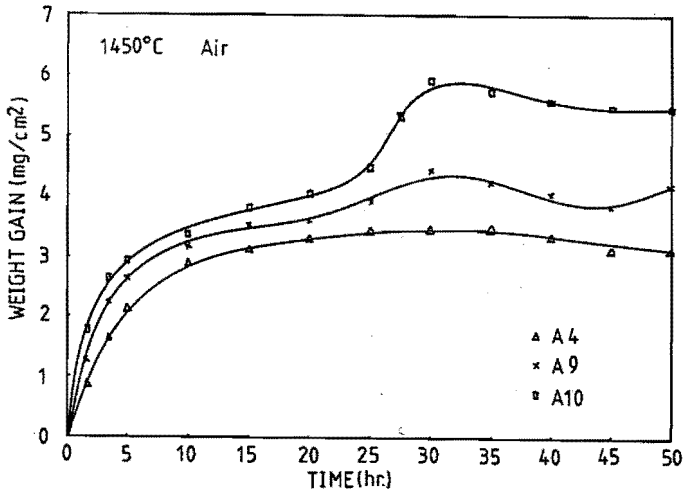


Fig. 6-16: Weight gain per unit area as a function of time for mixed α' + β' -sialons.

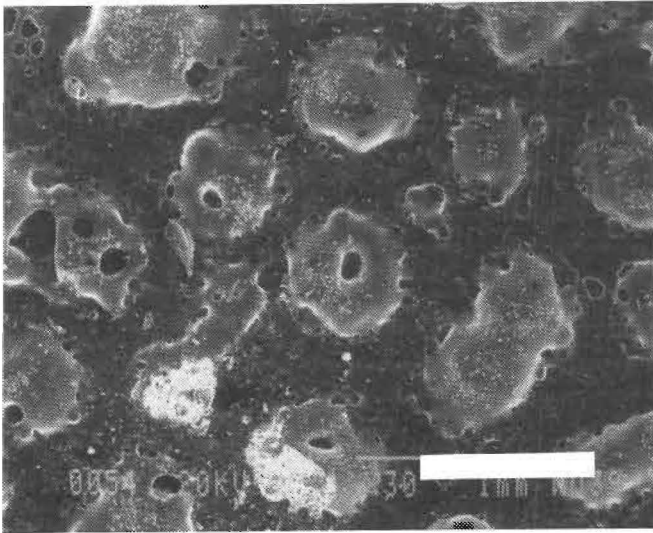


Fig. 6-17A: Surface texture of scale after oxidation in Air for 50 hr for mixed α' + β' -sialons (sample A4). The bar is 1 mm.

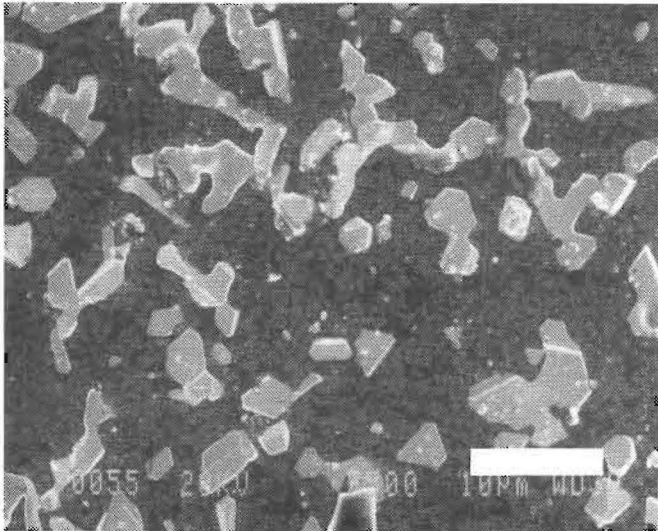


Fig. 6-17B: α -cristoballite formed on the oxidized surface layer. The bar is 50 μm .

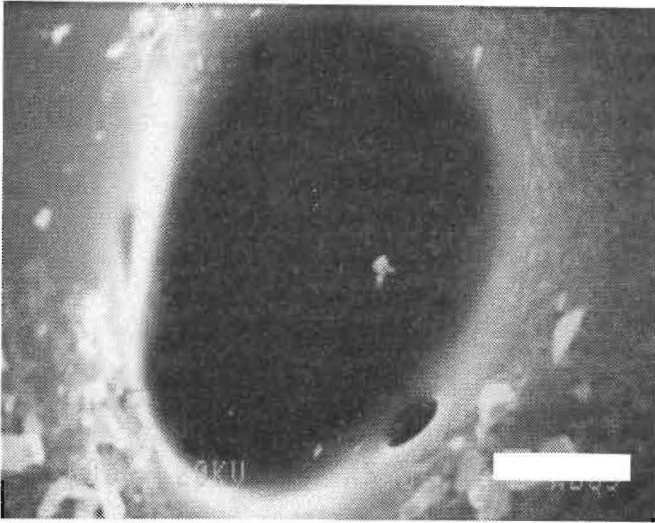


Fig. 6-17C: Surface eruption site for gas bubble. The bar is 50 μm .

Table 6-6: Parabolic Oxidation Constants (k) and Products in α' - and $\alpha'+\beta'$ -sialon after oxidation at 1450°C under 0.1 MPa air

Sample No.	Composition	k ($\times 10^{-8}$ $\text{mg}^2/\text{cm}^4 \cdot \text{min}^2$)	Products*
A1	α'	14.8	A, α , M
A2	α'	10.2	A, α , M, B
A3	$\alpha'+\beta'$	4.7	A, α , M
A4	$\alpha'+\beta'$	2.3	A, α
A7	α'	8.5	A, α , M
A8	α'	5.3	A, α , M
A9	$\alpha'+\beta'$	3.6	A, α
A10	$\alpha'+\beta'$	5.0	A, α

*: A: amorphous silicate, α : α -cristoballite,
 M: $\text{Y}_2\text{O}_3\text{Si}_3\text{N}_4$, B: $\text{Y}_2\text{SiAlO}_5\text{N}$

example, shows the micrograph of the oxide layer in the case of sample A4. The α -cristoballite can be seen in Fig. 6-17B and a lot of craters are seen to form in the surface (see Fig. 6-17C).

Table 6-6 summarizes the oxidation products observed and also gives the parabolic rate constants for various samples obtained in the initial period. It is seen that, in general, the composite α' + β' -sialons show a better oxidation resistance. This correlates quite well with the observation that their microstructures show only a minor amount of intergranular phase as discussed previously.

C. Oxidation mechanism of α' -sialon ceramics

The parabolic oxidation behaviour of α' - and α' + β' -sialons can be explained as passive oxidation, in which a dense oxide layer consisting of mainly amorphous phase is formed and the further oxidation of the bulk is controlled by oxygen diffusion through this oxide layer. Since the atom mobility in a viscous liquid phase is faster than in a crystalline phase, the oxidation occurs along with the grain boundaries, thus the oxidation resistance is significantly influenced by the amount and the composition of the glassy grain boundaries phase. It explains that the oxidation resistance deteriorates with increasing amount of the amorphous phase at grain boundaries.

During the passive oxidation, the protective oxide layer formed and its thickness increases as the oxidation proceeds. If the oxygen diffusion control is still applicable, just like in silicon nitride and β' -sialon ceramics, the concentration of oxygen (or partial oxygen pressure) at the interface between the oxide layer and the bulk declines due to the increase of the diffusion resistance as demonstrated in Fig. 6-18. When the partial oxygen pressure decreases below the critical value, active oxidation is expected to occur (see Fig. 6-19). After reaching the critical thickness, active oxidation is predominant (see Fig. 6-20). The active oxidation leads to a loss of mass due to the formation of silicon monoxide via the reactions 6-3 and 6-4, and thus an overall weight decrease is expected. In the present experiments it is seen that the active oxidation occurred after approximately of 5 to 10 hr, depending on the rate of the formation of the protective oxide layer.

If the oxide layer breaks due to some incidents, such as release of a large

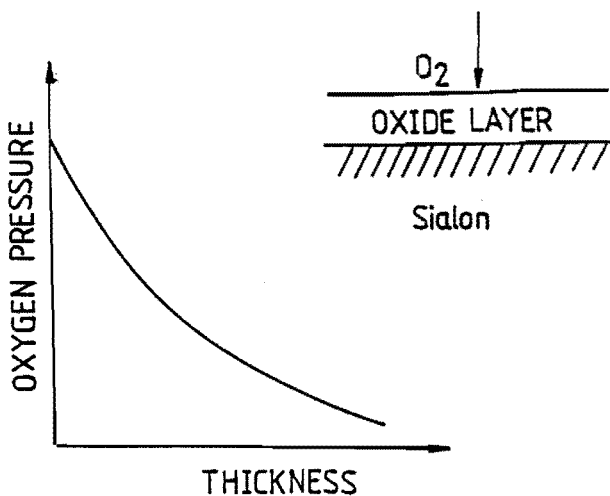


Fig. 6-18: Schematic drawing of the oxygen activity as a function of the thickness of the oxidized layer.

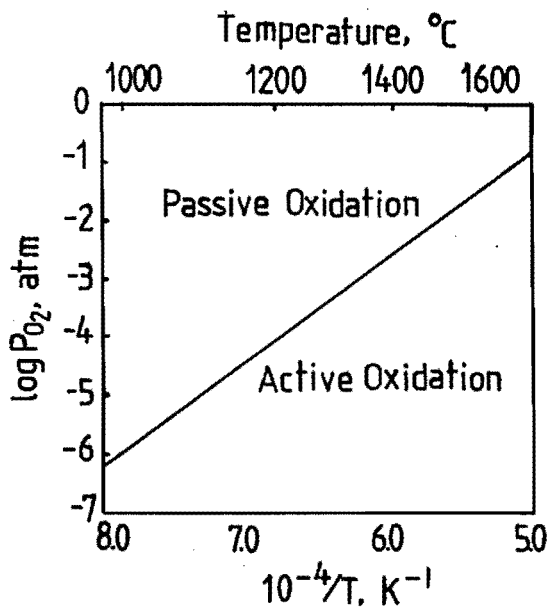


Fig. 6-19: Calculated regions for active and passive oxidation of Si_3N_4 in terms of oxygen partial pressure and temperature [40,41].

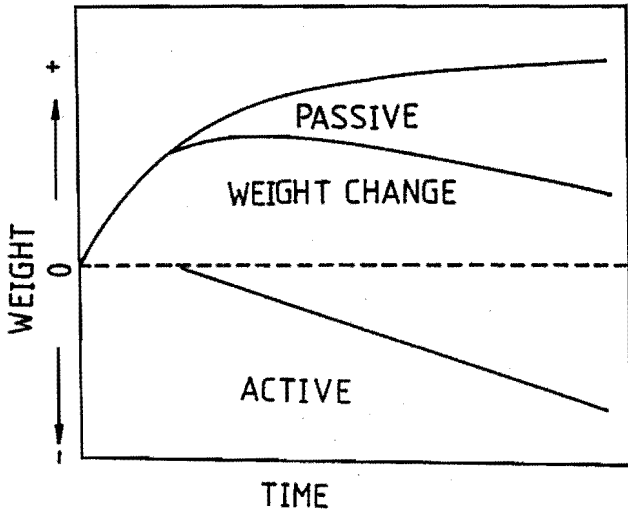


Fig. 6-20: Schematic drawing of the weight change as a function of time.

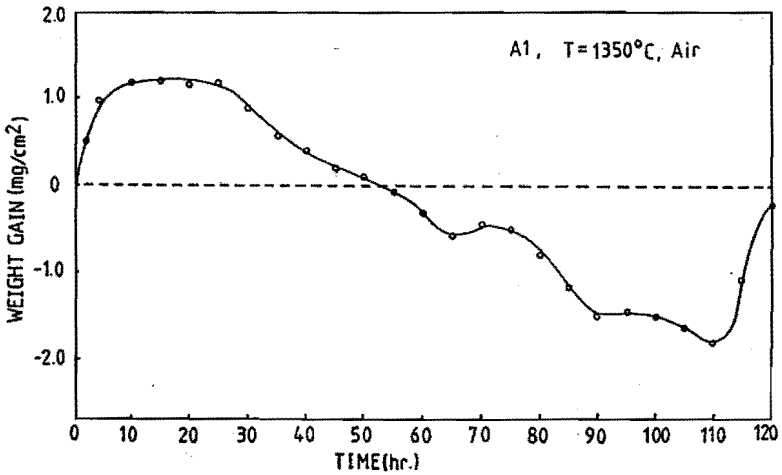


Fig. 6-21: Weight gain per unit area as a function of time for α' -sialon (A1).

nitrogen gas bulb, then a part of or all the "inner" surface of the bulk is accessible to the oxygen gas, and as a consequence the passive oxidation restarts and results in an irregular weight increase as demonstrated in Fig. 6-21. Such oxidation process is also seen in the case of samples A7, A9 and A10 in Figs. 6-15 and 6-16.

For a better understanding, further investigation is needed.

D. Influence of temperature & oxygen partial pressure

Fig. 6-22 gives the oxidation behaviour of the α' -sialon sample A2 under an atmosphere of air at temperatures in the range from 1250°C to 1450°C. The oxidation behaviour at the early stage follows the parabolic relationship due to the predominance of the passive oxidation. It is also seen that the weight gain increases with rising temperatures. However, the further oxidation exhibits some irregularity as we have observed previously in the case of A7, A9 and A10.

The influence of the partial oxygen pressure on the oxidation of the α' -sialon sample A2 is given in Fig. 6-23. The partial oxygen pressure, in a gas mixture of oxygen and nitrogen, increases from 0.21, 0.5, 0.75 to 1.0 bar at the temperature of 1350°C. In all cases, the oxidation behaviour follows the parabolic relationship in the beginning. However, it is quickly overlapped by a weight decrease, especially under a high partial oxygen pressure. As the oxidation goes on, a continuous weight loss is observed. The higher partial oxygen pressure results in a higher weight decrease. No explanation is available yet.

E. Powder oxidation

Fig. 6-24 shows the oxidation behaviour of the α' -sialon powder. The α' -sialon powder is the same as for the neutron diffraction analysis. The surface area of the powder is 1.2 m²/g, as determined by N₂ adsorption (BET). The oxidation experiments were conducted under the same condition as for dense α' - and /or α' + β' -sialons. It is seen that the oxidation proceeds very rapidly during the first period of about one hour and then follows with a very slow weight increase. It is seen that the α' -sialon powder shows a better oxidation resistance than the dense products (see Figs. 6-22, 23 etc.) and does not follow the parabolic relationship at all. A significant difference is that after a short period of weight increase, the weight remains almost unchanged in following experiments.

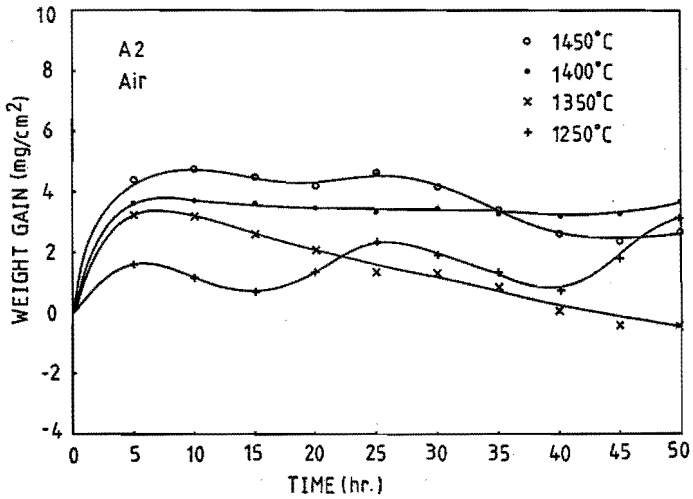


Fig. 6-22: Weight gain per unit area as a function of time for α' -sialon (A2), at various temperatures in air.

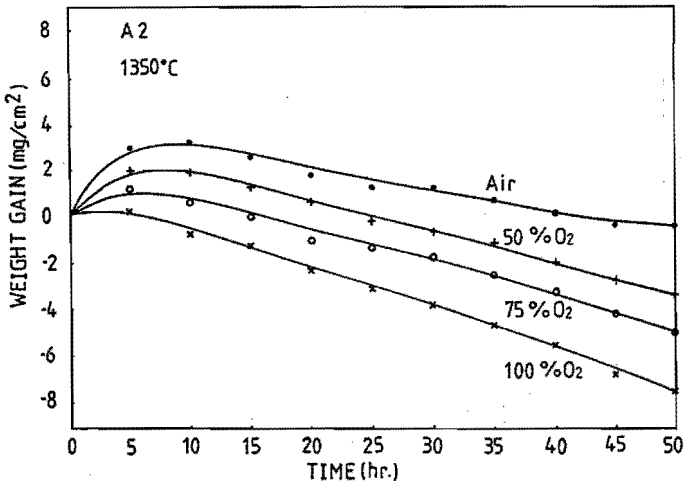


Fig. 6-23: Weight gain per unit area as a function of time for α' -sialon (A2), at 1350 °C under various partial oxygen pressures.

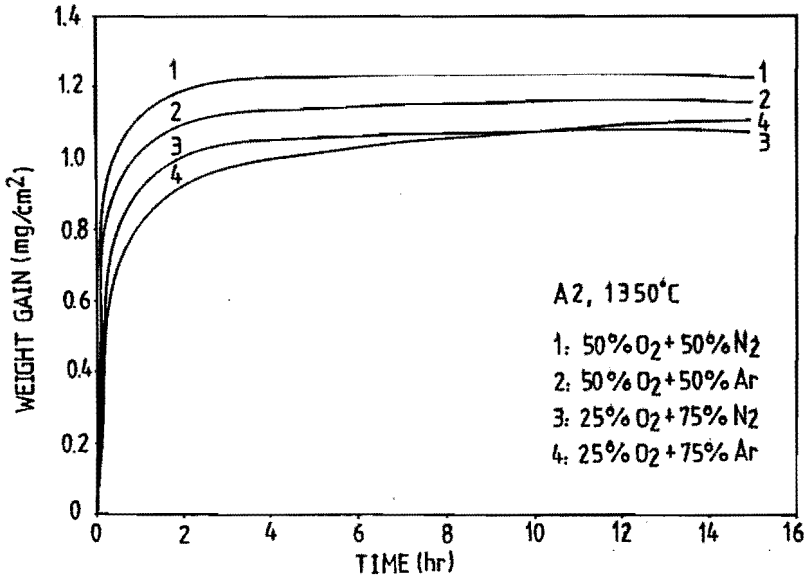


Fig. 6-24: Weight gain per unit area as a function of time for α' -sialon powder (A2), at 1350 °C under various partial oxygen pressures.

This figure also shows the influence of the partial oxygen pressure on the oxidation of the α' -sialon powder. The higher partial oxygen pressure results in a larger weight increase in the early stage. Also nitrogen enhances the oxidation in comparison with argon, probably due to the oxygen and water vapour present in nitrogen (P_{O_2} is about 10^{-4} bar). The overall oxidation behaviour at those four different conditions is approximately the same.

The difference of the oxidation of α' -sialons between dense compacts and powder is probably due to the influence of the amorphous phase. It remains at grain boundaries in the case of dense materials, while for powder the amorphous phase mainly covers the crystalline phase. As a consequence the oxidation of α' -sialon powder proceeds in two steps. The first is the oxidation of the amorphous phase at the particle surface. The second is the oxidation of the crystalline phase at bulk. Thus a very rapid oxidation is seen in the beginning while a very slow oxidation follows after a short period.

6-5. SUMMARY

The experimental results observed in the present investigation indicate that typically all α' -sialon and mixed $\alpha'+\beta'$ -sialon ceramic microstructures contain a small amount of a residual glassy phase after sintering, comparable with β' -sialon ceramics. During sintering there is a viscous liquid phase, after cooling a glassy phase remains between the grain boundaries. As a result there is a slight shift of the composition of the crystalline phases. Also in case the amount of yttria used is below the solubility limit, a part of the yttria remains as an amorphous phase at the grain boundaries.

The amount of the grain boundary phase was seen to increase with increasing amount of $Y_2O_3:9AlN$ in the starting mixtures. Also the addition of La_2O_3 to the starting mixture resulted in a change of the composition and an increase of the grain boundary glassy phase. On the contrary, the addition of alumina to the starting mixtures showed a small influence on the amount of the grain boundary phase. For monolithic α' -sialon ceramics the increasing amount of alumina in the starting mixtures was seen to have a very minor influence on the grain size and microstructure morphology. In contrast, addition of alumina reduced the ratio of the length to width of the β' -sialon grains.

The composite $\alpha'+\beta'$ -sialons have the highest fracture toughness of $6.0 \text{ MPa}\cdot\text{m}^{1/2}$ and biaxial bending strength of 734 MPa in the case of sample A4, whereas the highest Vickers hardness achieved is 21 GPa in the case of monolithic α' -sialon ceramics. The mechanical properties achieved in the present investigation are rather good in comparison with the data reported in literature.

In general, for both monolithic α' - and composite $\alpha'+\beta'$ -sialons an increasing amount of alumina in the starting mixtures results in a lower strength and fracture toughness. The influence on the mechanical properties of the addition of La_2O_3 to the starting mixture was not studied.

Active oxidation was observed to occur after a short period of passive oxidation. It is supposed to be due to the oxygen diffusion control through an oxidized layer. The oxidation resistance of α' -sialon ceramics shows very complicated relationships with the temperature and the partial pressures. The composition and amount of the amorphous phase at grain boundaries play a very important role. Oxidation is reduced with decreasing amount of grain boundary

amorphous phase.

Final summary and conclusions will be presented in the next chapter.

6-6. REFERENCES

1. Gillot, N., Cowlam, N. and Bacon, G.E., *J. Mater. Sci.*, 1981,16,2263.
2. van Dijen, F.K., Metselaar, R. and Helmholtz, R.B.,
J. Mater. Sci. Lett., 1987,6,1101.
3. Rietveld, H.M., *J. Appl. Crystallogr.*, 1969,2,65.
4. Albinati, A. and Willis, B.T.M., *J. Appl. Crystallogr.*, 1982,15,361.
5. Izumi, F., Mitomo, M. and Bando, Y., *J. Mater. Sci.*, 1984,19,3115.
6. Izumi, F., Mitomo, M. and Suzuki, J., *J. Mater. Sci. Lett.*, 1982,1,533.
7. Young, R.A. and Wiles, D.B., *J. Appl. Crystallogr.*, 1982,15,430.
8. Jack, K.H., *J. Mater. Sci.*, 1979,14,1135.
9. Jack, K.H., Progress in Nitrogen Ceramics, ed. Riley, F.L., 1983, p45,
Martinus Nijhoff, The Hague.
10. Cao, G.Z. and Metselaar, R., to be published in *Chemistry of Materials*.
11. Sakurai, T. and Kobayashi, K., *Rikagaku Kenkyusho Hokoku*, 1979,55,69.
12. Huang, Z.K., Greil, P. and Petzow, G., *J. Am. Ceram. Soc.*, 1983,66,C-96.
13. Stutz, D., Greil, P. and Petzow, G., *J. Mater. Sci. Lett.*, 1986,5,335.
14. Slasor, S. and Thompson, D.P., *J. Mater. Sci. Lett.*, 1987,6,315.
15. Slasor, S. and Thompson, D.P., Non-oxide Technical and Engineering Ceramics, ed. Hampshire, S., 1986, p223, Elsevier Applied Sciences.
16. Ukyo, Y. and Wada, S., Euro-Ceramics, eds. de With, G., Metselaar, R. and Terpstra, R.A., 1990, p1.566, Elsevier Applied Science.
17. McGuire, G.E. (ed.), Semiconductor Materials and Process Technology Handbook, 1988, Noyes Publications.
18. Kingery, W.D., Brown, H.K. and Uhlman, D.R., Introduction to Ceramics, 1976, John Wiley and Sons.
19. German, R.G., Liquid Phase Sintering, 1985, Plenum Press, New York.
20. Greil, P., Nagel, A., Stutz, D. and Petzow, G., Presented at German-Yugoslavian Symposium on Advanced Materials, April 22-24th, 1985, FRG.

21. Stutz, D., Ph.D Thesis, Institute für Metallkunde der Universität Stuttgart, D-7000 Stuttgart, FRG.
22. Cao, G.Z., Metselaar, R. and Ziegler, G., To be published in Proc. 7th Cimtec, June 1990, Italy.
23. Ekström, T., Austceram 90, eds. Darragh, P.J. and Stead, R.J., 1990, p586, Trans. Techn. Publications Ltd. Australia.
24. Ekström, T., presented in Nov. 1990, Arita, Japan.
25. Ekström, T., Mater. Sci. Eng., 1989,A109,341.
26. Ekström, T., Mater. Sci. Forum, 1988,34/36,605.
27. de With, G. and Wagemans, H.H.M., J. Am. Ceram. Soc., 1989,72,1538.
28. Kokmeijer, E., Ph.D Thesis, Eindhoven University of Technology, 1990.
29. Slasor, S. and Thompson, D.P., Non-oxide Technical and Engineering Ceramics, ed. Hampshire, S., 1986, p223, Elsevier Applied Science.
30. Ishizawa, K., Ayuzawa, N., Shiranita, A., Takai, M., Uchida, N. and Mitomo, M., Ceramic Materials and Components for Engines, eds. Bunk, W. and Hausner, H., 1986, p511, DKG.
31. Mitomo, M., Tanaka, H., Muramatsu, K., Ji, N. and Fuji, Y., J. Mater. Sci. Lett., 1980,15,2661.
32. Chatfield, C., Ekström, T. and Mikus, M., J. Mater. Sci., 1986,21,2297.
33. Wötting, G. and Ziegler, G., Sprechsaal, 1986,119,265.
34. Uchida, I., Takai, M. and Matsushita, Y., Shinagawa Technical Report, 1990,33,209.
35. Ukyo, Y. and Wada, S., Nippon Seram. Kyokai Gakuj. Romb., 1989,97,872.
36. Ekström, T., Solid State Phenomena, 1989,8/9,471.
37. Olsson, P.O. and Ekström, T., J. Mater. Sci., 1990,25,1824.
38. Ekström, T., Kall, P.O., Nygren, M. and Olsson, P.O., Mater. Sci. Eng., 1988,A105/106,161.
39. Arató, P., Besenyi, E., Kele, A. and Weber, F., to be published in Proc. 7th Cimtec, June 1990, Italy.
40. Singhal, S.C., Ceram. Int., 1976,2,123.
41. Singhal, S.C., Nitrogen Ceramics, ed. Riley, F.L., 1977, p607, NATO ASI Series E23, Noordhoff, Leyden.
42. Singhal, S.C., J. Mater. Sci., 1976,11,500.

43. Wanger, C., J. Appl. Phys., 1958,29,1295.
44. Antill, J.E. and Warburton, J.B., Corr. Sci., 1971,11,337.
45. Cubicciotti, D., Lau, K.H. and Jones, R.L.,
J. Electrochem. Soc., 1977,124,1955.
46. Fanz, I. and Langheinrich, W., Solid State Electron., 1971,14,499.
47. Porz, F. and Thummler, F., J. Mater. Sci., 1984,19,1283.
48. Babini, C.N., Bellosi, A. and Vincenzini, P., J. Mater. Sci., 1984,19,1029.
49. Pomeroy, M.J. and Hampshire, S., Mater. Chem. and Phys., 1985,13,437.
50. Van Dijen, F.K. and Metselaar, R., Science of Ceramics 14, ed. Taylor, D.,
1988, p327, The Institute of Ceramics, Stoke-on-Trent.
51. Sato, T., Haryu, K., Endo, T. and Shimada, M., J. Mater. Sci., 1987,22,2635.
52. Dortmans, L.J.M.G. and de With, G., to be published in J. Eur. Ceram. Soc.

CHAPTER SEVEN. SUMMARY AND CONCLUSIONS

The formation, densification, microstructure, and properties of both yttrium-containing α' -sialons and mixed $\alpha'+\beta'$ -sialons have been described in the previous chapters and are summarized as follows.

The compositions of the materials studied were restricted to the concentration plane of $\text{Si}_{12}\text{N}_{16}\text{-Y}_4\text{Al}_8\text{N}_{12}\text{-Si}_4\text{Al}_8\text{O}_8\text{N}_8$ in the Y-Si-Al-O-N system. The materials can be divided into two groups according to the composition of the starting mixtures. The materials of one group are prepared from Si_3N_4 , AlN, and Y_2O_3 and the others contain, apart from Si_3N_4 , AlN and Y_2O_3 , also Al_2O_3 (see Table 3-4). One exception is sample L2, in which 5 wt% La_2O_3 as an extra sintering additive was added to the starting mixture. The final products are either α' -sialons or mixed $\alpha'+\beta'$ -sialons (see Fig. 3-3 and Table 6-3).

In general, Starck LC-12 silicon nitride and Starck Grade C aluminium nitride powders were used. They contain a small amount of metallic impurities and are very fine powders but have a relatively high oxygen content (more than 1.5 wt% oxygen, see Table 3-1). Additionally two other silicon nitride powders (laboratory grade) with both lower oxygen impurity and α' -phase content (see table 3-3) were used in sample B2 and C2, respectively (see Table 3-4). It also should be noted that the oxygen content increases slightly during powder processing (see Fig. 3-4).

The reaction sequences of the formation of α' - and β' -sialons were followed by using X-ray diffraction and in-situ-dilatometry. The formation of α' -sialons starts approximately at 1360 °C, immediately following the dissolution of silicon nitride, while the β' -phase appears at about 1460 °C (see Figs. 4-1 to 4-10), in spite of the variation of composition and amount of liquid phase formed during heating. The completion of the formation of sialons is considered to be at a temperatures below 1800 °C, although a small amount of liquid phase still remains, which should be fully incorporated into the crystal lattice if the reaction proceeds completely. The formation of α' -sialons is proposed to be a reaction controlled process which requires the presence of a liquid phase, but proceeds

independently of the quantity and composition of this liquid phase. Furthermore it is supposed to be a secondary reconstructive phase transformation. The α' - β' phase transformation occurs at high temperatures by chemical reactions in the presence of a suitable liquid phase.

The densification of sialons starts with rearrangement in the temperature range from 1210 °C to 1400 °C, greatly depending on the amount and properties of the liquid phase (see Figs. 4-12, 4-13, 4-15, 4-17, 4-20, and 4-21). The dissolution-precipitation process starts as the dissolution of silicon nitride begins approximately at 1360 °C by the contact-flattening mechanism. At temperatures higher than 1600 °C, the densification of sialons is dominated by the Ostwald ripening process, accompanied by significant grain growth (see Fig. 4-24).

The sintering behaviour varies greatly with the amount and type of sintering additives used in the starting mixtures, the characteristics of the starting silicon nitride powders, the formation and dissolution of some intermediate compounds during firing, and the heating rate used. As the temperature rises up to 1800 °C, with a heating rate of 10 °C/min, for most specimens a relative density of about 90% is reached (see Figs. 4-14 and 4-16). However, full densification of both α' - and mixed $\alpha'+\beta'$ -sialons is very difficult to reach, since the overall composition is nitrogen rich and thus the amount of liquid phase is small. Therefore, gas pressure sintering was applied to overcome this difficulty.

Further densification of sialons by using gas pressure sintering can be achieved only when the closed pore structure is reached (see Figs. 5-2 and 5-3). Thus a two-step sintering process is applied. A modest temperature under a low nitrogen pressure was used at the first step to close the surface pores and then the second step was applied with a combination of high temperatures and high nitrogen pressures to achieve full densification of the sialons. Also a certain amount of oxide additives is necessary to achieve full densification, which was found to be 2.5 mol% yttria in the present work. But a large amount of oxide additives used in starting mixtures results in the formation of a large amount of liquid phase during heating, consequently it leads to swelling during GPS. The process parameters optimized by using a statistical evaluation method are found to be at 1800 °C for 60 min under 0.5 MPa N_2 , followed by 1900 °C for 30 min under 10 MPa N_2 (see Table 5-3). Grain growth in the second step is faster than

that during the first step, probably due to the high atom mobility at higher temperatures and to a shorter diffusion distance because of a small amount of liquid phase left.

The high pressure nitrogen gas not only provides an extra sintering driving force for densification but also reacts with the compacts to alter the composition of the final products. Notably, this reaction results in the α' to β' phase transformation, especially in the surface layer of the mixed $\alpha'+\beta'$ -sialons (see Figs. 5-19 and 5-20).

Microstructure analysis was conducted by means of X-ray and neutron powder diffraction, and optical and electron microscope observations (with energy dispersive spectrometer and the selected area electron diffraction technique). The typical microstructure of both yttrium-containing α' -sialons and mixed $\alpha'+\beta'$ -sialons consists of a crystalline phase of sialons and a small amount of an yttrium-rich amorphous phase at grain boundaries. Only a part of yttrium is incorporated into the crystal lattice and the rest is consumed to form an amorphous phase, even though the overall yttrium content is smaller than the lower solubility limit in α' -sialons. The amount of amorphous phase decreases with the yttria content used in the starting mixtures. The α' -sialon always appears as equiaxed grains (mean grain size $4\ \mu\text{m}$) and the β' -phase as needle or fibre-like grains with an aspect ratio in the range from 4 to 7 (the width of the grains is approximately $2\ \mu\text{m}$). The aspect ratio of the β' -grains decreases with increasing amount of alumina used in the starting mixtures. For mixed $\alpha'+\beta'$ -sialons the elongated β' -grains are dispersed in a matrix of equiaxed α' -grains, and a smaller amount of grain boundary phase (about 3.5 vol%, see Fig. 6-7) than for α' -sialons (about 8 vol%, see Fig. 6-6) was observed. Also it is noted that the addition of La_2O_3 to the starting mixtures results in a reduced α' -grain size (about $1.5\ \mu\text{m}$, see Fig. 6-5), but strongly increased amount of amorphous phase (about 15 vol%, see Fig. 6-8), almost twice as much as in other α' -sialons. This also leads to the formation of many crystal defects (see Fig. 6-9). The amount of the grain boundary amorphous phase increases slightly with the alumina content used in the starting mixtures but its composition remains almost unchanged.

Mechanical properties of α' -sialons are as follows: $Hv_{0.5}$ in a range from 19 to 21 GPa, K_{IC} from 5.3 to 5.7 $\text{MPa}\cdot\text{m}^{1/2}$, and $\sigma_{0.01}$ from 517 to 570 MPa (see

Tables 6-4 and 6-5). Whereas those for mixed α' + β' -sialons are Hv0.5 from 14.5 to 19 GPa, K_{IC} from 5.6 to 6.0 MPa $m^{1/2}$, and σ_{bi} from 600 to 734 MPa. For mixed α' + β' -sialons also a better wear resistance was observed (see Figs. 6-11 and 6-12). The higher fracture toughness and biaxial bending strength achieved for the mixed α' + β' -sialons in comparison with both monolithic α' - and β' -sialon ceramics is explained in terms of the microstructure. The pull-out of elongated β' -grains results in increased fracture energy and the small amount of amorphous phase reduces the size of the flaws. In general, the mechanical properties of both α' - and mixed α' + β' -sialons become worse with increasing amount of alumina content in the starting mixtures.

The oxidation resistance of α' - and mixed α' + β' -sialon ceramics follows a parabolic relationship in the early stage and is explained by a passive oxidation mechanism. However, further oxidation is always overlapped by a weight decrease (see Figs. 6-13, 6-15, 6-16, 6-20, and 6-21). This is probably due to the formation of volatile silicon monoxide (SiO) after the formation of a protective oxide layer, which normally consists of an amorphous silicate phase and a small amount of crystalline phases, such as SiO₂, Y₂O₃·Si₃N₄, and Y₂SiAlO₅N (see Table 6-6 and Fig. 6-17B). The oxidation resistance is seen to deteriorate with an increasing amount of amorphous phase remaining at grain boundaries.

The main conclusions from the experimental results described in this thesis can be summarized as follows:

1. The parallel investigation of formation, densification, and microstructure development has led to a better understanding of the liquid phase sintering process. The formation reaction has a strong influence on the densification via the liquid phase. The composition, amount and properties of the liquid phase are determined by the powder characteristics and by the type and amount of the sintering additives. The liquid phase exhibits a great influence on the densification and grain growth, but only a small influence on the formation of the sialons.
2. Gas pressure sintering is a suitable technique to obtain fully dense, fine grained α' - and mixed α' + β' -sialon ceramics. The use of a statistical evaluation method is of great value to optimise process parameters.

3. An increasing amount of oxide additives favours the fast densification, but has a negative influence on the microstructure and consequently also on the material properties. For full densification of α' - and mixed $\alpha'+\beta'$ -sialon ceramics by using GPS, not less than 2.5 mol% oxide additives are required.
4. The resulting microstructures lead to excellent mechanical properties. The mixed $\alpha'+\beta'$ -sialons show both higher fracture toughness and bending strength than the monolithic sialons. This is due to their favourable microstructure with needle-like β' -grains in a matrix of α' -sialons with fine equiaxed grains and with a small amount of amorphous phase remaining at grain boundaries.
5. Single phase α' -sialon with equiaxed fine grains can be produced. These materials promise the possibility of using superplastic deformation for near-net shaping.
6. The oxidation resistance is strongly influenced by the amount of amorphous grain boundary phase. The highest resistance was obtained for mixed $\alpha'+\beta'$ -sialons, which is due to the small amount of amorphous phase in these materials.

SUMMARY

α' -sialons have attracted more and more attention world-wide recently due to their excellent high temperature mechanical properties and thermal shock resistance. A significant difference between α' -sialons and other nitrogen ceramics, including β' - and O'-sialons, is that the former can incorporate both sintering additives and impurities present into the crystal lattice, because α' -sialons have the α -silicon nitride type structure with interstitials available for cations like Li, Ca, Y.

The work is first concentrated on the study of the formation and densification mechanisms of α' -sialon and $\alpha'+\beta'$ -sialons by means of X-ray diffraction and in-situ-dilatometry. It is shown that the formation of α' -sialons, $Y_x(\text{Si,Al})_{12}(\text{O,N})_{16}$, from $\alpha\text{-Si}_3\text{N}_4$, AlN and oxide(s) is a reaction controlled process which requires the presence of a liquid phase but proceeds independent of the quantity and the composition of this liquid phase. Furthermore, the formation of α' -sialons is considered to be associated with a secondary reconstructive phase transformation as in the case of β' -phase. Although α' -sialon is a stable phase, the $\alpha'\leftrightarrow\beta'$ transformation can occur by chemical reactions.

The densification of α' - and $\alpha'+\beta'$ -sialon ceramics proceeds by the mechanism of liquid phase sintering. Primary rearrangement occurs only in the case of a large amount and a low viscosity of the liquid phase. The dissolution-precipitation proceeds by the contact-flattening mechanism only in the early stage, while the Ostwald ripening mechanism becomes dominant for the further densification at temperatures above 1600°C. The latter is always accompanied by a significant grain growth. Moreover, the characteristics of the silicon nitride starting powders strongly influence the sintering behaviour and the properties of the final product. A high α -phase content and a certain amount of oxygen impurity are considered to be necessary for full densification of α' -sialon ceramics.

Gas pressure sintering (GPS) is employed to achieve full densification of α' -sialon ceramics with a fine-grained microstructure. It is seen that application of a high nitrogen pressure promotes the final densification only when a closed pore structure has been achieved. A statistical evaluation method, known as

response surface methodology, is applied to optimize the process parameters. The optimized GPS process with two steps consists of a heat treatment at 1800°C for 60 min under 0.5 MPa N₂, followed by 1900°C for 30 min under 10 MPa N₂. The high pressure nitrogen gas is found not only to provide an extra sintering driving force but also to react with compacts during sintering.

The typical microstructure of α' - and $\alpha'+\beta'$ -sialon ceramics always consists of a crystalline phase of sialons and a small amount of amorphous phase remaining at grain boundaries. Only part of the yttrium is incorporated into the lattice, while the rest is consumed to form an yttrium-rich glass phase. It is seen that $\alpha'+\beta'$ -sialon composites possess a very promising microstructure, needle-like grains of the β' -phase (the ratio of length to width is about 7) present in a matrix of equi-axed α' -sialon grains (mean grain size is about 4 μm) with a very small amount of amorphous phase remaining at grain boundaries.

In general, α' -sialon ceramics have a higher Vickers hardness (HV0.5) than composite $\alpha'+\beta'$ -sialons, with the highest value of 21.0 ± 1.6 GPa. On the other hand, composite $\alpha'+\beta'$ -sialon ceramics have both fracture toughness (K_{IC}) and biaxial bending strength (σ_{bi}) higher than α' -sialon ceramics, with the highest values 6.0 ± 0.7 MPa·m^{1/2} and 734 ± 55 MPa, respectively.

The oxidation resistance of α' - and $\alpha'+\beta'$ -sialon ceramics follows a parabolic relationship only in the early stage, and overlaps with a weight decrease, which is probably due to an active oxidation after formation of a protective oxide layer. The oxidation resistance is seen to deteriorate with an increase of the amount of grain boundary glassy phase and also with increasing temperature. Besides, partial oxygen pressure exhibits a very complicated influence on oxidation resistance, for which no explanation is available yet.

The results observed in the present experiments indicate that the increasing amount of oxide additives leads to some negative effects on the microstructure and consequently on the properties of the final products. The composite $\alpha'+\beta'$ -sialons have very promising mechanical properties and an oxidation resistance comparable with both monolithic α' - and β' -sialon ceramics. ■

SAMENVATTING

α' -Sialons staan momenteel in de belangstelling vanwege hun uitstekende hoge temperatuur mechanische eigenschappen en goede thermoschok bestendigheid. Een belangrijk verschil tussen α' -sialons en andere stikstofhoudende keramische materialen, waaronder β' - en O' -sialons, is namelijk dat sinterhulpmiddelen en verontreinigingen in het kristallijne rooster van de eerste kunnen worden ingebouwd omdat de α' -sialons dezelfde structuur hebben als α - Si_3N_4 met ruimte voor interstitiële kationen zoals Li, Ca of Y.

Het onderzoek omvat een studie naar de vormings- en verdichtingsmechanismen van α' - and $\alpha'+\beta'$ -sialons met behulp van röntgendiffractie en dilatometrie. Er is aangetoond dat de vorming van α' -sialons, $Y_x(Si,Al)_{12}(O,N)_{16}$, uit α - Si_3N_4 , AlN en oxyde(n) een reactie bepaald proces is. De reactie vindt alleen plaats wanneer een vloeibare fase aanwezig is maar is onafhankelijk van de hoeveelheid en samenstelling van deze vloeibare fase. De vorming van α' -sialons wordt als een secundaire reconstructieve fase transformatie beschouwd net als in het geval van β' -fase. Hoewel α' -sialon een stabiele fase is, kan een $\alpha' \rightarrow \beta'$ transformatie optreden tengevolge van chemische reacties.

De verdichting van α' - and $\alpha'+\beta'$ -sialons vindt plaats door vloeibare fase sintering. Verdichting tengevolge van herrangschikking treedt alleen op wanneer een grote hoeveelheid vloeibare fase met lage viscositeit gevormd is. 'Oplossen en precipiteren' treedt alleen in het beginstadium op tengevolge van 'contact-flattening'. Gedurende verdere verdichting boven $1600^\circ C$ is het Ostwald groei mechanisme dominant, hetgeen duidelijk blijkt uit de waargenomen korrelgroei. Bovendien beïnvloeden de eigenschappen van de uitgangspoeders nadrukkelijk zowel het sintergedrag als de eigenschappen van het gesinterde product. Gebleken is dat voor het verkrijgen van volledig dichte α' -sialons een hoog gehalte α -fase en een zekere hoeveelheid oxidische verontreiniging nodig zijn.

Voor het verkrijgen van volledige dichtheid met fijne microstructuur is daarom gebruik gemaakt van een gasdruk-sinterproces. Het gebruiken van hoge stikstofdruk versnelt de laatste verdichting alleen wanneer reeds een dichte poriënstructuur is verkregen. Een statistische evaluatie methode bekend als

'response surface methodology' wordt toegepast om de optimale procesparameters te vinden. Het geoptimaliseerde gasdruk-sinterproces bestaat uit twee stappen: een sinterstap van 60 minuten bij 0.5 MPa N₂ en 1800°C gevolgd door een sinterstap van 30 minuten bij 10 MPa N₂ en 1900°C. Het hoge druk stikstofgas levert niet alleen een extra drijvende kracht voor het sinteren maar reageert ook met de compacts tijdens het sinteren.

De microstructuur van α' -en $\alpha'+\beta'$ -sialons wordt gekarakteriseerd door de kristallijne fase van sialons en een geringe hoeveelheid amorfe fase die overblijft op de korrelgrenzen. Alleen een deel van het yttrium wordt in het rooster ingebouwd, terwijl de rest wordt verbruikt om een yttriumrijke glasfase te vormen. De composiet $\alpha'+\beta'$ -sialon heeft een zeer veelbelovende structuur bestaande uit naaldvormige β' -sialon korrels (de verhouding tussen lengte en breedte is ongeveer 7) in een equi-axiale α' -sialon matrix (gemiddelde grootte is ongeveer 4 μ m) met een slechts zeer geringe hoeveelheid amorfe fase op de korrelgrenzen.

In het algemeen hebben α' -sialons een hogere Vickers hardheid (HV0.5) dan de composiet $\alpha'+\beta'$ -sialons. De hoogste gemeten hardheid is 21.0 ± 1.6 GPa. Maar de composiet $\alpha'+\beta'$ -sialons hebben zowel een hogere breukweerstand (K_{IC}) als tweeaasige buigsterkte (σ_{b1}) dan α' -sialons met hoogste waarden van 6.0 ± 0.7 MPa m^{1/2} en 734 ± 55 MPa respectievelijk.

De oxydatieweerstand van α' - and $\alpha'+\beta'$ -sialons volgt alleen tijdens de eerste fase een parabolische relatie en overlapt met een gewicht afname vanwege een actieve oxydatie na de vorming van een beschermende oxyde laag. De oxydatieweerstand neemt af met toenemende hoeveelheid interkristallijne fase en met stijgende temperatuur. Daarnaast heeft de partiële zuurstofdruk een ingewikkelde invloed op de oxydatieweerstand waarvoor tot nu toe geen verklaring beschikbaar is.

De waargenomen resultaten van de onderzoeken indiceren dat de composiet $\alpha'+\beta'$ -sialons zeer veelbelovende mechanische eigenschappen hebben en een oxydatieweerstand vergelijkbaar met die van de monolithische α' - en β' -sialons. ■

ACKNOWLEDGEMENTS

I wish to express my great appreciation to all those who have, in one way or the other, devoted much of their time and effort towards the completion of this work.

I am indebted to Prof. dr. R. Metselaar and Prof. dr. G. Ziegler for their constant support and valuable advice received under their supervision.

My grateful acknowledgement is especially due to the ever help of my colleague, Ir. W. Wakelkamp for many things.

Thanks are also due to Prof. G. de With, Dr. Ir. L.R. Wolff, Dr. J. Gerretsen, Dr. F.J.J.van Loo, and Prof. O. van der Biest for their fruitful discussions and critical readings of this thesis and to Ing. J.P.G.M.van Eijk, Ing. G.J. Bezemer, Ing. H. de Jonge Baas, Dr. W.G. Haije, Drs. H.F. Scholten, Dr. Ir. L.J.M.G.Dortmans, and Dr. F.K. van Dijen for their experiment assistance and discussions. Many of my colleagues, in TVM group of TUE and ceramic group of TNO, Eindhoven, and in DLR in Köln, FRG, are also acknowledged.

Finally, my wife deserves special thanks for her patience, encouragement, and love throughout this effort.

Guo-zhong Cao

Eindhoven, the Netherlands

February, 1991

CURRICULUM VITAE

Guo-zhong Cao was born in Nantong county, Jiangsu Province, China on January 30, 1962. There he finished his pre-college education in July 1978. Then he entered the East China University of Chemistry and Technology in Shanghai, from which he was awarded his first degree (B. Sc.) in July 1982. He continued his education as a graduate student at Shanghai Institute of Ceramics, Chinese Academy of Sciences, and worked in the Institute after he received his Master degree in May 1985. In March 1987, he came to the Eindhoven University of Technology in the Netherlands and worked on the project "Preparation and Characterization of α' -Sialon Ceramics".

STATEMENTS (Stellingen)

Guo-zhong Cao

Eindhoven, Feb. 1991

1. Phase diagrams of nitride and oxynitride systems determined by means of experiments do not represent thermodynamical equilibrium phase relationships.

Cao, G. and Metselaar, R., Chemistry of Materials, in press.

This thesis, chapter two.

2. In discussions on the influence of sintering additives on solid state sintering, it is often neglected that impurities in the ppm range can cause a liquid phase.

Bennison, S.J. and Harmer, M.P., J. Am. Ceram. Soc., 66(1983)C-90.

3. Fukuhara stated that the Y-free α' -sialon, $(\text{Si,Al})_3(\text{O,N})_4$, can be made from mixtures of Si_3N_4 and AlN by hot-pressing. This is not true because it is not possible to complete the reaction between Si_3N_4 and AlN at 1723K, which was used for the determination of the phase relationships. What the author actually obtained seems to be unreacted $\alpha\text{-Si}_3\text{N}_4$.

Fukuhara, M., J. Am. Ceram. Soc., 71(1988)C-359.

4. The conclusion of Moser and his colleagues "The increase of positive values of enthalpy of mixing with temperature is an anomaly" is not correct. The increase of positive values of enthalpy of mixing with temperature is a natural consequence of the increasing randomisation of bonds between equal and unequal atoms.

Moser, Z., Castanet, R., Rzyman, K. and Randzio, S.L., Z. Metallkde, 76(1985)596.

5. The statement of Yoshimatsu and Kawasaki "The t-ZrO₂ phase is stabler in the powders prepared from zircoaluminates than in the powders from mixtures of $\text{Zr}(\text{O}^n\text{Bu})_4$ and $\text{Al}(\text{OPr}^i)_3$ because of the more homogeneous and intragranular distribution of the t-ZrO₂ grains" is not convincing. The grain size is an important factor to affect the stability of the t-ZrO₂ phase; this phase is stable when the grains are 0.6 μm in size or smaller.

Yoshimatsu, H. and Kawasaki, H., J. Mater. Sci., 23(1988)332.

6. The claim made by Xu et al regarding the nature of the silicon nitride whiskers they produced is unfounded. Energy dispersive spectroscopy and electron probe microanalysis cannot be used to distinguish between the α and β modifications of silicon nitride.

Xu, Y.R., Huang, L.P., Fu, X.R. and Yan, D.S., Scientia Sinica, A28(1985)556.

7. A relatively high electrical conductivity of the Li- α '-sialons made by hot-pressing is probably due to conduction via a grain boundary amorphous phase.

Mitomo, M. and Uemura, Y., J. Mater. Sci. Lett., 16(1981)552.

8. It is interesting to see that elaborate studies are conducted on heat transfer and combustion in porous radiant burners without consideration of materials aspects and without validation of models.

Sathe, S.B., Peck, R.E. and Tong, T.W., Int. J. Heat Mass Transfer, 33(1990)1331.

9. Although many people take the cold fusion carried out in a test tube as a hype¹, some recent results reveal that there is something new and real². Maybe it is worthwhile to pursue the idea.

1: Close, F., New Scientist, 1752(1991)46.

2: Bockris, J., New Scientist, 1752(1991)50.

10. The development of nuclear energy is of great importance to meet the need of the society in the future¹. However, significant improvement in the efficiency of energy use is the real hope².

1: Besmann, T.M., Am. Ceram. Soc. Bull., 69(1990)1637.

2: Gibbons, J.H., Blair, P.D. and Gwin, H.L., Scientific American, 261(3), (1989)86.

11. To stop the degradation of the environment, we need a change in both the attitude of ordinary people and policy makers and the way we live now.

Scientific American, (Special issue), 261(3), (1989).

12. For any scientific research a thorough literature survey will be of benefit to both scientists and their science.

Roy, R., Am. Ceram. Soc. Bull., 68(1989)1553.